1 Research project title

Extensional Tectonics Across the Northern Nova Scotia Margin
from Ocean Bottom Seismometer Data

Research Project Number:

20150414085619191

Research Project Start Date:

May 1, 2015

Final Report:

New Wide-angle Velocity Models Across the Northeast Nova Scotia Margin From Ocean Bottom Seismic Data

by
Helen Lau and Mladen Nedimović
Dept. of Earth Sciences, Dalhousie Univ., May 2017

Period of Time Covered by Final Report:

May 1, 2015 – April 30, 2017 (The Entire Term)

Date of Submission:

May 28, 2017

Mladen Nedimović

Earth Sciences
Dalhousie University
Life Sciences Centre, Rm. 3054
1355 Oxford Street
Halifax, Nova Scotia
Canada, B3H 4R2
Tel: (902) 494-4524
Fax: (902) 494-6889
E-mail: mladen@dal.ca

2 Summary

The recently conducted Play Fairway Analysis (PFA) for the Nova Scotia margin "has developed a model that allows the potential for a more regional Lower Jurassic source rock that extends beyond the Sable sub basin and underlies the whole margin" (*PFA Atlas*, 2011). To test this model, research funding was made available on a competitive basis by the Offshore Research Energy Association (OERA). Our proposed project for a detailed and rigorous analysis of ocean bottom seismometer (OBS) profiles OETR-2009 and OCTOPUS-2010 (Fig. 1) was funded in 2015 under OERA's Seismic Reprocessing and Analysis research direction. Until this project was funded, OETR profile has only been studied in a preliminary fashion and OCTOPUS profile has not been analyzed at all. These two profiles have the potential to provide important detailed information regarding the location and geometry of deep source rock basins, crystalline basement and Moho, all of which are critical for understanding the early history of the northern Nova Scotia margin. To support detailed analysis of both OBS profiles, we obtained coincident ION GXT long-streamer multichannel seismic (MCS) data and the corresponding images.

In this final report, we first briefly review the contract objectives. This is followed by a summary of the work carried out during the first 15 months of the project during which we produced a detailed layered-velocity model (for details please see 29.04.2016. report) and performed a full-scale error analysis (for details please see 31.07.2016. report) of the OETR-2009 profile. Full interpretation of the obtained results is currently being developed (please see the attached draft manuscript in Appendix 12.2). Through international funds obtained on a competitive basis, we were able to carry out work in addition to what was laid out in the contract and produce a smooth first arrival tomographic model (please see the attached expanded abstract in Appendix 12.1). Our results indicate that the previous interpretation of a shallow crystalline crust beneath the shelf is incorrect as a deep sedimentary basin underneath a high velocity (4.8–5.8 km/s) carbonate layer is modelled. At the outer shelf, the modeled steep, half-graben type, 12 km basement drop matches well with the steep rise of the Moho. Crustal velocities (5.3–7.2 km/s) consistent with continental crust are modelled beyond the slope until the seaward limit of salt structures. Two high gradient lower crust or mantle layers (6.3–8.0 km/s) are modelled for the continent-ocean-transition (COT) seaward. We interpreted these layers as serpentinized mantle. The velocity and nature of the crust above is, however, unresolved. High oceanic crustal velocities (5.0–7.3 km/s) are observed seaward.

During the last 9 months of the contract, we produced a layered-velocity model with full-scale error analysis for the 240-km long OCTOPUS profile, which is perpendicular to the OETR and SMART-1 profiles and coincident with the MCS profile GXT-5100. Because this work was finalized after the last interim report, we detail it in this report. Our results suggest a COT whose character changes along strike. The final velocity model shows 6 sedimentary, 2 crustal and 1 uppermost mantle layers. Velocities within the sedimentary appear uniform along the whole profile. In contrast, two different crustal zones can be observed for the deeper layers. The crustal layer along the eastward 60-km of the profile displays oceanic Layer-2 and -3 velocity characters and is 3–7 km thick. The velocity structure for the rest of the profile to the west appears to show a varying transitional character with very thin crust (0–4 km). Within this zone, 3 different transitional velocity characters can be identified: Trans-1 has velocities that smoothly increase from the crystalline basement at the top (5.5 km/s) to a low velocity (7.4–8.0 km/s) mantle layer at the bottom; Trans-2 is similar to Trans-1 but with an upper crustal layer with velocity of ≈

5.1–5.3 km/s; Trans-3 upper crustal (velocity ≈ 5.0–5.5 km/s) and lower crustal (velocity ≈ 6.1–6.8 km/s) layers overly a low velocity mantle layer. The base of the crust (Moho) also coincides with a high amplitude reflector observed on GXT-5100 reflection profile. We speculate that mafic crust of continental origin may be highly thinned or that a limited amount of mafic melt was emplaced within the transition zone during the breakup. The Trans-1 structure may represent the extreme case where crust broke up without melt and mantle was exhumed to the seafloor. Our velocity model agrees with that of SMART-1 and OETR-2009 where they intersect. We conclude this report by providing insights on margin evolution and suggesting future work.

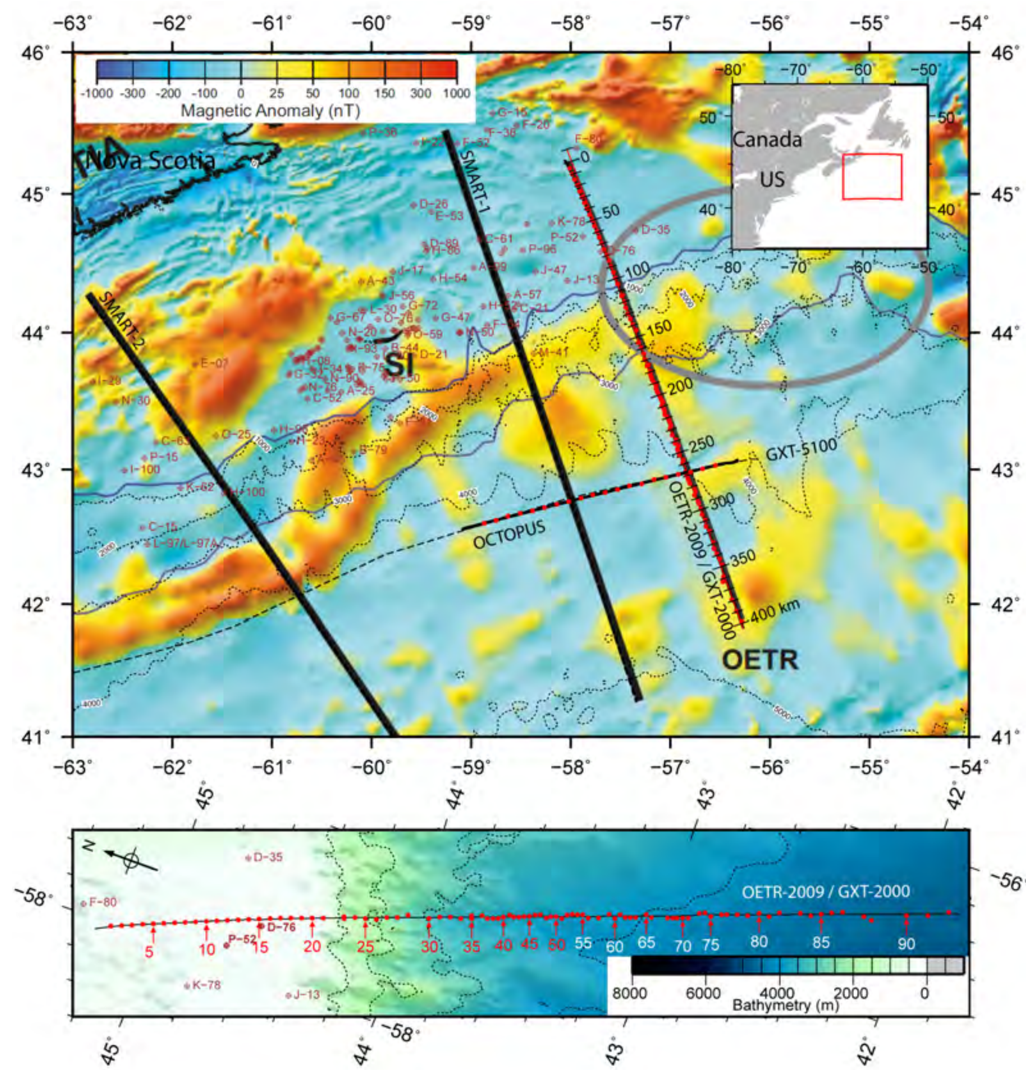

Figure 1. (top) Magnetic anomaly map (colour scale) with locations of OETR-2009 OBS (long red dotted line) and coincident GXT-2000 MCS (black line) profiles, earlier SMART OBS profiles (thick solid black line; Funck *et al.* 2004; Wu *et al.* 2006), connecting OCTOPUS OBS (short red dotted line) and coincident GXT-5100 MCS (black line) profiles, and selected boreholes (brown diamonds). Study area (red rectangle) is shown relative to eastern Canada and US in the inset. Bathymetry is contoured (thin dashed lines) every 1000 m. The OETR-2009 model distance is tick-marked and labelled in black. Red filled circles are OBS locations. SI – Sable Island. (bottom) Area around profile OETR-2009 is enlarged in the lower panel with OBSs numbered in red (white on dark background) and bathymetry in colour scale and contoured every 500 m.

3 Table of contents

4 Introduction

4.1 Background

The continental margin offshore Nova Scotia has long been known as the definitive Atlantic style passive margin; a rifted margin followed by thermal sag and a prograding shelf with a carbonate bank, major river delta and a mobile salt substrate (*Kidston et al.,* 2002). Analogue Atlantic margins are found in the Gulf of Mexico, offshore Brazil and offshore West Central Africa, all with significant proven petroleum reserves. The assessments of the Nova Scotia offshore petroleum potential have evolved through time, together with the petroleum exploration that started some half a century ago and has been, early on, characterized by moderate success (e.g., *EMR-Canada,* 1977; *Proctor et al.,* 1984; *Wade et al.,* 1989; *MacLean and Wade,* 1992; *SOEP,* 1997, *CNSOPB,* 1997; *CGPC,* 1997 and 2001; *Kidston et al.,* 2002 and 2007). Despite the early success, recent exploration has not been fruitful resulting in steady decline in exploration licenses in the first decade of the 21st century. In 2009, recognizing that there is a vast amount of knowledge about the offshore geology in Halifax in need of integration and to rekindle exploration interest in the offshore, the Government of Nova Scotia invested 15 million dollars in the creation of an industry standard Play Fairway Analysis (PFA) project. The PFA project has identified rich hydrocarbon potential of unrisked 120 TCF of gas and 8 bnbbls of oil in place, three times the previous provincial estimate (*PFA Atlas,* 2011). The results of the PFA project have, in part, attracted significant new interest in the offshore Nova Scotia with Shell and BP each investing about one billion dollars in exploration. However, the estimated unrisked petroleum potential has yet to be proven by discoveries and additional investments in offshore research investigations are needed to further reduce geologic risk and to keep the exploration momentum going. Accordingly, government of Nova Scotia has recently embarked on the 2nd phase of PFA with a $12M investment.

We were funded through the 2nd phase of PFA as part of the OERA's Reprocessing and Analysis research priority area to carry out analysis of ocean bottom seismometer (OBS) profiles OETR-2009 and OCTOPUS-2010 (Fig. 1) with the goal to form detailed and rigorous layered velocity models. The obtained result provide information about the targeted area offshore NE Nova Scotia with respect to the location and geometry of deep source rock basins, crystalline basement, Moho, and uppermost mantle. This information is critical for understanding the early rifting history of the northern Nova Scotia margin.

4.2 Regional tectonic framework: remaining questions

When continents rift apart and new ocean basins form, a transition region is created between the old, thick continental crust and young, thin oceanic crust [*Louden and Lau,* 2001]. Based on the amount of volcanism that occurs during rifting, two primary classes of this transitional region at continental margins can develop, volcanic and non-volcanic [*Louden and Lau,* 2001; *Keen and Potter,* 1995]. Standard crustal scale MCS reflection and OBS refraction projects were carried out during the past couple of decades to better understand the ocean-continent transition found offshore eastern Canada (Fig. 2) [e.g., Funck et al., 2004; *Wu et al.,* 2006; *Louden,* 2002, *Van Avendonk et al.*, 2006; *Gerlings et al.,* 2012]. The formed reflection images and velocity models [Louden and Chain, 1999; Louden and Lau, 2001; *Keen and Potter,* 1995; Funck et al., 2004; *Wu et al.,* 2006; *Louden,* 2002, *Van Avendonk et al.*, 2006; *Gerlings et al.,* 2012] show significant basement structural variations between the profiles that are, together with potential field data, interpreted to indicate a volcanic-type margin offshore southern Nova Scotia, a non-volcanic margin offshore central Nova Scotia, and an extremely amagmatic margin further north. These zones of transitional crystalline crust appear to coincide with northward transitions within overlying sedimentary structures, from salt-free to salt bodies in the south, and from autochthonous salt diapirs to allochthonous salt tongues in the north [*Shimeld,* 2004].

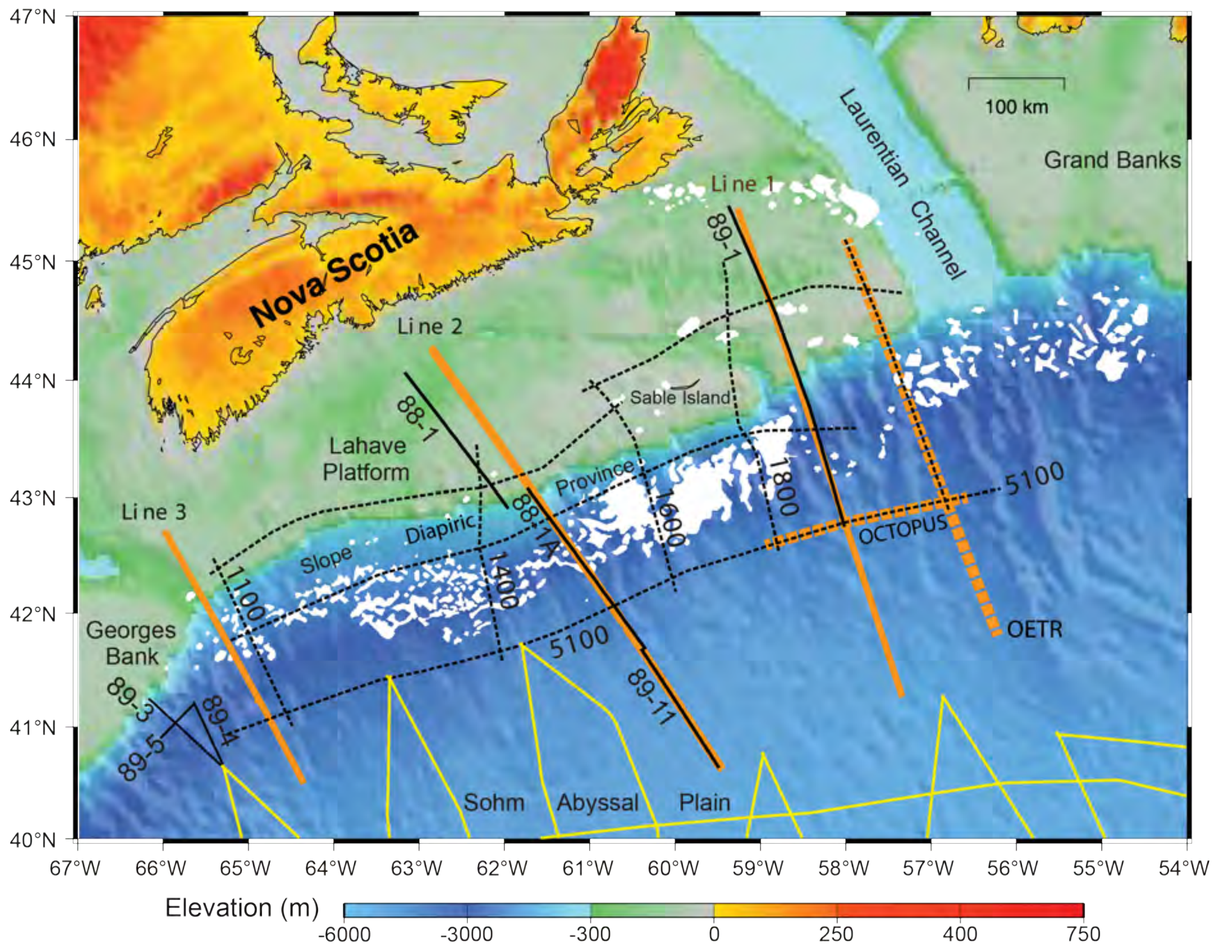

Figure 2. Location of regional seismic profiles offshore Nova Scotia. Regional MCS reflection profiles are shown as solid black lines (Lithoprobe and Frontier Geoscience Program), dashed black lines (ION-GXT NovaSpan Project) and yellow lines (UNCLOS Project). Seismic refraction profiles are marked by orange lines, solid for SMART Lines 1-3 and dashed for OCTOPUS and OETR. Jurassic salt over the Slope Diapiric Province is indicated by white patches.

The existing knowledge about the crystalline basement structure offshore Nova Scotia (Fig. 2) has, so far, been gained using sparsely spaced (100s of km) regional seismic profiles with sparsely spaced (~20 km) OBS instruments. New breakthroughs in our understanding of crustal structures offshore Nova Scotia will require new 2D OBS data with closer profile spacing (10s of km) and/or smaller instrument spacing (1-5 km) (*Lau et al.,* 2015; *Watremez et al.,* 2015). Densely spaced, high-resolution OBS profile data will also require additional, more sophisticated data analysis such as are waveform tomography and prestack depth migration. Both the new data and the advanced data analysis are needed to resolve deep structures with sufficient resolution to answer first order questions such as is: What is the detailed nature of the ocean-continent transition, which can exhibit complex structures, including highly extended continental crust, exposed mantle and thin oceanic crust that are difficult to distinguish with standard data and data analysis methods. Detailed imaging of these structures is critically important for an improved understanding of such widely-held concepts as the continent-ocean boundary and the breakup unconformity.

The style of rifting (volcanic or non-volcanic) also has a direct implication on the rift infill and paleo-water depth at the onset of drifting (*PFA Atlas,* 2011). In magma rich conditions the rift zone is uplifted with continental and shallow marine conditions prevailing, thus allowing for the deposition of confined marine source rock. In magma poor conditions the stretching of the lithosphere induces mantle exhumation and rapid subsidence resulting in 1-2 km deep marine conditions that preclude the deposition of shallow marine source rock. The presence of such a source rock can have a direct impact on the petroleum system. The general consensus among academic researchers is that the transition from magmatic to amagmatic rifting occurs offshore south-central Nova Scotia. This view is consistent with the absence of any direct evidence for a magma rich margin, such as a continuous belt of seaward dipping reflectors (SDR) or a continuous and homogeneous East Coast Magnetic Anomaly (ECMA; Fig. 1). However, reinterpretations by consulting companies for the *PFA Atlas* (2011) have found several features that they believe strongly suggest that the magma rich Camp Province could extend north up to the Newfoundland-Azores transform fault. In this interpretation, the entire Nova Scotia margin could be considered as a magma rich rifted margin. This suggestion indicates that there is an urgent need for detailed data analysis of the existing OBS profiles in order to de-risk the petroleum exploration offshore Nova Scotia. The research program we carried out was designed to directly address some of this need and, because was focused on regional geologic de-risking, it equally benefits all parties interested in petroleum exploration offshore Nova Scotia.

4.3 Proposed research program and delivered materials

Several OBS profiles collected offshore Nova Scotia since 2001 have only been analyzed in a very preliminary fashion (NS-3, OETR, GSC-1; Fig. 1) or have not been analyzed at all (OCTOPUS). The data collected along these profiles is rich in information and represents >80% of all of the OBS data ever collected offshore Nova Scotia. We proposed to analyze profiles OETR and OCTOPUS to produce detailed and rigorous layered velocity models. These two profiles have small OBS spacing (in particular the OETR profile where instruments are separated at places by as little as 1-2 km) and therefore show the highest potential for extracting significant new information. Moreover, the OBS data analysis for these two profiles can further benefit from iterative processing with coincident ION-GXT long-streamer MCS data, which that company kindly provided to us. The plan was to carry out the proposed analysis in three phases over a three-year period, with each phase taking one year. We were funded by OERA for the first two phases/years of the project, with the third year optional and based on the results of the first two years.

During the past two years, we first completed our implementation of navigation and data corrections to the OETR dataset to precondition it for analysis. Helen Lau invested over a year (i.e. $90k from other funding sources) to prepare these data even before this contract started so this component of the project did not take much time and effort to complete. Nevertheless, this work was necessary because, as delivered raw to us by GeoPro, the data were characterized by significant errors that preclude analysis. Once the data were ready, we proceeded with a detailed layered velocity modeling approach with RAYINVR software and then full-scale error analysis and development of a resolution matrix. The same data analysis approach was subsequently applied to the OCTOPUS profile. The 2010 OCTOPUS wide-angle refraction profile data were collected with intermediate OBS spacing of ~10 km. The OCTOPUS profile is important because it crosses the SMART 1 and OETR profiles and allows for a potential estimation of anisotropy in velocity of the lower crust and uppermost mantle. Information about directional changes in the velocity of the lower crust and uppermost mantle is likely to be the critical for deciphering the margin type as magmatic or amagmatic in this area of the Nova Scotia offshore.

Our plan for the next (third) year was to prestack migrate in a joint fashion the OETR-2009 OBS and NovaSpan 2000 MCS data. To the best of our knowledge, this would be the first attempt to carry out this type of data analysis and we anticipate significant improvements in the imaging with this approach, in particular of the crystalline basement, crust and the Moho. In order to construct an accurate and detailed but smooth velocity model needed for joint prestack migration of the OBS and MCS data, our plan was to first run a detailed tomographic inversion of the OETR profile. These advanced data analysis processes can be carried out only because of the closely spaced distribution of the OBS instruments along this profile and will result in deep crustal velocity profiles and reflection images characterized by resolution not previously seen on the Scotia margin. However, a change in focus was requested by OERA for year three.

4.3.1 Year I

Activities:

1. Implementation of navigation and data corrections to the OETR dataset to precondition it for analysis (Year 1; Month 1)
2. Detailed analysis of OETR dataset using a layered velocity modeling approach with RAYINVR software (Year 1; Months 2 to 12)

Outcomes and deliverables:

1. Corrected ocean bottom seismic (OBS) data and navigation files (Delivered at the end of year 1 - month 1)
    a. Common receiver gathers of all channels on all OBSs in SEGY IBM format; Data include corrections applied to remove erroneous time shift found in the earlier version of the dataset and corrections applied to remove navigation errors due to GPS malfunction
    b. Revised OBS locations in latitudes and longitudes (ascii file)
    c. Revised shot navigation tables (ascii files)
2. Layered P-wave velocity model (Delivered at the end of year 1 - month 12)
    a. A detailed layered velocity model from seafloor to mantle, consistent with observations of a complex reflection image on GXT line 2000 (e.g. basement and salt diapirs), produced using RAYINVR software with constraints from:
        i. first and secondary arrivals picked in the OETR-2009 OBS data;
        ii. multi-channel seismic (MCS) reflection section (NovaSpan-2000).
    b. Final velocity model delivered in the following formats:
3. RAYINVR v.in format (ascii file)
4. Gridded three-column format with distance-depth-velocity (ascii file)
5. Gridded IBM SEGY format (binary file)

6. Gridded GMT format (binary file)
7. Plot in PDF format, with GMT script and supporting files used to plot

Associated reports for OERA:

1. OETR data corrections and preparation for analysis (delivered on 31.05.2015.)
2. Preliminary OETR layered P-wave velocity model (delivered 31.10.2015.)
3. First year-end report with final OETR velocity model (delivered 29.04.2016.)

4.3.2 Year 2

Activities:

1. Full-scale error analysis and development of a resolution matrix for OETR line (Year 2; Months 1 to 3)
2. Detailed analysis of OCTOPUS data using a layered velocity modeling approach with RAYINVR software (Year 2; Months 4 to 8)
3. Full-scale error analysis and development of a resolution matrix for OCTOPUS line (Year 2; Months 9 to 12)

Outcomes and deliverables:

1. Full-scale error analysis results and a resolution matrix (Delivered at the end of year 2 - month 3)
    a. Error analysis statistics for each observed wave phase. These include: (i) number of observed picks; (ii) RMS residual between modeled and observed traveltimes (t_{rms}); (iii) normalized (χ^2)
    b. Resolution matrix values for each depth and velocity node
    c. Plot of resolution matrix values in PDF format, with GMT script and supporting files used to plot
2. Detailed layered velocity model for the OCTOPUS 2010 ocean bottom seismometer (OBS) profile (Delivered at the end of year 2 - month 8)
    a. Same deliverables as for OETR-2009 (please see Outcomes and deliverables for Year I)
3. Full-scale error analysis results and a resolution matrix for the OCTOPUS 2010 OBS profile (Delivered at the end of year 2 - month 12)
    a. Same deliverables as for OETR-2009 (please see Outcomes and deliverables for Year I)

Associated reports for OERA:

1. OETR uncertainty and resolution analysis (delivered on 31.07.2016.)
2. Final Octopus layered P-wave velocity model (delivered 31.12.2016.)
3. Final report (delivered 26.05.2017.)
    a. Overall summary of activities and results for the second year of contract
    b. Interpretations of the OETR-2009 and OCTOPUS layered velocity models supported by error analyses and resolution matrices with insights into tectonic history for margin formation
    c. Emphasis on crystalline basement location, crustal thickness and evaluation of potential deep source rock basins

4.3.3 Year 3

Activities:

1. Detailed tomographic inversion of the OETR profile using JIVE3D or TOMO2D software (Year 3; Months 1 to 6)
2. Joint prestack migration of OETR-2009 and NovaSpan 2000 data using Geodepth Software (Year 3; Months 6 to 12)

Outcomes and deliverables:

1. Detailed tomographic velocity model for OETR profile (Delivery at the end of year 3 - month 6)
   a. A detailed minimum structure smooth tomographic velocity model constrained by first arrival picks and basement/Moho reflection picks. Final velocity model will be delivered in the following formats:
      i. Gridded three-column format with distance-depth-velocity (ascii file)
      ii. Gridded IBM SEGY format (binary file)
      iii. Gridded GMT format (binary file)
      iv. Plot in PDF format, with GMT script and supporting files used to plot
2. Joint prestack migrated profile of OETR-2009 and NovaSpan 2000 data (Delivery at the end of year 3 - month 12)
   a. Joint prestack migration of OETR OBS and GXT line 2000 MCS data using the smooth tomographic model with special attention to crustal structures (e.g., crystalline basement and Moho). Prestack migrated profile will be delivered in the following formats:
      i. SEGY IBM (binary file)

Associated reports for OERA:

1. Third year-end report
   a. Summary of activities and results for the third year of contract
   b. Processing details for prestack migration
2. Final report for the whole three year project

4.4 Fulfillment of contract

We have successfully completed all the work proposed for Year I and II. This report including, all deliverables have been sent to OERA as outlined in the contract. We also have given two year-end presentations on our results. Due to a shift to a new focus, a revised contract for the next two years is currently under negotiation. Although Year III of the last contract will no longer apply, using other funding external to Nova Scotia, we managed to finish the proposed TOMO2D tomographic inversion of the OETR profile, which represents half of the work (6 months) that was originally proposed for Year 3 of the contract. We are now working toward producing manuscripts for submission and eventual publication in major international peer-review journals.

5 Discussion of objectives, methodology and results

5.1 Final P-wave layered velocity model of OETR 2009 profile

5.1.1 Introduction

Our main objective for Year 1 of the project was to analyse and produce a layered velocity model using the OETR-2009 wide-angle seismic profile collected across the Nova Scotia margin. Before we were able to do this, we performed, mostly before the contract started, a detailed and careful quality control on the OBS data sent from GeoPro. Although many problems were encountered regarding the timing of the data, we were able to successfully fix the errors and locate the on-seafloor positions of 87 OBSs, 78 of which provided reliable data for analyses. We also performed a full-scale error analysis of the model in Year 2 to test the integrity of both the model and the corrected data. The test results were generally positive and indicated that the quality and the impact of our results is high and, therefore, suitable for publication in a major international peer-review journal. So far, we completed all the figures and half-finished the text for the manuscript. Please see Appendix 12.2 for the manuscript in its current form as it provides a detailed description on the data, method and results.

5.1.2 Data problems and solutions

A processing report was submitted to OERA in May 2015. This document details the pre-conditioning of data in preparation for analysis. Pre-conditioning of data was necessary because errors were detected in our first attempt to model the data, which we received directly from GeoPro.

To remove all the errors and to appropriately pre-condition the data for velocity modelling, we applied the following changes to the data:

i. Re-numbering of OBSs from those used during deployment
ii. Removal of erroneous static time shift
iii. Removal of traces of redundant shots
iv. Recovery of previously unused data for OBS 23 & 25 to extend coverage
v. Corrections for clock jumps
vi. Upload of geometry into headers

To ensure integrity of the header information, we retrieved, organized and reproduced a new set of the following geometry that is free of all known errors:

i. Water depth
ii. Ship navigation
iii. Shot navigation
iv. Trace start time
v. Water velocity
vi. Receiver positions

The resulting OBS data and navigation files were sent to OERA together with the processing report.

5.1.3 Final Velocity Model

Fig. 3a shows the final velocity model with crustal zonal interpretations. This model shows many complex structures that are not present in the earlier GeoPro model presented in the PFA report. In particular, the basement is better defined and a low velocity zone is modelled underneath the shelf beneath a high velocity carbonate bank. This detailed model is more consistent with the amount of data used to constrain the model (Fig. 3b).

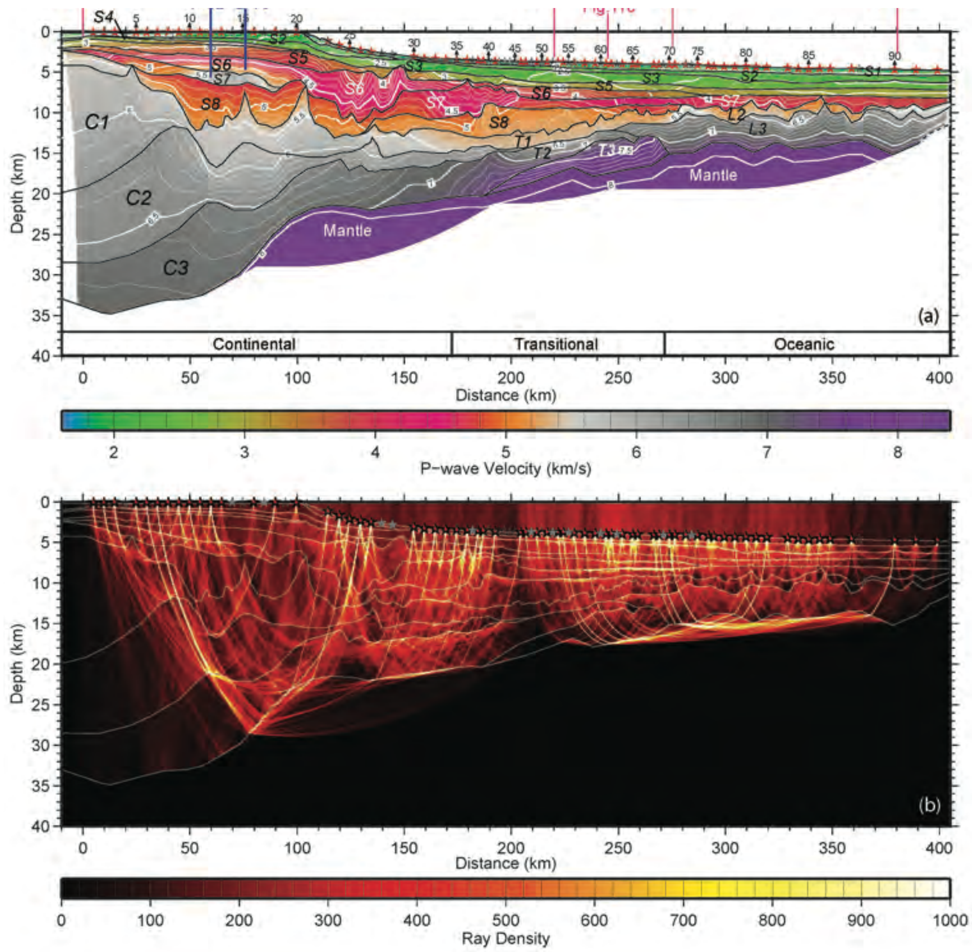

Figure 3. P-wave final velocity model of OETR-2009 profile (1) and the constraining ray diagram (b). Stars are OBS locations with filled colours representing differing constraints input to the model: red, fully picked; grey, not picked; unfilled, no data. (a) Velocity model with layer boundaries in black lines and velocities defined by colour scale. White rectangles at the bottom represent crustal zonal interpretations. Velocities are contoured every 0.1 km s^{-1} (white lines). OBS numbers are above black arrows; vertical blue lines are well positions projected along profile. Area outside of ray coverage is masked. (b) Illumination diagram showing ray counts in colour scale (truncated at 1000 rays). Only rays used for inversion are shown. Grey lines are model boundaries.

5.1.4 Error analysis and resolution test

A common way to evaluate the robustness of resulted velocity model is through error analysis. Table 1 summarizes the error analysis statistics based on misfit between the observed and modeled traveltimes. Our χ^2 of ~2 shows good fit between observations and the model. We also calculated the diagonal value of the resolution matrix for each of our model parameters (Fig. 4). A value of <0.3 represents relatively poor resolution and >0.7 implies the opposite. Our results show that most of the relevant parts of the model range from moderately to well resolved.

Table 1. Error analysis statistics for picked OBSs: number of raytraced picks (n), mean uncertainty of all input picks ($t_{uncertainty}$), RMS residual between modeled and observed traveltimes (t_{rms}) and normalized (χ^2).

	Phase	n	mean $t_{uncertainty}$ (s)	t_{rms} (s)	χ^2
Sediment	P_{S1}	658	±0.018	0.029	2.861
	$P_{S2}P$	3092	±0.021	0.018	0.791
	P_{S2}	2980	±0.017	0.025	2.304
	$P_{S3}P$	4407	±0.024	0.027	1.192
	P_{S3}	5553	±0.029	0.043	1.706
	$P_{S4}P$	9394	±0.032	0.034	1.157
	P_{S4}	822	±0.023	0.020	0.737
	$P_{S5}P$	338	±0.025	0.023	0.789
	P_{S5}	3185	±0.033	0.041	1.708
	$P_{S6}P$	6952	±0.033	0.030	0.799
	P_{S6}	4410	±0.037	0.060	2.714
	$P_{S7}P$	4514	±0.043	0.061	1.879
	P_{S7}	7271	±0.042	0.045	1.131
	$P_{S8}P$/ P_BP	7223	±0.046	0.062	1.566
	P_{S8}	2739	±0.048	0.051	1.166
	$P_{B'}P$	4567	±0.049	0.059	1.404
Crust	P_{C1}	3598	±0.049	0.052	1.080
	$P_{C2}P$	11387	±0.060	0.113	2.967
	P_{C2}	7135	±0.053	0.068	1.700
	$P_{C3}P$/ $P_{m'}P$	9278	±0.061	0.090	2.055
	P_{C3}	5186	±0.069	0.148	4.191
	P_mP	13805	±0.083	0.163	3.805
Mantle	P_{n1}	1726	±0.050	0.051	1.260
	P_{n2}	14937	±0.087	0.174	3.394
All		135157	±0.053	0.099	2.177

Note: The basement reflection is comprised of P_BP (reflection from the bottom of S7 where S8 is absent) and $P_{B'}P$ (reflection from the bottom of S8). P_mP (reflection from the bottom of C3) is the continental Moho whereas $P_{m'}P$ (reflection from the bottom of O2) is the oceanic Moho.

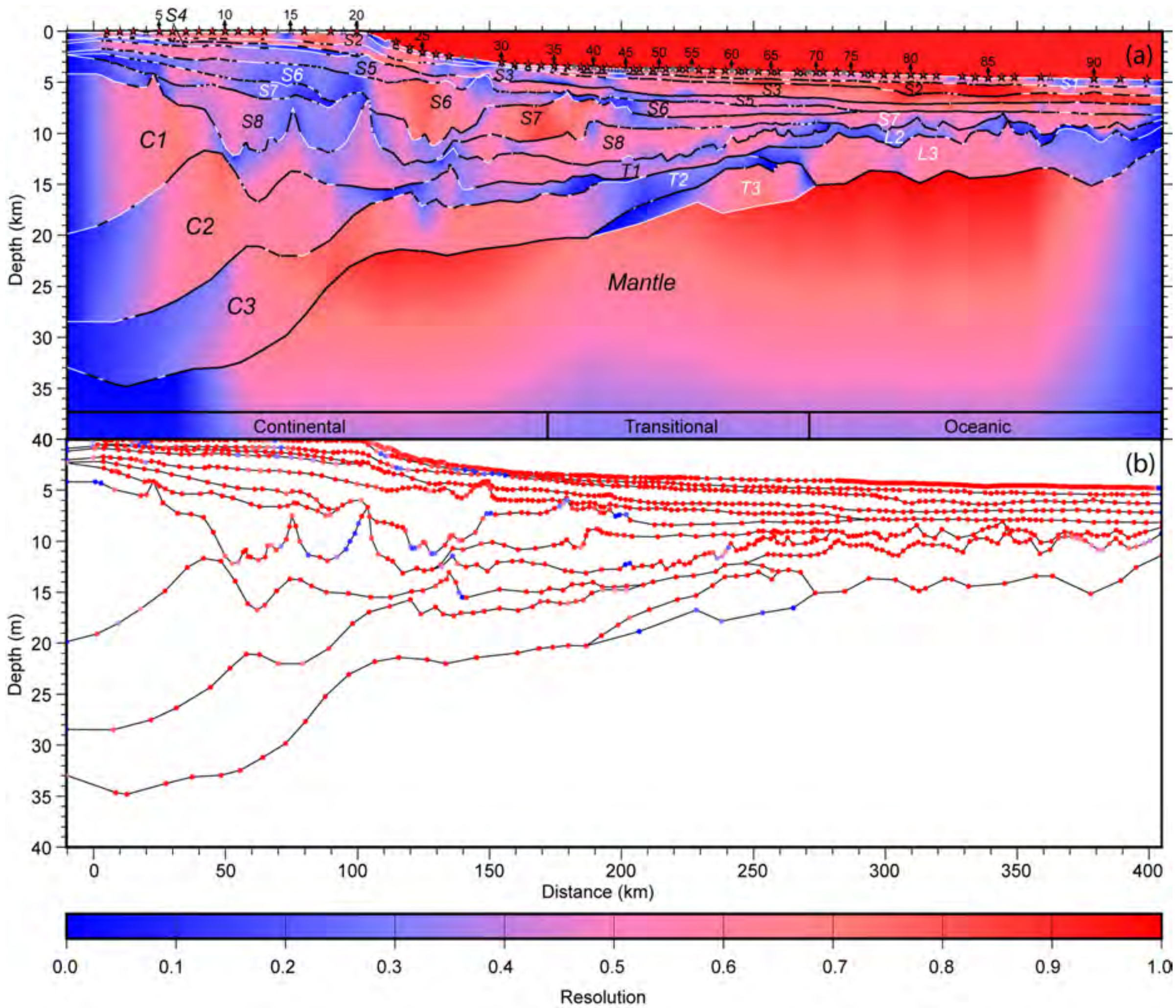

Figure 4. Model resolution plots. (a) Colour scale shows gridded diagonal values of the resolution matrix for all velocity nodes. Note that values for areas between layer boundaries are linearly interpolated from values along the boundaries. Black lines represent locations of layer boundaries illuminated by picked reflections and white lines are locations without observations. See caption of Figure 3a regarding model layer names, crustal zonal interpretations and OBS symbols. (b) Depth resolution of velocity model boundaries. Black lines are velocity model layer boundaries. Colour-scaled circles are diagonal values of the resolution matrix of the depth nodes.

5.2 Final P-wave layered velocity model of OCTOPUS 2010 profile

5.2.1 Introduction

After completion of work on profile OETR-2009, we started analyzing the new data from OCTOPUS profile acquired by Dalhousie University in 2010. The OCTOPUS profile ties with the OETR-2009 and SMART-1 profiles (Fig. 5; Funck *et al.* 2004). The OCTOPUS profile is also coincident with the eastern end of MCS profile GXT-5100 which intersects with SMART-1 within the interpreted COT. This profile is, therefore, important to the study of the nature of the transitional crust and any along-strike variations between the two crustal-scale velocity models available for the NE Nova Scotia margin. Since OCTOPUS profile is orthogonal to the OETR-2009 and SMART-1 profiles, it can be used to investigate seismic anisotropy in any layer of

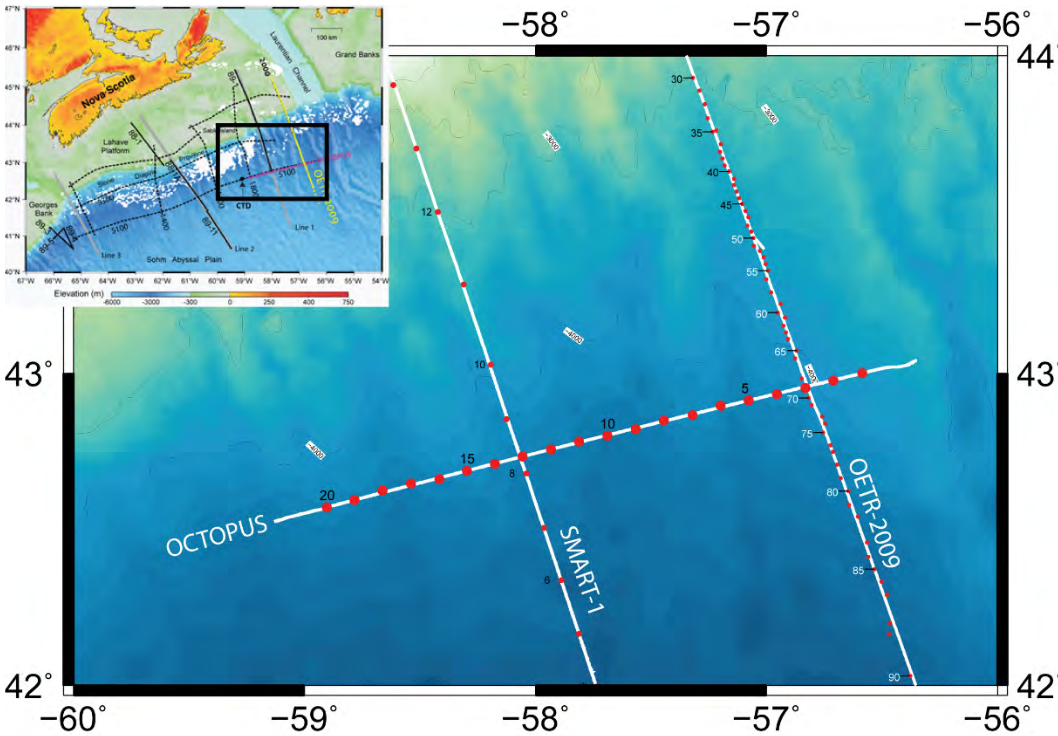

Figure 5. Bathymetry map showing the OCTOPUS, SMART-1 and OETR-2009 profiles. Red circles are OBS positions with OBS numbers in black. Inset shows the location of main map (black rectangle) relative to Nova Scotia other major seismic profiles.

interest by comparing the results from the three profiles. Anisotropy can be a useful tool to discriminate between isotropic gabbro and anisotropic olivine that have both been proposed for the transition.

During the period from August 2016 to December 2016, we have successfully processed, analysed and modelled the OCTOPUS data and a final layered P-wave velocity model has been developed. We followed the same modeling procedures as for the OETR-2009 profile. Fortunately, we did not encounter any major data problems with the OCTOPUS data the way we did with the OETR-2009 data. Error analysis and resolution test followed, from January 2017 to the end of April 2017, which also marks the end of this contract.

5.2.2 Arrival identification

Data from 19 OBSs provided credible observations for interpreting primary and secondary P-wave phases. However, one OBS (#5) recorded data with a time-shift that we do not have sufficient information to correct for so these data were not used. Wave phases are more clearly observed at plots with different ranges in offset and time and different reduction velocity (a.k.a. linear moveout velocity). Using OBS 3 as an example, the shallower and lower velocity phases (1.5–3.5 km/s) are more easily seen at a plot restricted to the near offsets and small traveltime reduced at 3 km/s (Fig. 6); while deeper and higher velocity phases are better observed on plots using a larger offset and traveltime ranges reduced at 6 km/s (Fig. 7). Using these plots, we delineate coherent refracted and reflected arrivals from the OBS data and build a layered-velocity model to calculate traveltime curves to fit the observed wave phases (Figs. 6–10).

Table 2. Glossary of seismic phases

Phase	Description
Direct	Direct wave through the water
P_{sn}	P-wave refracted phase through the nth sedimentary layer from the top
$P_{sn}P$	P-wave reflected phase from the bottom of the nth sedimentary layer from the top
P_BP	P-wave reflected phase from the basement top
P_{C1}/P_{C2}	P-wave refracted phase through the upper/lower crystalline crust or exhumed mantle layers
$P_{C2}P$	P-wave reflected phase from the top of the lower crystalline crust
P_mP	P-wave Moho reflection or reflection at the crust-mantle boundary
P_{n1}	P-wave refracted phase through interpreted, serpentinized mantle
P_{n2}	P-wave refracted phase through normal mantle

5.2.3 Layered velocity model constraints

The seafloor depth, which is the bottom of the first layer, is calculated from the seafloor reflection in two-way-travel-time (TWTT) digitized on profile GXT-5100 and a water velocity of 1.5 km/s. Phases from all the layers beneath, including, the crustal and mantle layers, have been identified, picker and used for modeling (Figs. 6–10). There is a good agreement between calculated traveltime curves (colour curves) and the picked coherent events interpreted as refracted and reflected phases through velocity layers. Fig. 7, for example, shows the part of the final layered velocity model in part constrained with OBS 11 data, which are also shown together with the corresponding picked arrivals and traced rays. Converting model boundaries from depth to TWTT and correlating them with reflections observed on MCS profile GXT-5100 resulted in additional constraints for the layered velocity modeling.

5.2.3.1 Sedimentary sections

Prominent reflected phases can be observed for the base boundaries of the second and the third sedimentary layer from the top (blue and brown curves, respectively; Fig. 6). Refracted phases from the third and sixth sedimentary layers appear consistently as first arrival (brown and purple lines, respectively) while the others are mostly second arrivals. This suggests that there is a substantially higher velocity sedimentary layer package (>> 3 km/s) underlying one that is lower in velocity (<< 3 km/s) as shown in Figure 6.

5.2.3.2 Crustal sections

The basement top boundary is constrained by the interpreted basement top from profile GXT-5100. The refracted phases from the upper crustal layers are in general poorly defined and are mostly interpreted as a farther, hence deeper, continuation of the refracted phase from the sediment above, and in other cases, are observed with large uncertainty as weak arrivals with amplitudes just above the noise levels. Nevertheless, the recorded refraction and reflection patterns show complexities that suggest along-strike variations in the crustal structure. While the crustal velocities eastward of OBS 4 are more typical of oceanic crust, those to the west are not typical of either continental or oceanic crust, as expected for the transitional crust (Fig. 8). For the oceanic zone to the east, the lower crustal velocity layer (a.k.a. oceanic layer 3) is well constrained by first arrivals up to ~30 km offset distance (cyan line; Fig. 8). A strong and sharp wide-angle Moho reflection (P_mP; cyan curve) is also observed and constrains the depth of the Moho. Such phases are very different to the west.

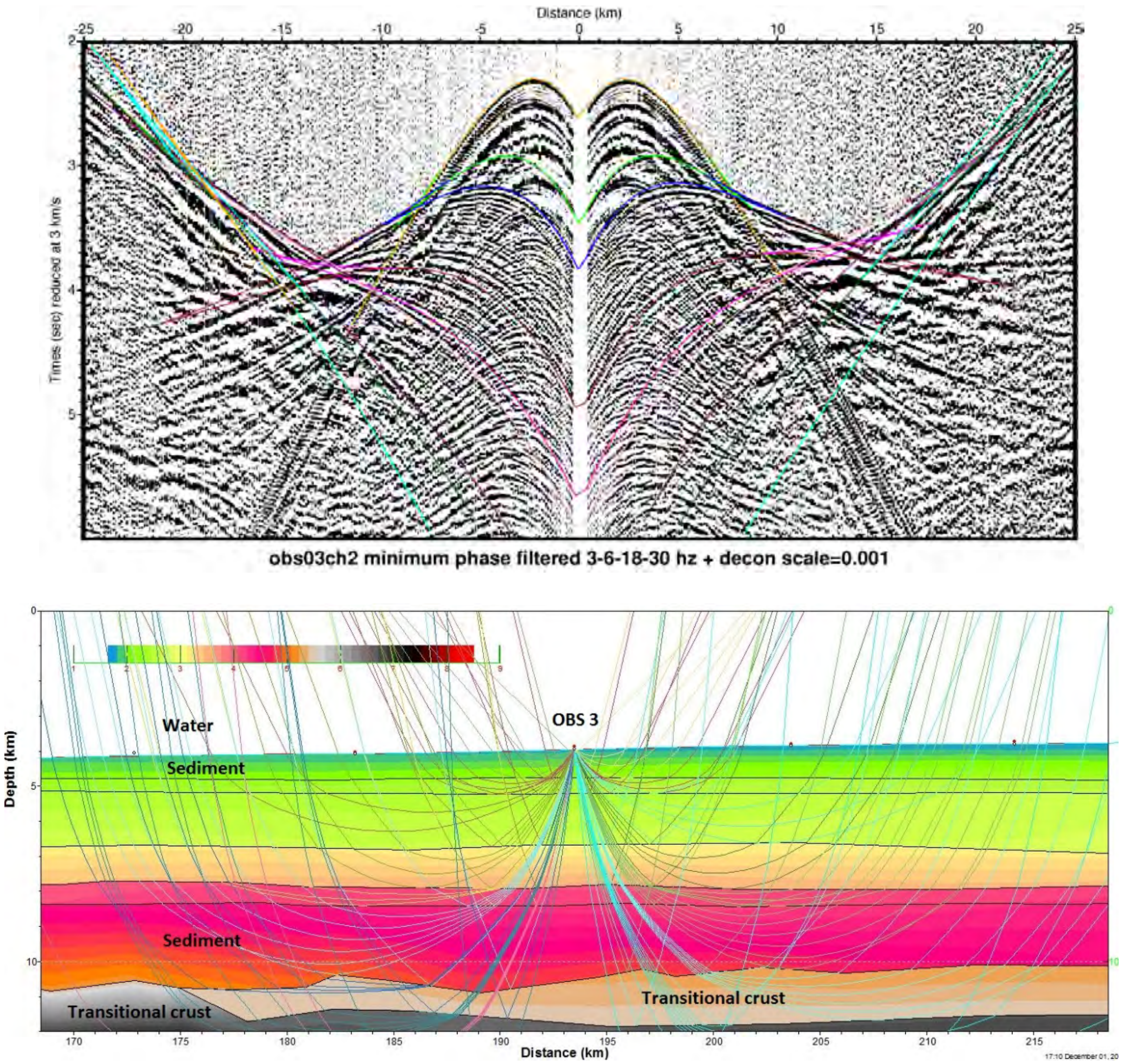

Figure 6. (Top) Plot of data from OBS 3 with overlay by calculated traveltime curves (colour curves) from ray tracing through the final layered velocity model. The scale of the plot and a reduction velocity of 3 km/s are chosen to show the sedimentary phases more clearly. (Bottom) Ray diagram from ray tracing for OBS 3 to produce the traveltime curves shown in the top diagram. The velocity model is given as color background and the color scale is in km/s.

Within the transitional zone, the velocities and character of the crustal phases change from one OBS to another. For OBS 4, the crustal phases on the western side join smoothly with the mantle phases (red and orange lines; Fig. 8). This suggests a structure with smooth transition in velocity from the basement to the mantle (hereafter Trans-1). This pattern is also observed at the western side of OBS 11 (Fig. 7) but with a twist that the upper crustal refracted phase (green line) is also observed though is weak (hereafter Trans-2). However, on the western side of OBS 8 (Fig. 9), both the upper and the lower crustal refracted phases are distinctive from that of the mantle (hereafter Trans-3). Note that the lower crustal phase velocity (~6 km/s) is slower than that of the

Layer 3 at OBS 4 (> 6 km/s; Fig. 8). The Trans-3 structure is also observed at OBS 20 (Fig. 10) and shows strong wide-angle reflections from the mid-crustal boundary (green curve) and Moho (blue curve), which constrains their depth.

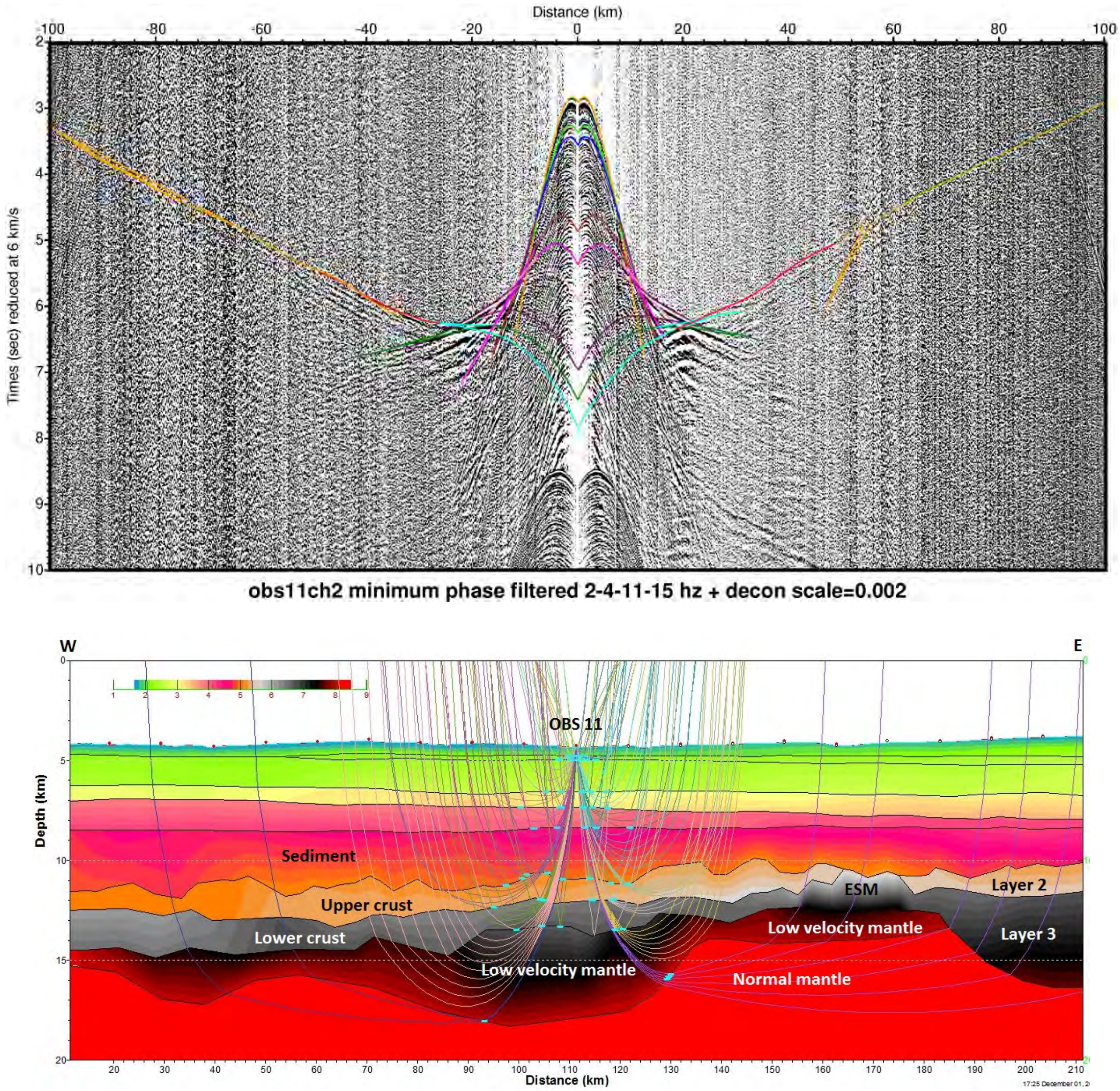

Figure 7. (Top) Plot of data from OBS 11 with overlay by calculated traveltime curves (colour curves) from ray tracing through the final layered velocity model. The scale of the plot and a reduction velocity of 6 km/s are chosen to show the crustal phases more clearly. See Figure 1 for map location of the OBS. (Bottom) Ray diagram from ray tracing for OBS 11 to produce the traveltime curves shown in the top diagram. The velocity model is given as color background and the color scale is in km/s. Model layers are labeled with preliminary interpretation for identification purpose. EMS - exhumed serpentinized mantle.

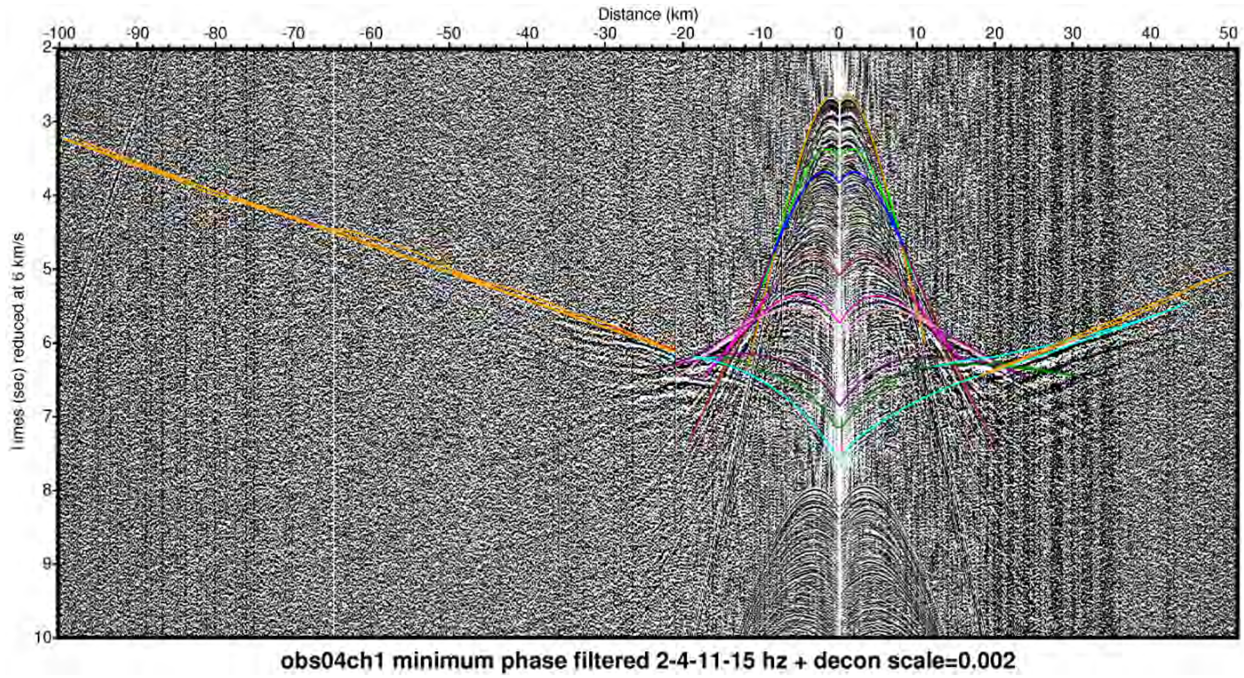

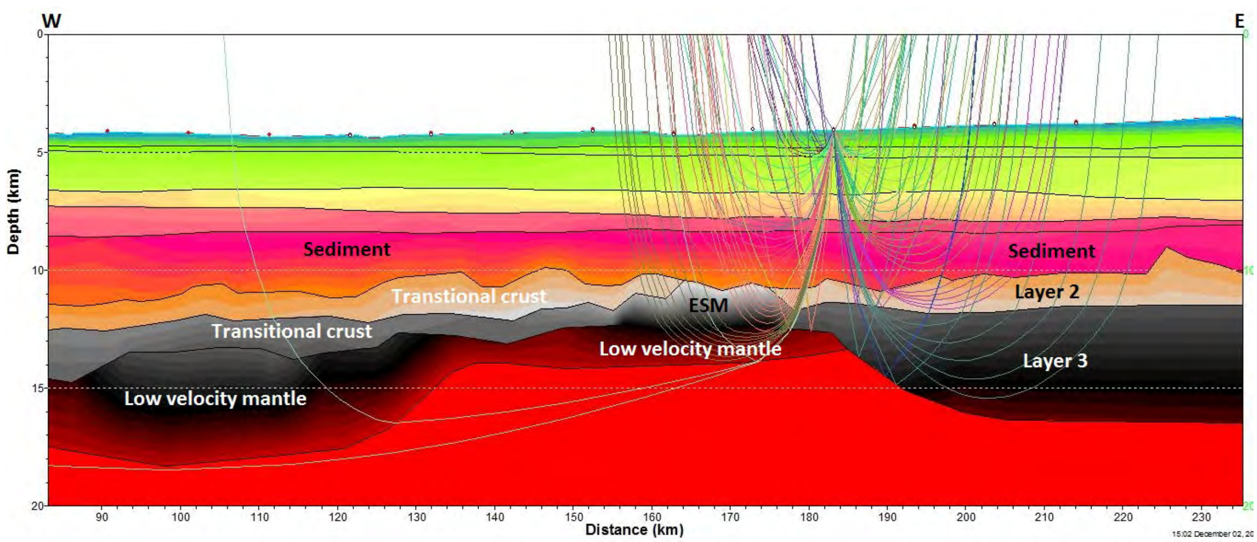

Figure 8. (Top) Plot of data from OBS 4 with overlay by calculated traveltime curves (colour curves) from ray tracing through the final layered velocity model. The scale of the plot and a reduction velocity of 6 km/s are chosen to show the crustal phases more clearly. (Bottom) Ray diagram from ray tracing for OBS 4 to produce the traveltime curves shown in the top diagram. The velocity model is given as color background and the color scale is in km/s.

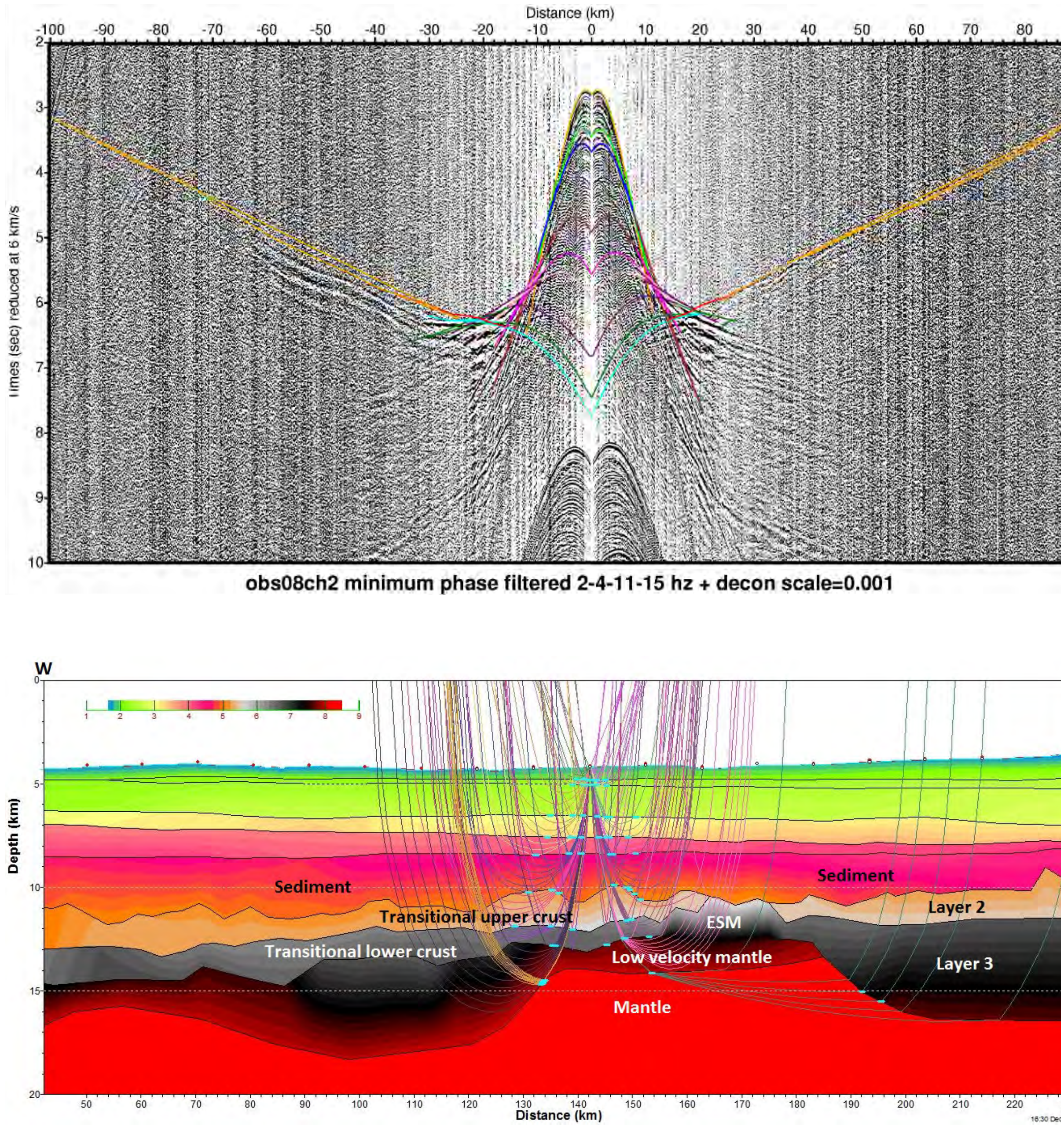

Figure 9. (Top) Plot of data from OBS 8 with overlay by calculated traveltime curves (colour curves) from ray tracing through the final layered velocity model. The scale of the plot and a reduction velocity of 6 km/s are chosen to show the crustal phases more clearly. (Bottom) Ray diagram from ray tracing for OBS 8 to produce the traveltime curves shown in the top diagram. The velocity model is given as color background and the color scale is in km/s.

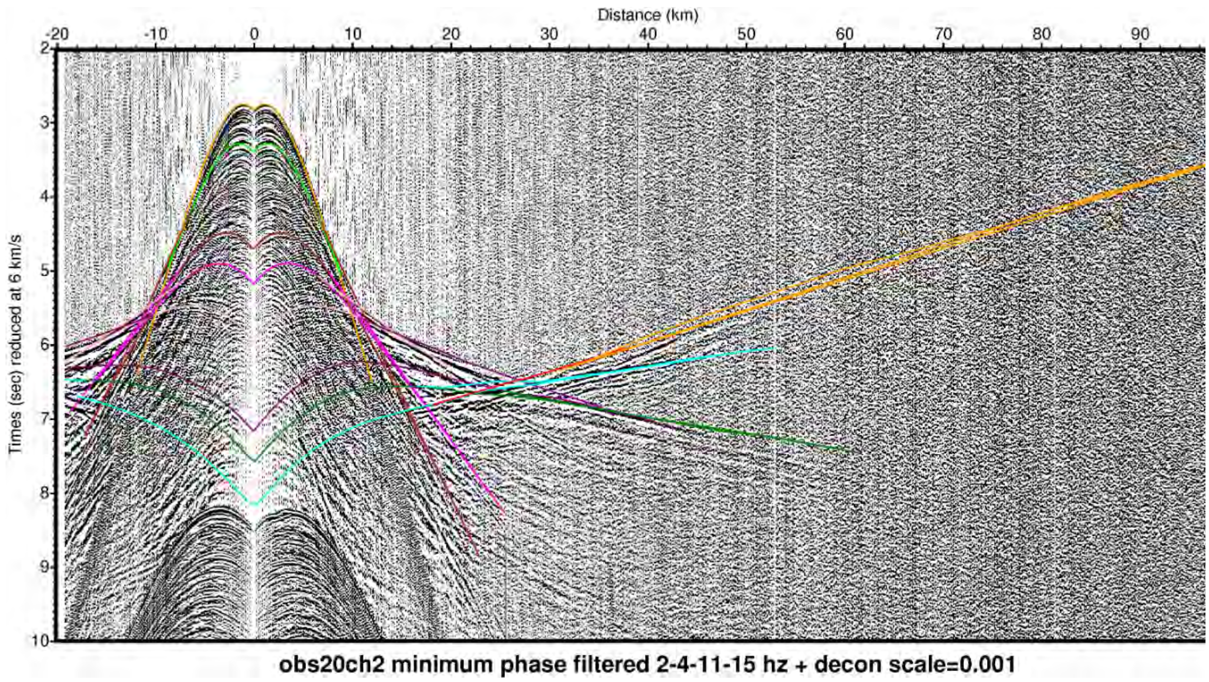

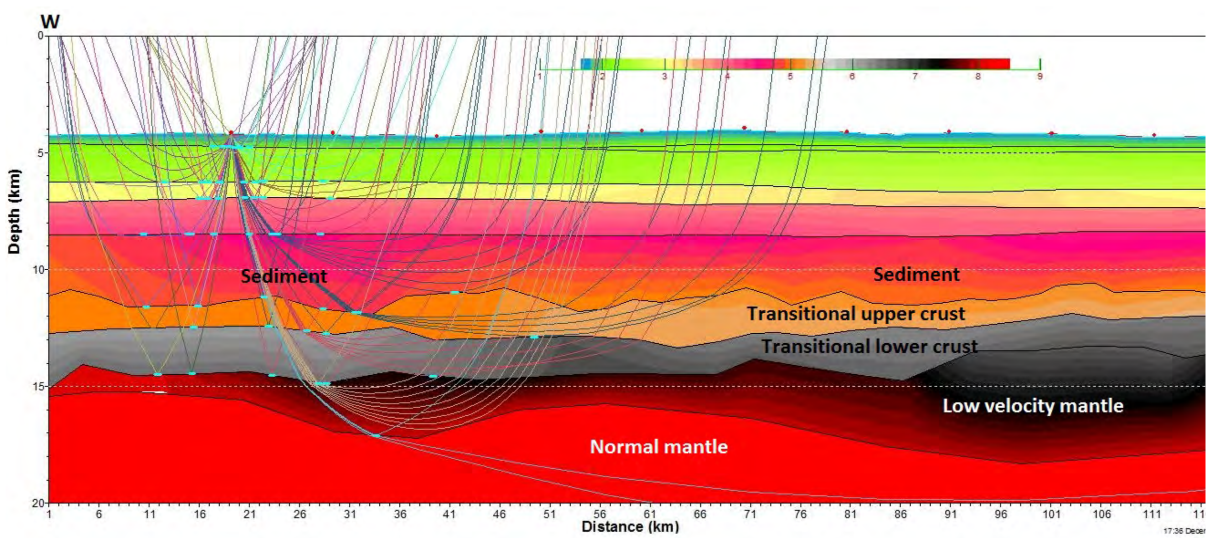

Figure 10. (Top) Plot of data from OBS 20 with overlay by calculated traveltime curves (colour curves) from ray tracing through the final layered velocity model. The scale of the plot and a reduction velocity of 6 km/s are chosen to show the crustal phases more clearly. (Bottom) Ray diagram from ray tracing for OBS 20 to produce the traveltime curves shown in the top diagram. The velocity model is given as color background and the color scale is in km/s.

5.2.3.3 Mantle

Within the transitional zone, westward of the oceanic zone, a relatively high amplitude refracted phase with higher phase velocities than interpreted for the lower crust is observed as the first arrivals (red lines; Figs. 6-10). The timing of this phase also constrains the depth of Moho. To fit this phase, a layer of relatively high velocity gradient is required with velocities ranging from 6.7 km/s to 8.0 km/s. This velocity structure is not typical of crust and is likely caused by uppermost mantle layer with velocities that are reduced by serpentinization. The thickness of this layer is constrained by the timing of the normal mantle phase (P_n; orange lines) with a phase velocity of ~8.0 km/s. This phase depicts a low-velocity gradient and exhibits a low signal-to-noise ratio.

5.2.4 Arrival picking

After the completion of the preliminary model based on visual fitting between calculated and observed arrivals, we carefully picked all the observable phases that had been modelled (Fig. 11). This was carried out on all 19 OBSs with observable data. Pick uncertainties (10–150 ms) are dependent on the frequency response function, the required processing to observe the signal and on the signal-to-noise ratios of the picked data. In general, the later (deeper) the arriving phases, the larger the uncertainties.

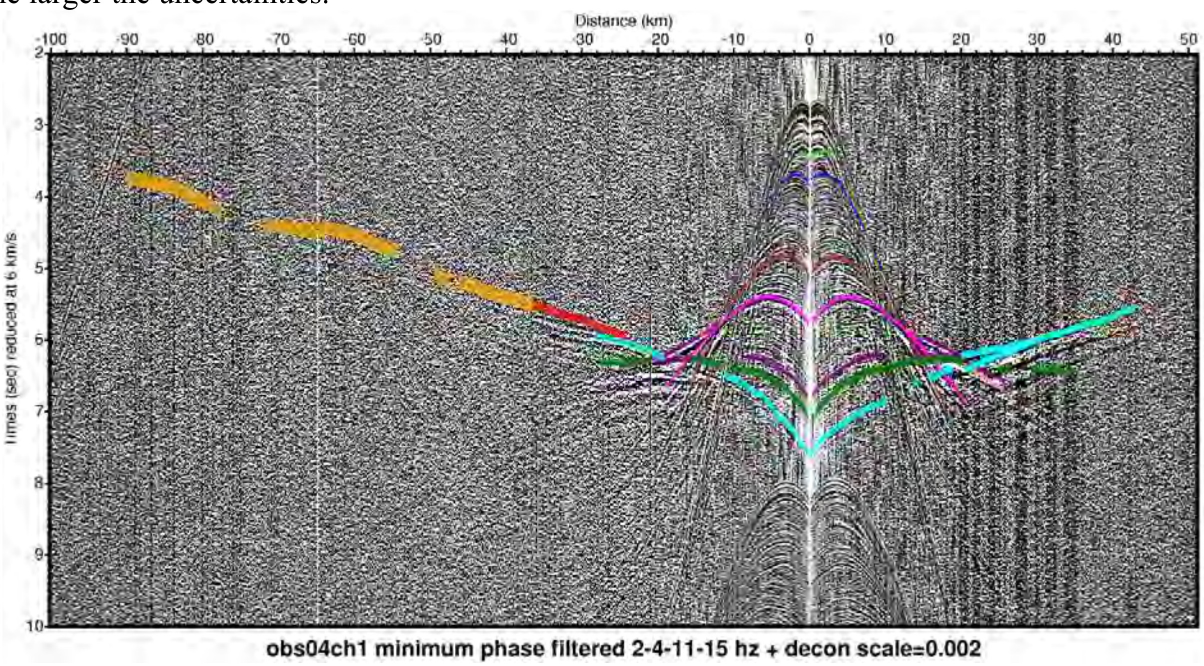

Figure 11. Picks of observed phases on data of OBS 4. Height of picks corresponds to pick uncertainties.

5.2.5 Localized inversion

By using the picks as input data and the preliminary velocity model as the starting model, we inverted the traveltimes using RAYINVR to produce the final layered velocity model. This was done one layer at a time, from top down. Only phases that are most relevant for the inversion of the layer in question were used. That is, when the velocities and the boundary depths of a particular layer are being inverted, the reflected phases from the top and the bottom boundaries and the refracted phase through the layer are used. The resulting model is, statistically speaking, the best fit to the traveltime picks in the framework of the starting preliminary model. The picked times are often different from what was visually determined when fitting to produce the preliminary model due to enhanced image information and more careful observations while picking. Therefore, picking not only provides means for error analysis. It also allows creation of a more accurate model through inversion. The root-mean-square misfits were improved by the inversion for almost all layers.

5.2.6 Final model

Figure 12 shows the resulting final P-wave layered velocity model of the OCTOPUS profile after the inversion. The velocity model shows that the velocity structures within the sedimentary layers are laterally uniform. However, for the deepest sedimentary layer, the velocities are lower towards the east. Such uniformity is, however, in contrast with the crustal and mantle velocity structures underneath. First, crystalline structures show two distinctive crustal zones as transitional and oceanic. The crust eastward of model distance 185 km displays oceanic Layer 2 velocities (5.2–5.5 km/s) in the upper domain and Layer 3 velocities (6.5–7.6 km/s) in the lower domain. The crustal thickness is 3–7 km. Note that the bottom part and the far eastern end of the crust are unconstrained due to the lack of ray coverage (Fig. 13).

Second, the model shows that the crustal structure westward of the oceanic zone is highly complex with very thin crust (0–4 km). We distinguish three different velocity patterns within the transitional zone and call them Trans-1, Trans-2 and Trans-3. For Trans-1, the velocity model suggest a pinch out of the upper crustal layer and an exhumation of a transitional crust (165–175 km distance) that has very high velocity gradient at the top (velocities ~5.5–7.4 km/s) as the counterpart of the lower crust at the two sides. Since this part of the transitional crust display no velocity discontinuity with the low velocity mantle layer underneath (velocities ~7.4–8.0 km/s), it may possibly be exhumed serpentinized mantle (ESM). The top boundary of the buried sides of the ESM body also coincides with observed reflections in the GXT-5100 profile (Fig. 14).

Westward at model distances 100–112 km (Fig. 12), the Trans-2 lower crust (6.3–6.7 km/s) is also continuous in velocity with that of the low velocity mantle (6.7–8.0 km/s) and their gradients are similar. In other words, the boundary that separates the two layers is artificial. Therefore, the lower crustal velocities may represent those of serpentinized mantle as do those underneath. Unlike in Trans-1, the serpentinized mantle of Trans-2 is not exhumed but lies underneath an upper crust of very low crustal velocities (5.1–5.3 km/s) relative to the layers underneath. Note that this structure also exhibits the greatest depth (18 km) to the top of the normal mantle.

The rest of the transitional zone is characterized by the Trans-3 structure (not labelled in Figure 12) which includes a low gradient, low velocity upper crust (velocity ~5.0–5.5 km/s) and a low gradient high velocity lower crust (velocity ~6.1–6.8 km/s) overlying with a velocity jump to a slightly low velocity mantle layer (Fig. 12). The lower crust is, therefore, more likely to be comprised of mafic rocks from melt than by serpentinized mantle rocks. The Moho (base of mafic crust) for this structure also coincides with a strong reflector observed in the MCS section (Fig. 14). The velocity of the mantle underneath is 7.5–8.0 km/s except for the area surrounding the Trans-2 structure where it is slightly lower.

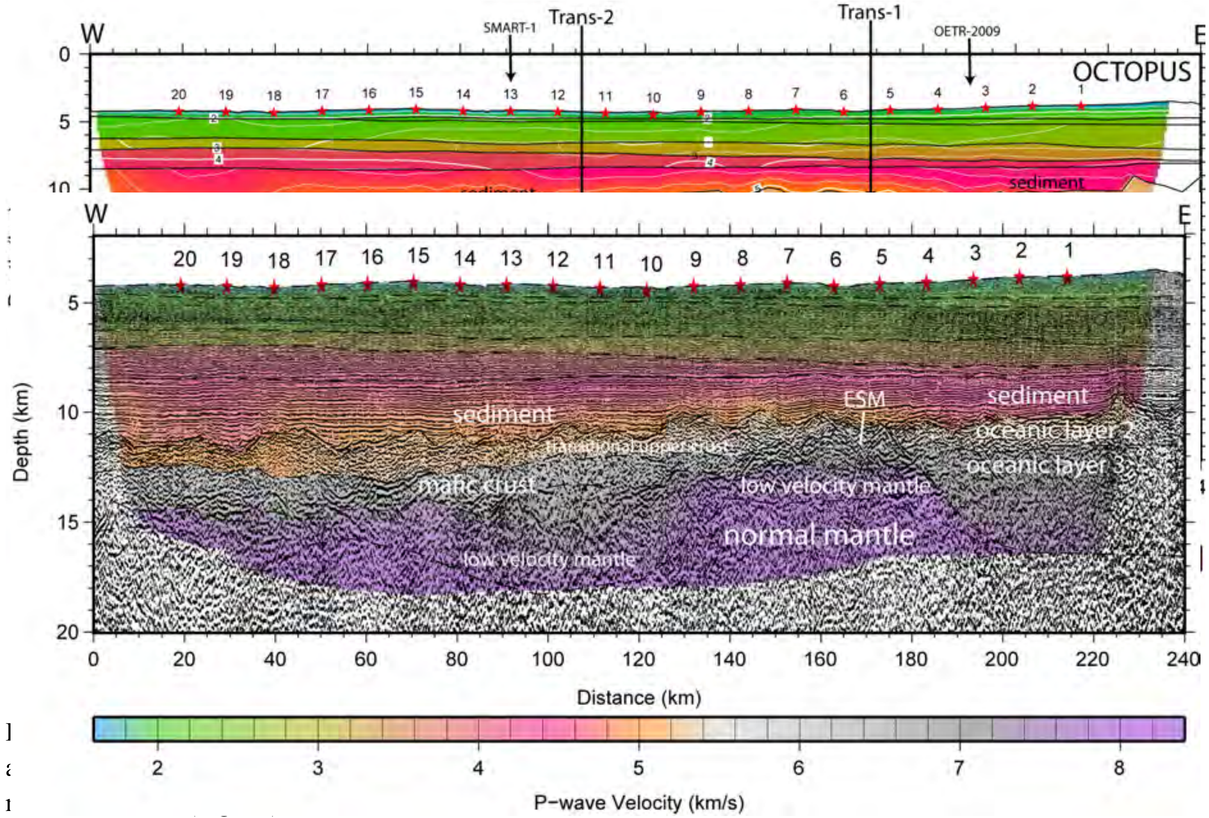

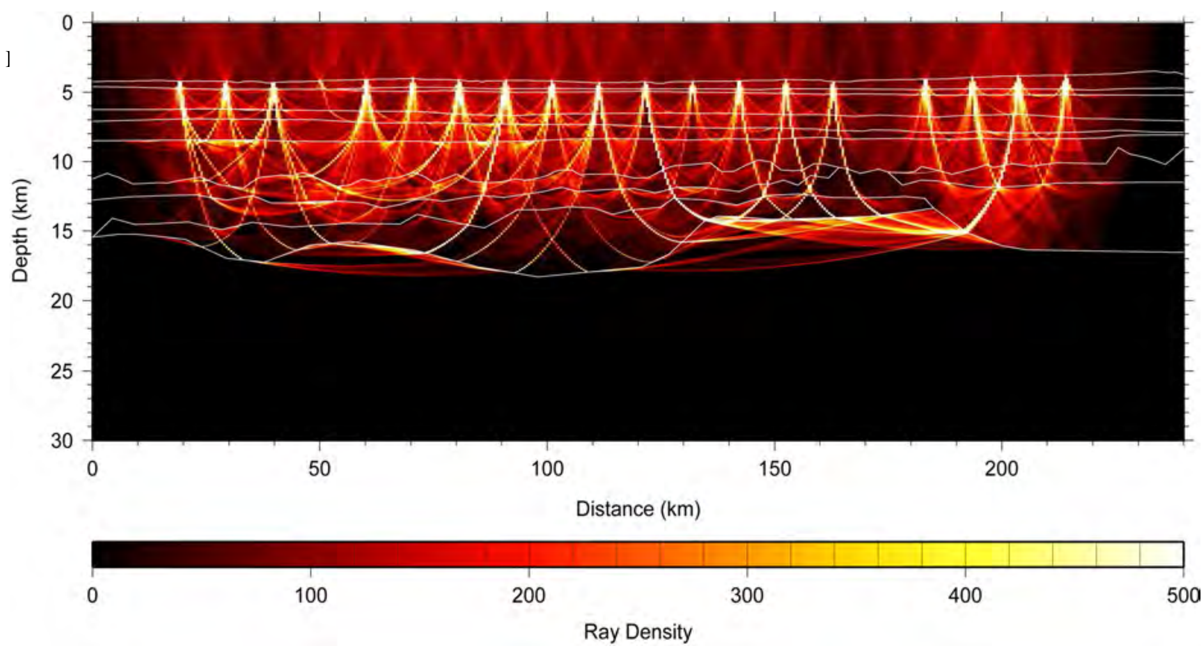

Figure 13. Illumination diagram showing ray counts in colour scale (truncated at 500 rays). Only rays used for inversion are shown. White lines are model boundaries.

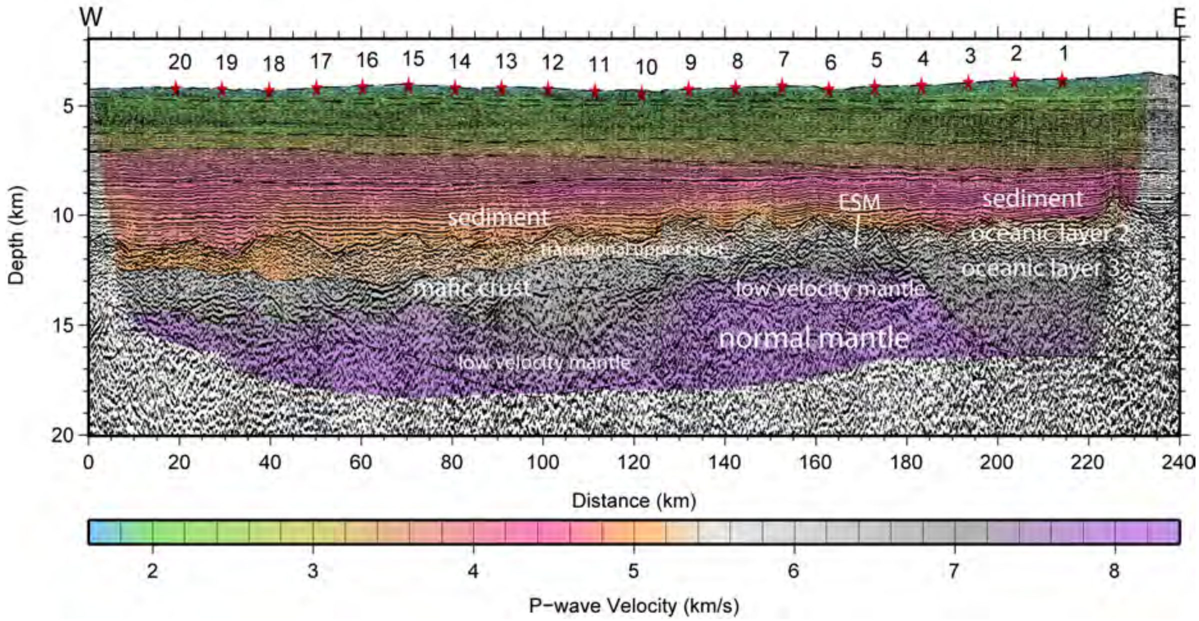

Figure 14. GXT-1500 MCS reflection image converted to depth using the final OCTOPUS velocity model (Fig. 12) superimposed on the same velocity model. Dashed lines are wide-angle model layers boundaries.

5.2.7 Error analysis and resolution test

Error analysis statistics (Table 3) and resolution plots (Fig. 15) are generated in the same manner as for the OETR-2009 model. Table 3 shows that our model as a whole has $\chi^2 = 0.769$. This means that the model fits the observations within picking uncertainties. Even for the few individual phases that show larger values of χ^2 than the others (e.g. P_{S1} & P_{C1}), the χ^2 is only slightly larger than the targeted value of 1. The number of ray-traced picks (n) is also provided to show the amount of constraints from different phases.

The resolution for different parts of the model is indicated by the diagonal values of the resolution matrix (Zelt & Smith 1992) for each velocity (Fig. 15a) and depth node (Fig. 15b). The sedimentary velocities and boundary depths are predominantly well resolved (resolution > 0.5). The velocities of oceanic layer 3 and the upper and lower transitional crust at 25–90 km distance also show relatively good resolution (~ 0.5). Therefore, constraints of both transitional and oceanic crustal zones are mostly good. The thicker sections of the low velocity mantle layer and the normal mantle also show good and even excellent resolution, respectively. However, due to the high velocity gradient and the small thickness of the majority of the transitional crust, ray coverage is poor in this area (Fig. 13) and leads to low resolution (<< 0.5). This problem is a well-documented characteristic of magma-poor transitional zones and can be resolved by placing more receivers (a denser arrays) when surveying. This implies that some caution is needed when interpreting the transitional crust. Note also that the base of the low velocity mantle layer is non-reflective and only serves as an artificial boundary to mark a vertical change in velocity gradient.

Table 3. Error analysis statistics for picked OBS: number of raytraced picks (n), mean uncertainty for all input picks ($t_{uncertainty}$), RMS residual between modeled and observed traveltimes (t_{rms}) and normalized (χ^2).

	Phase	n	mean $t_{uncertainty}$ (s)	t_{rms} (s)	χ^2
Sediment	P_{S1}	140	±0.020	0.026	1.587
	$P_{S2}P$	1779	±0.018	0.013	0.477
	P_{S2}	303	±0.017	0.018	1.054
	$P_{S3}P$	1432	±0.020	0.018	0.881
	P_{S3}	1306	±0.023	0.019	0.704
	$P_{S4}P$	3794	±0.028	0.027	0.867
	P_{S4}	831	±0.030	0.035	1.22
	$P_{S5}P$	3229	±0.030	0.030	1.027
	P_{S5}	1155	±0.031	0.016	0.29
	$P_{S6}P$	2425	±0.032	0.032	1.06
	P_{S6}	3205	±0.032	0.025	0.575
	P_BP	2451	±0.038	0.028	0.56
Crust	P_{C1}	1900	±0.060	0.060	1.414
	$P_{C2}P$	3675	±0.050	0.042	0.681
	P_{C2}	1922	±0.045	0.036	0.846
	P_mP	3833	±0.054	0.045	0.658
Mantle	P_{n1}	1522	±0.059	0.037	0.477
	P_{n2}	3732	±0.087	0.063	0.635
All		38634		0.038	0.769

5.2.8 Comparison with dip profiles

Based on our velocity models, OCTOPUS profile intersects OETR-2209 profile within what is likely to be the oceanic domain and the SMART-1 profile, slightly westward, at what seems to be the Trans-2 structure of the transitional domain (Fig. 12). Figure 16 compares 1-D velocity profiles from the OCTOPUS final model with that of the OETR-2009 and SMART-1 models extracted at the location of their intersections.

Figure 16a shows that the SMART model and the OCTOPUS model share similar velocity structures for layers above the base of the upper crust (13.5 km on both models). Between the upper crust and normal mantle, the SMART model shows a single layer of interpreted serpentinized mantle with a large velocity jump from 5 to > 7 km/s across the top boundary. For OCTOPUS, the same depth range is shown to be comprised of two layers with a less dramatic jump in velocities across the layers but higher gradient within each layer. This difference may simply be a result of modeller preference and can only be resolved by comparing actual data from the two profiles. Despite the difference, both models show a prominent low velocity mantle layer. However, without comparison with the SMART-1 data, it is challenging to conclude at this stage whether the modeled anisotropy is real.

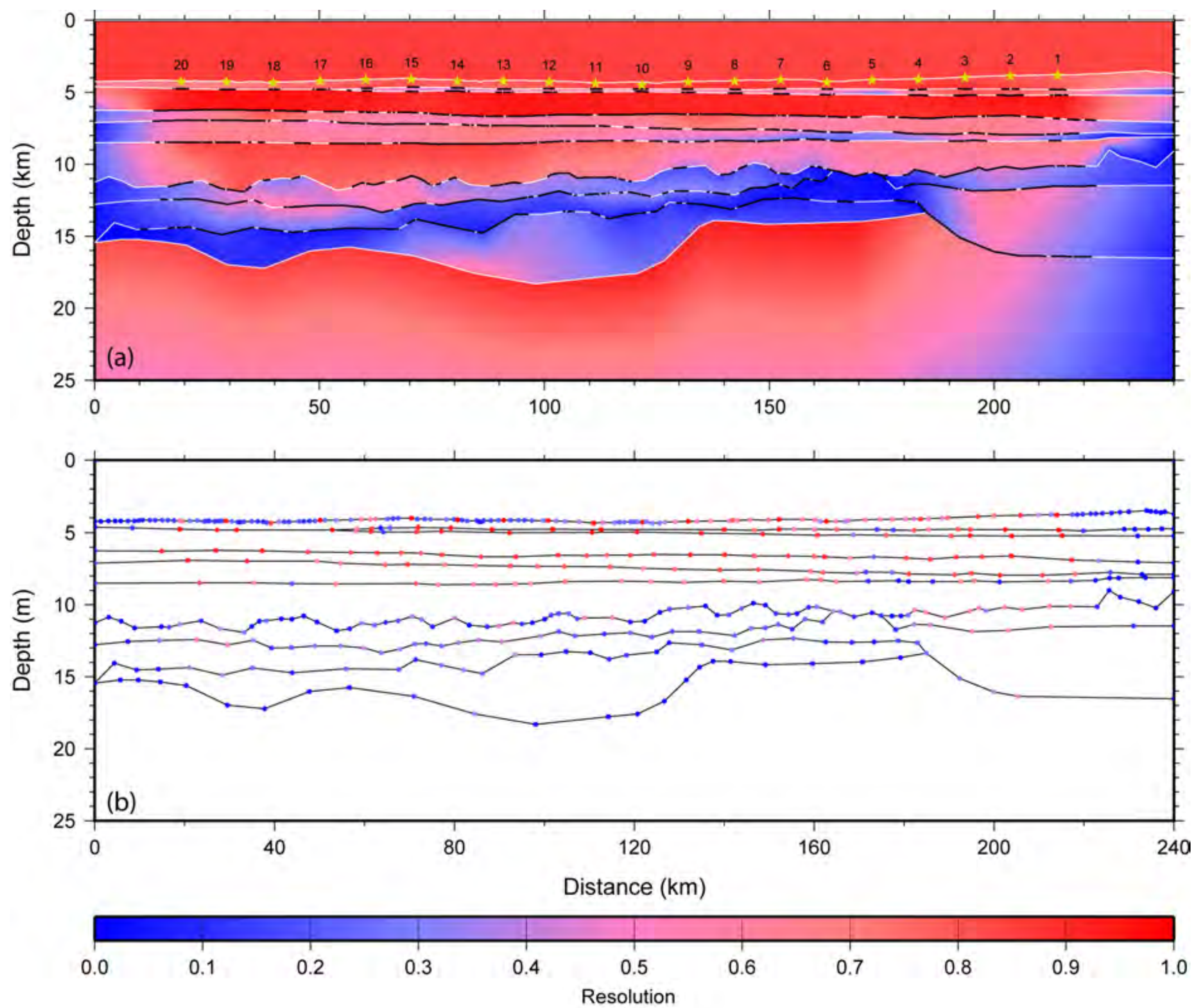

Figure 15. Model resolution plots. (a) Colour scale shows gridded diagonal values of the resolution matrix for all velocity nodes. Note that values for areas between layer boundaries are linearly interpolated from values along the boundaries. Black lines represent locations of layer boundaries illuminated by picked reflections and white lines are locations without observations. See caption of Fig. 3a regarding model layer names, crustal zonal interpretations and OBS symbols. (b) Depth resolution of velocity model boundaries. Black lines are velocity model layer boundaries. Colour-scaled circles are diagonal values of the resolution matrix of the depth nodes.

Figure 16b also shows close agreement between the OCTOPUS model and the OETR model. The major difference is within the lower part of the oceanic Layer 2 and the upper mantle according to the OCTOPUS model (13–17 km) as a layer of low velocity mantle is modeled instead in the OETR model. Here, modeller preference does not apply. The reason may be that the intersection point is near to the seaward end of the low velocity mantle layer and so the orientation of the profile may be a factor to determine whether the rays will hit or miss this layer. This complicates a possible anisotropy study at this location.

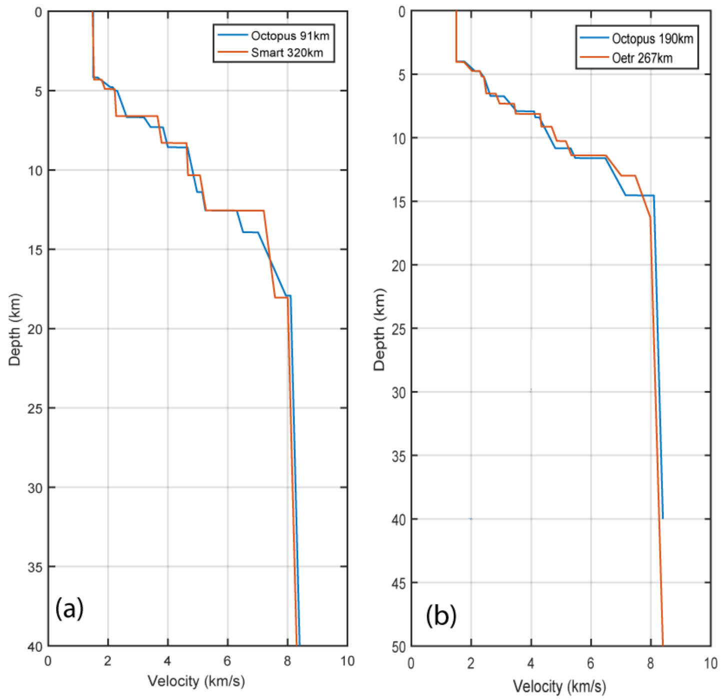

Figure 16. 1-D velocity profiles from (1) the SMART-1 model and (2) the OETR-2009 model are plotted together with those from the OCTOPUS model at tying locations. See legends for model distance at which the velocity profiles are extracted.

5.3 Synthesis of results

Figure 17 shows the geometrical basis for a regional synthesis of results from analysis of the OETR-2009, SMART-1 and OCTOPUS wide-angle profiles. In accordance with our new results, we observe distinctive velocity structures that can be categorized into three crustal zones: continental, transitional and oceanic (Figs. 3 and 12). It is worth noting that such zonation is not obvious from the MCS reflection sections unless presented together with the velocity model (Fig. 14 in the attached manuscript in the Appendix 12.2 and Fig. 14 this text).

5.3.1 Tectonics

5.3.1.1 Continental domain

We are confident that rifted continental crust extends as far seaward as 170 km model distance, ~70 km westward from the shelf break along OETR-2009 (Fig. 3). Upper and middle crust were thinned by brittle deformation and the lower crust by ductile deformation. Most of the thinning took place beneath the seaward end of the shelf to form a 12-km deep basin filled by sediment of unknown origin. This agrees with the continental structure of the SMART-1 velocity model (Funck *et al.* 2004; Fig. 17). However, the large fault block (~25 km wide) beneath the shelf break on the OETR-2009 model is likely a local structure since it is not observed 100 km to the west on SMART-1. Alternatively, this structure may have been misinterpreted as salt on the SMART-1 profile due to the low instrument density which prevents imaging of such structures with sufficient resolution. This may also explain why the Funck *et al.* (2004) calculated gravity does not fit well with the observed one.

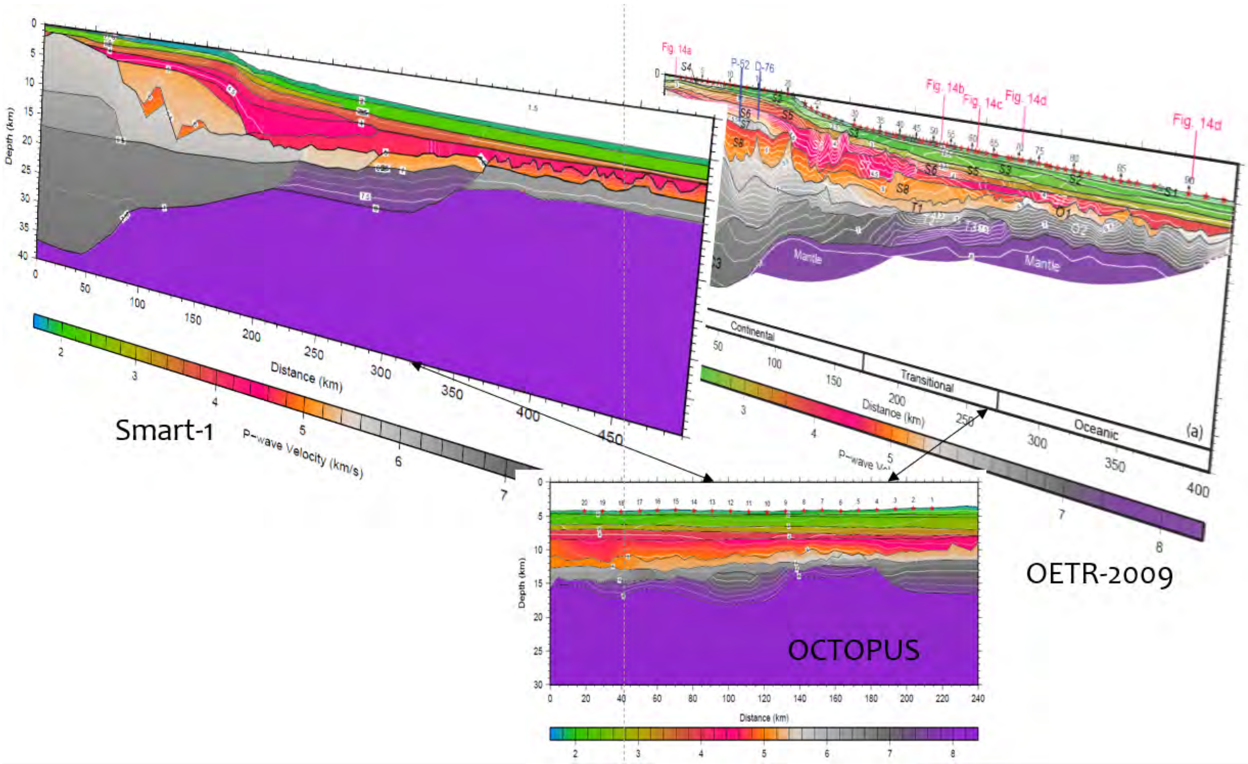

Figure 17. Velocity models of SMART-1 (Funck *et al.* 2004), OETR-2009 and OCTOPUS (this report) profiles. All models are plotted using the same colour scale and scale. The SMART-1 and OETR-2009 models are shown with a rotated perspective.

Seaward of this large basement block, the continental crustal thickness decreases more gradually seaward by more diffused deformation, resulting in a wide-rift (Fig. 3) that is typical of magma-poor continental break-up. The changes in crustal velocities seaward of 150 km distance on OETR-2009 profile, while highly resolved are, perhaps, not large enough to conclude unequivocally where exactly the continental crust ends. Furthermore, this area is characterized with an unreflective basement top shown in the MCS section, where the basement velocity is lowered to be closer to the velocity of the overlying sediments (Fig. 14 in Appendix 12.2). The underlying process that resulted in the discussed structures may be responsible for the breakup of the continental crust at ~172 km distance. Regardless of the causes, the lack of strong reflectivity makes it to accurately locate a discrete boundary between the continental and transitional crust. Even if such a boundary exists, it would represent a small contrast in velocity.

5.3.1.2 Transitional domain

The synthesis of the three models in Figure 17 helps us start to characterize and understand the formation of the transitional zone. Figure 18 shows a preliminary plan view of the interpreted crustal zones for the study area. The most prominent feature of the transitional zone is the low velocity uppermost mantle layer which is interpreted to be partially serpentinized. Along-strike variation of this layer is observed. The serpentinized mantle layer could reach its greatest width where SMART-1 profile crosses as it narrows eastward toward OETR-2009 profile, and possibly so toward west. The bottom boundary of this layer shallows toward its seaward boundary. Our OCTOPUS model also suggest that exhumed mantle is only a local feature and calls for a re-interpretation of the extent of exhumed mantle over SMART-1 profile. Since we do not observe any exhumed mantle where SMART-1 intersects with OCTOPUS (91 km), we reinterpret the serpentinized mantle on SMART-1 to be exhumed only south of OCTOPUS (Fig. 18). Note, however, that the exhumed mantle velocities are poorly resolved.

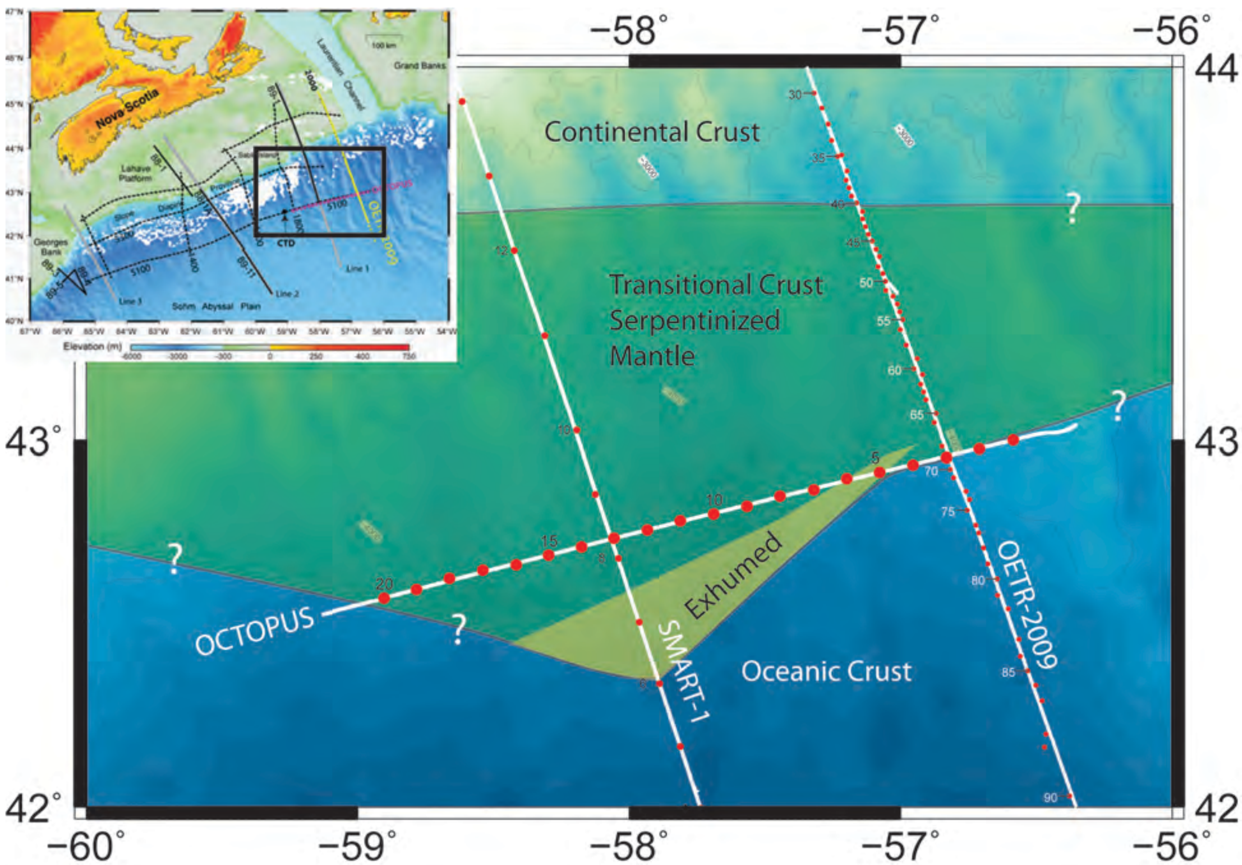

Figure 18. Bathymetry map showing a preliminary schematic map of modeled serpentinized mantle layer and exhumed serpentinized mantle. Question marks represent major unconstrained portions of the boundaries.

The OCTOPUS results (Fig. 14) also show that the transitional zone is highly heterogeneous along strike. The velocity of the upper transitional crust decreases from 5.3 km/s in the north to 5.0 km/s to the southwest. Since it has a consistently large velocity contrast across the upper-to-lower crustal boundary, the upper crust is not likely to be exhumed serpentinized mantle. We interpret it to be more likely embryonic oceanic crustal layer 2 with occasional isolated continental blocks. The interpreted lower crust is even more heterogeneous as the velocity at the base produces a large contrast with the mantle underneath at some places and none at others.

Therefore, this layer is either composed of mafic crust from melt (a.k.a. ultra-slow spreading oceanic layer 3) or mafic thinned continental crust at one place and highly serpentinized mantle at others. The interpreted lower crustal mafic layer is of very limited thickness and so can allow exhumation of mantle where the embryonic crust or very thin continental crust was extended amagmatically. Adding to the complexity, we also observe two different transitional crustal patterns along the dip profiles (Transitional-1 and Transitional-2).

5.3.1.3 Oceanic domain

The three models show that a sharp boundary appears exist between the transitional zone and the normal oceanic crustal zone (Fig. 17). The oceanic crust is much thicker than the ultra-thin crustal layers landward. There is, however, a small discrepancy between the whole oceanic crustal thickness of OETR-2009 (~3–6 km) and that of SMART-1 (3–5 km). This can be a result of differences in velocity structures although both support an interpretation of oceanic crust. Our oceanic crustal model is well constrained by closer instrument spacing and so is likely to be more accurate. According to Figure 18, seafloor spreading also started farther north on OETR-2009 than on SMART-1, suggesting an earlier onset age. The velocities of layer 3 are also slightly different among the three models (Fig. 17). It is possible that the oceanic crust formed near the boundary of the onset of seafloor spreading is mixed with serpentinized mantle to explain its higher velocities along the OCTOPUS profile.

5.3.2 Source rock

Source rocks were most likely deposited during the syn-rift to early post-rift period when basins were more restricted to allow anoxic depositional environment. And yet, water depth also plays a similar role. Since widespread salt structures are observed beneath the slope and the rise, restricted and shallow depositional environment likely existed during their formation before they were buried deep beneath a thick post-rift sequence and later migrated upward. Our model shows that the deepest sedimentary velocities (S7) are ~4.8–5.2 km/s which are too high for salt (< 4.6 km/s). According to the MCS reflectivity (Fig. 14 in Appendix), these sediments are likely pre-rift or syn-rift due to their chaotic reflection pattern. Unfortunately, the nearest boreholes are only over the shelf and are not deep enough to reach the syn-rift formations to define their rock type (Fig. 3a).

At the time when we wrote our 2015 proposal to OERA, we did not foresee a low-velocity zone beneath the shelf that is not sampled by the existing boreholes. Therefore, we proposed to comment on source rock potential by constraining the velocities of deep sediment immediately above the basement based on previous success in a similar study. Since these velocities cannot be constrained due to the presence of the LVZ, we need a new strategy for our next phase of study before we can provide further comments.

6 Dissemination and technology transfer

The dissemination of new products for this project will come after the contract is completed because additional time and effort are required to make the step from completed data analysis to publishable new products. Please note that this project is aimed at advanced analysis of high-quality OBS data and, as such, will not result in technology development per se.

7 Conclusions and recommendations

We provide our conclusions in Section 5.3 Synthesis of Results. In this section we focus on recommendations for future work.

7.1 Probing the velocity inversion below the outer shelf

Additional analysis of the data is needed for a better understanding of what is currently interpreted as a velocity inversion across the outer shelf region. This improved understanding is important because of the implications that a deep clastic sedimentary basin found below carbonate layers would have on the petroleum potential of this section of the Nova Scotia margin. We believe that improved constraints on this inversion can be obtained through an additional look at the GXT NovaSpan data combined with a sensitivity study of the OETR-2009 OBS data.

A first look at the geometry of the GXT dataset suggests that it is possible to constrain the velocities within the shelf basin using the streamer data. However, discrepancies within the Jurassic unit exist between this GXT prestack depth migration (PSDM) model and the OETR-2009 model as well as the downhole seismic model (Fig. 19). Further investigation is, therefore, needed to resolve these discrepancies. The simplest and quickest approach is to recheck the prestack depth migration work carried out with the NovaSpan data as presented in the PFA Atlas (2011) and compare and combine this information with a sensitivity study of the OETR-2009 data. The latter entails establishment of the lower and upper limits for velocities, and therefore thickness of the sedimentary basin below the carbonate layers. The existing constraints on the crustal thickness and crystalline crust velocities provide a limit for possibilities for the velocity and thickness of the deep sedimentary basin.

Reanalysis of a small part of the GXT profile 2000 would likely provide additional constraints but is time consuming. Best constraints would be obtained by waveform tomography of the OETR-2009 profile but this would require a postdoc with specialized knowledge and, therefore, additional funding.

7.2 Re-modeling data from profile MIRROR-1 on Moroccan margin

A large degree of asymmetry can be observed across the Nova Scotian-Moroccan conjugates using the most recent results from analysis of OETR-2009 and MIRROR-1 profiles (Fig. 16 in Appendix 12.2). However, despite having similar OBS density as the OETR profile, the MIRROR-1 model from the Moroccan margin is relatively simple and appears to show resolution and detail that does not agree with its small OBS spacing. We expect that reanalysis of the MIRROR data in a similar fashion as the OETR-2009 data would result in a layered velocity model of comparable detail and resolution to that presented in this work for the OETR-2009 profile. This would allow for obtaining greater and more complete insight into the rifting history of these two conjugate margins.

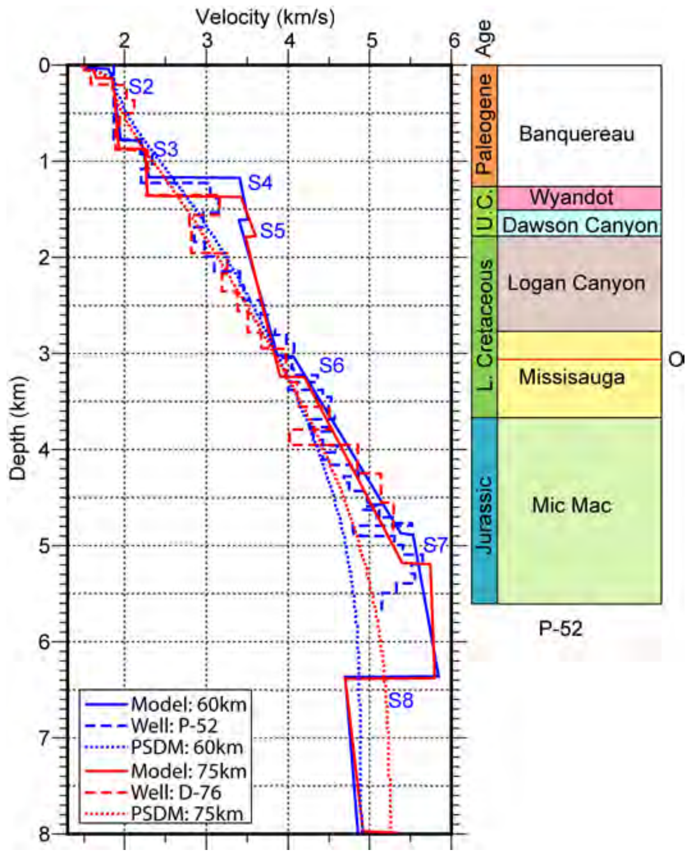

Figure 19. 1-D velocity versus depth profiles through the sedimentary layers of the final OETR model (solid lines) and pre-stack depth migrated (PSDM) velocities of GXT-2000 (dotted lines) at 60 and 75 km model distance, projected locations of wells P-52 and D-76, respectively, and their corresponding downhole seismic models (dashed line). Layers are labeled for model 60 km according to Fig. 3a. Ages and depths of stratigraphic formations and location of the O-marker (red line) are taken from previous interpretations of well P-52.

7.3 Previously proposed work

Prestack depth migration of the dense OBS OETR-2009 profile deep reflection data, as proposed originally for year 3 of this project, is expected to improve our knowledge of the crustal and mantle domains, especially about the location of layer boundaries such as, for example, is the Moho discontinuity. From other external international funds, we already managed to produce a smooth tomographic model for the OETR-2009 profile (see Appendix 12.1), which is the critically needed step toward migrating the deep reflections recorded by the OBS data. The next step is the actual migration.

8 Publications

We submitted an extended abstract (Appendix 12.1) to 15th International Congress of the Brazilian Geophysical Society held in Rio de Janeiro, Brazil, 31 Jul. to 3 Aug., 2017. We are given an oral presentation, which will be delivered by Dr. Perosi (Perosi et al., 2017). We are also planning for Dr. Lau and Dr. Perosi to attend the 5th Conjugate Margins Conference taking place in Brazil in August 2017. For this, they will both submit extended abstracts. Most importantly, we will complete writing and submit two manuscripts to major international journals. The first manuscript is based on our work on the OETR 2009 OBS data and the second manuscript is based on joint analysis of OETR 2009 and OCTOPUS 2010 OBS data. Because we are targeting major international journals that require detailed and high-quality work, this process is taking significant time. Nevertheless, we are making significant progress as shown in the Appendices where we include all the finalized figures for the first manuscript and the manuscript text we have so far. Please note that we plan to keep notifying OERA office of our progress with the manuscripts until they are published. Copies of all publications will be sent to OERA office.

9 Bibliography/References

CGPC, 1997, Natural gas potential in Canada: A Report by the Canadian Gas Potential Committee, Univ. Calgary, 113 p.

CGPC, 2001, Natural gas potential in Canada-2001: A Report by the Canadian Gas Potential Committee, Univ. Calgary, 570 p.

Funck, T., Jackson, H. R., Louden, K. E., Dehler, S. A. and Wu, Y., 2004, Crustal structure of the northern Nova Scotia rifted continental margin (eastern Canada), *Journal of Geophysical Research: Solid Earth*, **109**(B9), doi:10.1029/2004JB003008.

Gerlings, J., Louden, K. E., Minshull, T. A. and Nedimović, M. R., 2012, Flemish Cap–Goban Spur conjugate margins: new evidence of asymmetry. *Geology*, **40**(12), 1107-1110.

Keen, C. E. and Potter, D. P., 1995, The transition from a volcanic to a nonvolcanic rifted margin off eastern Canada. *Tectonics*, **14**(2), 359-371.

Kidston, A. G., Brown, D. E., Altheim, B. and Smith, B. M., 2002, Hydrocarbon potential of the deep-water Scotian Slope, *Canada-Nova Scotia Offshore Petroleum Board*, 111.

Kidston, A. G., Smith, B. M., Brown, D. E., Makrides, C. and Altheim, B., 2007, Nova Scotia Deepwater post-drill analysis 1982-2004, *Unpublished Report to the Canada-Nova Scotia Offshore Petroleum Board*, 181p.

Lau, K. W. H., Watremez, L., Louden, K. E. and Nedimović, M. R., 2015, Structure of thinned continental crust across the Orphan Basin from a dense wide-angle seismic profile and gravity data, *Geophysical Journal International*, **202**(3), 1969-1992.

Louden, K.E. and Chian, D., 1999, The deep structure of non-volcanic rifted continental margins, Philosophical Transactions-Royal Society of London Series A Mathematical Physical and Engineering Sciences, 767-799.

Louden, K. and Lau, H., 2001, Insights from scientific drilling on rifted continental margins. *Geoscience Canada*, **28**(4).

Louden, K., (2002), Tectonic evolution of the east coast of Canada, *Canadian Society of Exploration Geophysicists* “Recorder”, **27**(2), 37-48.

MacLean, B. C., and Wade, J. A., 1992, Petroleum geology of the continental margin south of the islands of St. Pierre and Miquelon, offshore Eastern Canada. *Bulletin of Canadian Petroleum Geology*, **40**(3), 222-253.

Perosi, F. A., Nedimović, M. R., Louden, K. E., Lau, K. W. H. and Watremez, L., 2017, Smooth velocity model from traveltime tomography of an offshore dense wide-angle profile in Nova Scotia: preliminary results, Fifteenth International Congress of the Brazilian Geophysical Society Extended Abstract.

Play Fairway Analysis Atlas (*PFA Atlas*), 2011, Offshore Nova Scotia Canada, *An integrated project for: Nova Scotia – Department of Energy*.

Procter, R. M., Taylor, G. C. and Wade, J. A., 1984, Oil and natural gas resources of Canada, 1983, **83**(31), Ottawa, Canada: *Energy, Mines, and Resources Canada*: Available from Canadian Government Pub. Centre, Supply and Services Canada.

Sable Offshore Energy Project Canada-Nova Scotia Benefits Plan and Development Plan Decision Report, 1997, 120.

Shimeld, J., 2004, A comparison of salt tectonic subprovinces beneath the Scotian Slope and Laurentian Fan, In: P.J. Post, D.L. Olsen, K.T. Lyons, S.L. Palmes, P.F. Harrison, and N.C. Rosen (Eds), *Salt-Sediment Interactions and Hydrocarbon Prospectivity: Concepts, Applications, and Case Studies for the 21st Century*, 24th Annual GCS-SEPM Foundation Bob F. Perkins Research Conference, Houston, p. 502-532, CD-ROM

Van Avendonk, H. J., Holbrook, W. S., Nunes, G. T., Shillington, D. J., Tucholke, B. E., Louden, K. E., Larsen, H. C. and Hopper, J. R., 2006, Seismic velocity structure of the rifted margin of the eastern Grand Banks of Newfoundland, Canada. *Journal of Geophysical Research: Solid Earth*, **111**(B11).

Wade, J. A., 1989, Petroleum resources of the Scotian Shelf, **88**(19), *Energy, Mines and Resources Canada*.

Watremez, L., Lau, K. W. H., Nedimović, M. R. and Louden, K. E., 2015, Traveltime tomography of a dense wide-angle profile across Orphan Basin, *Geophysics*, **80**(3), B69-B82.

Wu, Y., Louden, K. E., Funck, T., Jackson, H. R. and Dehler, S. A., 2006, Crustal structure of the central Nova Scotia margin off Eastern Canada, *Geophysical Journal International*, **166**(2), 878–906, doi:10.1111/j.1365-246X.2006.02991.x.

Zelt, C. A. and Smith, R. B., 1992, Seismic traveltime inversion for 2–D crustal velocity structure, *Geophysical Journal International*, **108**, 16–34.

Please note that an additional reference list is provided in the Appendices, which include the developing draft of our first manuscript. We will keep adding references as we make progress with our interpretation and add text to the Discussion section of our manuscript.

10 Appendices

10.1 Extended abstract submitted to 15th International Congress of the CBGf

10.2 Draft manuscript for JGR based on OETR-2009 profile results

Smooth velocity model from traveltime tomography of an offshore dense wide-angle profile in Nova Scotia: preliminary results

Fabio A. Perosi (Dept. of Geology/UFRJ)*, Mladen R. Nedimović (Dept. of Earth Sciences/Dalhousie University), Keith E. Louden (Dept. of Oceanography/Dalhousie University), K. W. Helen Lau (Dept. of Oceanography, Dalhousie University), Louise Watremez (Institut des Sciences de la Terre de Paris/Pierre and Marie Curie University - Paris 6)

Abstract

Understanding the mechanisms that generate rifted continental margins is important in several aspects: (1) scientific - how continents break apart; (2) geopolitical - delimitation of the territorial sea through the United Nations Convention on the Law of the Sea (UNCLOS) and; (3) economic, de-risking of oil and gas exploration. The goal of the work proposed here is to prestack migrate in a joint fashion the coincident OETR-2009 OBS and NovaSpan 2000 MCS data. To the best of our knowledge, this would be the first attempt to carry out this type of data analysis and we anticipate significant improvements in the imaging with this approach, in particular of the crystalline basement, crust and the Moho. In order to construct an accurate and detailed but smooth velocity model needed for joint prestack migration of the OBS and MCS data, we first run a detailed tomographic inversion of the OETR profile using Tomo2D software, for which we present the results here. The proposed prestack depth migration will show how velocity modeling of detailed wide-angle refraction observations (such as the OETR profile) can significantly improve the migration definition of the lower (deep) sediment and basement geometries. We also hope that our results will have an impact on the sighting of future 3D reflection surveys and exploration wells. The preliminary result of smooth velocity model shows: the depth of the Moho discontinuity is estimated to be ~30 km in the continental crust over a distance of ~60 km, rapidly rising to ~24 km at the distance of ~100 km and, gradually, rising to ~13 km at 280 km within the oceanic crustal domain, with the same depth extending until the end of the model. Between 10-80 km distance, a LVL–HVL–LVL (LVL=Low Velocity Layer, HVL=High Velocity Layer) sequence is observed. In the OCT, between 200-260 km distance, our smooth tomography model cannot resolve the layer found immediately above the Moho and interpreted in the GeoPro velocity model as magmatic underplating.

Introduction

Deep-penetration controlled source seismic data are essential for constraining the structure of a transition between the continental and oceanic crust, as are appropriate analysis of these data and subsequent result interpretation. Supporting information used for constructing a structurally reliable seismic model of an OCT (ocean-continent transition) are gravity, magnetic and well data. Recent practice of collecting coincident wide-angle ocean-bottom seismometer (OBS) and long hydrophone streamer multi-channel seismic (MCS) profiles, allows for imaging to greater depth, beyond the sediment section and through the crust all the way into the uppermost mantle.

When continents rift apart and new ocean basins form, a transition region is created between the old, thick continental crust and young, thin oceanic crust [Louden and Lau, 2001]. Based on the amount of volcanism that occurs during rifting, two primary classes of this transitional region at continental margins can develop, volcanic and non-volcanic [Louden and Lau, 2001; Keen and Potter, 1995]. Standard crustal scale MCS reflection and OBS refraction projects were carried out during the past couple of decades to better understand the ocean-continent transition (OCT) found offshore eastern Canada (Figure 1) [e.g., Funck et al., 2004; Wu et al., 2006; Louden, 2002]. The formed reflection images and velocity models [Louden and Chain, 1999; Louden and Lau, 2001; Keen and Potter, 1995; Funck et al., 2004; Wu et al., 2006; Louden, 2002, Van Avendonk et al., 2006; Gerlings et al., 2011] show significant basement structural variations between the profiles that are, together with potential field data, interpreted to indicate a volcanic-type margin offshore southern Nova Scotia, a non-volcanic margin offshore central Nova Scotia, and an extremely amagmatic margin further north. These zones of transitional crystalline crust appear to coincide with northward transitions within overlying sedimentary structures, from salt-free to salt bodies in the south, and from autochthonous salt diapirs to allochthonous salt tongues in the north [Hansen et al., 2004].

The existing knowledge about the crystalline basement structure offshore Nova Scotia (Figure 1) has been, so far, gained using sparsely spaced (100s of km) regional seismic profiles with sparsely spaced (~20 km) OBS instruments. New breakthroughs in our understanding of crustal structures offshore Nova Scotia will require new 2D OBS data with closer profile spacing (10s of km) and/or smaller instrument spacing (1-5 km) [Lau et al., 2015; Watremez et al., 2015]. Densely spaced, high-resolution OBS profile data will also require additional, more sophisticated data analysis such as are waveform tomography and prestack depth migration. Both the new data and the advanced data analysis are needed to resolve deep structures with sufficient resolution to answer first order questions such as is: What is the detailed nature of the OCT, which can exhibit complex structures, including highly extended continental crust, exposed mantle and thin oceanic crust that are difficult to distinguish with standard data and data analysis methods. Detailed imaging of these structures is critically important for an improved understanding of such widely-held concepts as the continent-ocean boundary and the breakup unconformity.The style of rifting (volcanic or non-volcanic) also has a direct implication on the rift infill and paleo-water depth at the onset of drifting [PFA Atlas, Louden et al.,2011, PFA – Play Fairway Analysis]. In magma rich conditions the rift zone is uplifted with continental and shallow marine conditions prevailing, thus allowing for the deposition of confined marine source rock. In magma poor conditions the stretching of the lithosphere induces mantle exhumation and rapid subsidence resulting in 1-2 km deep marine conditions that preclude the deposition of shallow marine source rock. The presence of such a source rock can have a direct impact on the petroleum system. The general consensus among academic researchers is that the transition from magmatic to amagmatic rifting occurs offshore south-central Nova Scotia. This view is consistent with the absence of any direct evidence for a magma rich margin, such as a continuous belt of seaward dipping reflectors (SDR) or a continuous and homogeneous East Coast Magnetic Anomaly (ECMA). However, reinterpretations by consulting companies for the PFA Atlas [2011] have found several features that they believe strongly suggest that the magma rich Camp Province could extend north up to the Newfoundland-Azores transform fault. In this interpretation, the entire Nova Scotia margin could be considered as a magma rich passive margin. This suggestion indicates that there is an urgent need for detailed data analysis of the existing OBS profiles in order to de-risk the petroleum exploration offshore Nova Scotia. The research presented here, using data from OETR (Offshore Energy Technical Research) refraction profile (Figure 1), directly addresses this need and will, hopefully, resolve the ongoing debate.

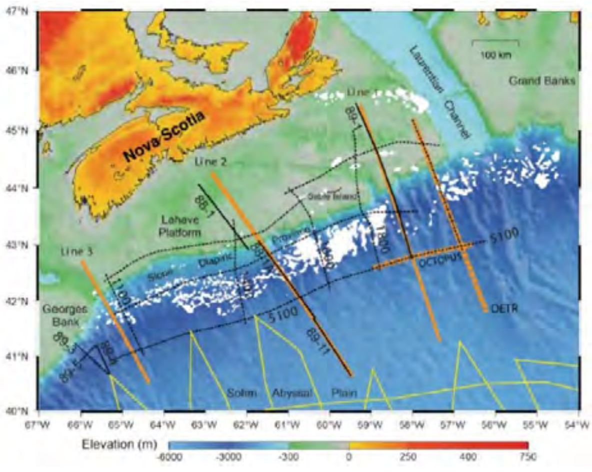

Figure 1 – Location of regional seismic lines offshore Nova Scotia. Seismic refraction profiles are marked by orange lines, dashed for OETR (NW-SE) and OCTOPUS and solid for SMART Lines 1-3 and. Regional MCS reflection lines are shown as solid black lines (Lithoprobe and Frontier Geoscience Program), dashed black lines (NovaSpan Project of ION-GXT) and yellow lines (UNCLOS Project). Jurassic salt over the Slope Diapiric Province is indicated by white patches.

Method

The purpose of tomographic inversion is detailed exploration of the velocity pattern of a medium. Such exploration is based on first arrival traveltimes obtained from a set of source-to-receiver pairs. Any geometry of sources and receivers may be considered. In our case, this was a 400 km long profile that permitted recording of refracted or diving waves and reflected waves from great depths. It is essential that the rays penetrate all parts of the area that we wish to map seismically and that the rays form a complete net, crossing all parts of the model we wish to penetrate.

Tomographic inversion requires as input picked arrivals and an initial velocity model. The tomographic inversion consists of two main steps: 1) solving the direct problem; 2) solving the inverse problem. The aim of the first step is computation of arrival traveltimes/amplitudes and corresponding raypaths. Traveltime residuals (i.e. differences between observed traveltimes and computed ones) are input information for the second step. A traditional way for solving the inverse problem is to divide the investigated region into cells and to find perturbations of the initial model, provided the perturbation for each cell is constant. Adding these perturbations to the initial model, one obtains the refined model, which reduces the traveltime residuals.

DATA AND DATA ANALYSIS

The data were collected as part of the PFA by GeoPro GmbH under contract to OETR along the pre-existing MCS reflection profile ION/GXT NovaSPAN-2000 (Figure 1). The data are stored in SEGY format and each OBS has four components: Ch1-vertical geophone; Ch2 and Ch3-horizontal geophone; Ch4-hydrophone. The OETR refraction profile (Figure 1) is 400 km long and has 100 OBS, mostly spaced only 2-5 km between stations as opposed to the typical spacing for standard surveys of 15-25 km. A few datasets have these characteristics, thus the results are expected to show significant improvements in image resolution and details captured, particularly for the crystalline basement, crust and Moho discontinuity.

The first task was to analyze the date quality and headers that contains all position information. This was in part needed in order to evaluate if there is a need to relocate the OBS, a procedure executed in Matlab that uses water depth, water velocity, deployment position, recovery position, and the direct arrivals through water layer picked on OBS data. This analysis confirmed that the original relocation exercise was carried out well except for only six OBS found at the seaward end of the OBS line, which needed improved positions at the seafloor. Data for 22 could not be recovered. However, even with this unusually large loss of data, this seismic refraction profile with 78 four-component OBS recordings is considered to have a very dense coverage.

Figure 2 shows the quality of the data in the OBS records, together with the first arrival picks (refractions with some direct waves at short offsets) and picks of reflection Moho. OBS 14 is along the shelf, OBS 39 within the ocean-continent transition zone, and OBS 65 further seaward. In the seismic section of OBS 14, rapid attenuation of the first arrivals, probably, due to a low velocity layer. This structure results in a velocity inversion. Seismic recordings for OBS 39 show clear first arrivals and several reflections (offsets -20, -35, -45-, -55 km) indicating a complex structure of the crust. In the seismic section of OBS 65, first arrivals are observed with a good signal-to-noise ratio but the reflections from the Moho are not clear.

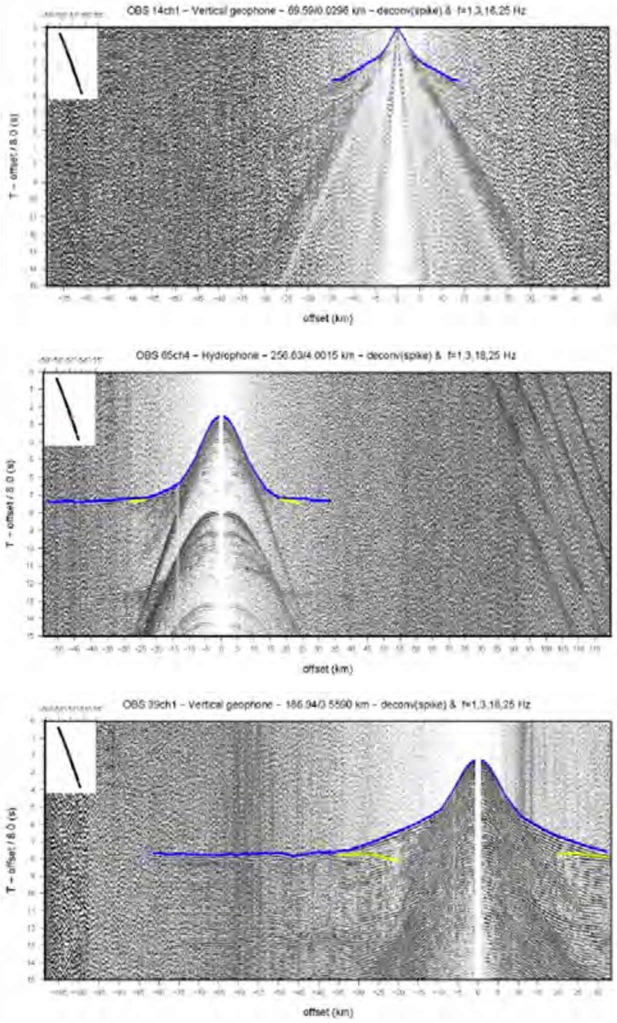

Figure 2 – Seismic sections of OBS 14, 39 and 65. The blue picks are the first arrivals, yellow picks are Moho reflection. In the upper left corner the relative position of the OBS in the seismic refraction profile is shown.

Reflection phases other than the PmP (Moho reflection) can be identified, but the joint refraction and reflection inversion using Tomo2D can utilize only one reflection phase. The PmP arrivals where chosen because they are most important for understanding the regional structure in the study area. The total number of seismic arrival picks used in the tomographic inversion was 55,899: 45,272 first arrivals (Pg – crustal refractions, Pn – mantle refractions) and 10,627 PmP arrivals. To stabilize the inversion, it was carried out in stages with picks at larger offsets added gradually.

STARTING MODELS

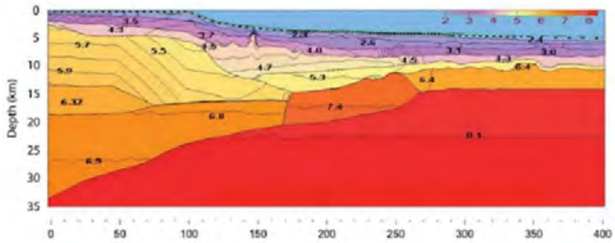

Figure 3 - GeoPro layered velocity model. Numbers in figure are P-wave velocity in km/s. The contour interval is 0.1 km/s. Triangle are OBS. (Luheshi et al., 2012).

The OETR-2009 data, used in this study, were originally used to construct a preliminary layered velocity model called GeoPro by Luheshi et al. [2012] (Figure 3). This model was a reference for the construction of the initial model to be used in Tomo2D. Two initial models were created for Tomo2D input, with the intention that the initial models are as simple as possible and with smooth velocity gradients. The first model (Figure 4) has seafloor velocity of 1.6 km/s and Moho velocity of 7.5 km/s (black dashed line is the Moho). Velocity between the seafloor and the Moho increases linearly with depth.

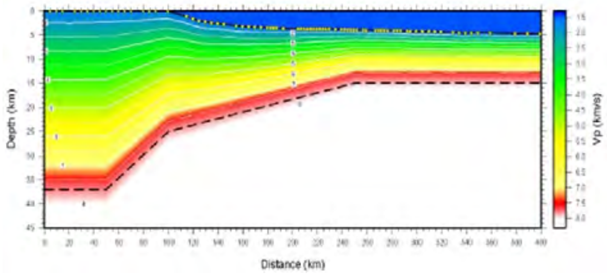

Figure 4 – Initial model, linear velocity gradient increase

TOMO2D INVERSION PROCEDURE

Tomo2D was used to carry out joint tomography inversion of refracted first-arrival traveltimes and later reflection arrivals arising from a single interface (in our case the Moho) in a sheared mesh model, hanging from the seafloor. Cells are parallelograms with the top and bottom sides parallel to the seafloor and the two other sides being vertical [Korenaga et al., 2000]. Cells in our model are 200-m wide, and their height is 200 m, 45 km beneath the seafloor, with the cell heights linearly increasing with depth. The Moho is modeled as a floating reflector with depth nodes every 200 m. Traveltime tomography using Tomo2D produces a smooth velocity model using minimum a priori information. This means that there are no velocity discontinuities anywhere in the model, including the Moho.

The forward problem in Tomo2D consists of finding the shortest raypath from the shot to the receiver for each arrival time following a hybrid approach that combines graph and ray-bending methods (Moser et al., 1992; Korenaga et al., 2000). We use a tenth-order forward star (Zhang and Toksöz, 1998) for the graph method and a minimum segment length of 1 km with 10 interpolation points per segment for the bending method (Papazachos and Nolet, 1997). Tolerances are 5×10^{-4} s and 5×10^{-5} s for the conjugate gradient and Brent minimization, respectively.

Tomography inversion (the inverse problem in Tomo2D) results in a reduction in the residuals between picked and calculated traveltimes through model updates by perturbation of velocities and depth of the interface nodes, using a least-squares regularized inversion. Parameters for the inversion were chosen, similar to the forward problem, after a full parametric study. The correlation lengths control the smoothness of the model perturbations (i.e., the inversion stability). For the velocity nodes, we use horizontal correlation lengths that linearly increase from 2 to 20 km from the seafloor to the base of the model and vertical correlation lengths that linearly increase from 1 to 10 km from the seafloor to the base of the model. The correlation length for the depth of the interface nodes is set to 6 km. Weighting parameters also control the smoothing and the damping constrains. The depth kernel weighting parameter is equal to 0.1, to favor stronger velocity perturbations relative to the interface depth perturbations. Indeed, we favor strong velocity perturbations over Moho depth perturbations because we have more picks for first arrivals than for wide-angle reflections, and their uncertainties are much lower. Finally, we set the least-squares tolerance to 1 ms.

For each iteration, the computed synthetic traveltimes are compared to the picked traveltimes, and the inversion reduces the misfit between the two sets of traveltimes by perturbing the input velocity model. The forward and inverse problems run until the misfit is reduced to a $\chi 2$ (Chi square) of approximately 1. A $\chi 2$ of 1 is achieved when the synthetic arrival times are in agreement with the picked arrival times, within their uncertainty range (Bevington, 2003). When the acceptable final model is reached, model resolution and model uncertainties are evaluated using checkerboard tests, restoration resolution tests, and Monte Carlo analysis [Korenaga & Sager, 2012; Korenaga et al., 2000].

Results

More than a hundred models were generated while searching for optimal inversion parameters for the Tomo2D tomography. Figure 5 shows the last test model with a very smooth grid of velocities, emphasizing the area where there is ray coverage. The depth of the Moho discontinuity is estimated to be ~30 km in the continental crust over a distance of ~60 km, rapidly rising to ~24 km at the distance of ~100 km and, gradually, rising to ~13 km at 280 km within the oceanic crustal domain, with the same depth extending until the end of the model. Between 10-80 km distance, at the depth of ~5 km, the same LVL-HVL-LVL feature is present below the continental shelf. In the OCT, between 200-260 km distance, our smooth tomography model cannot resolve the layer just above the Moho discontinuity and interpreted in the GeoPro layered velocity model as magmatic underplating.

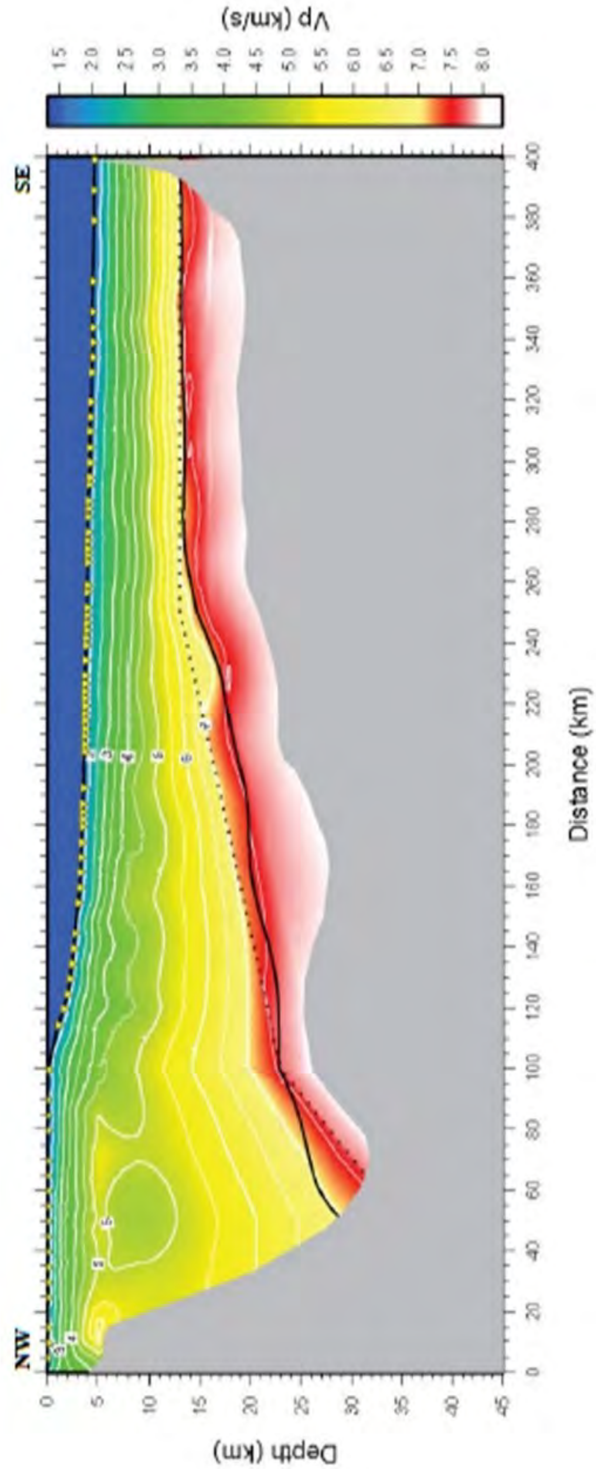

Figure 5 – Most recent preliminary result obtained using Tomo2D.

Conclusions

Despite the smoothness and simplicity of the minimum structure tomographic model produced using Tomo2D, based only on the first arrival traveltimes and PmP reflection picks (Figure 5), the inverted model is quite informative. The obtained tomographic model shows: (1)

that the original layered modeling produced by GeoPro (Figure 3) and constructed from primary and secondary arrivals, likely has utilized only a fraction of the collected data as it outlined only the most regional structures along the OETR profile, similar to what was possible to delineate by analysis of the nearby SMART 1 OBS profile [Funck et al., 2004] (Figure 1) with OBS spacing 5 to 10 times greater than for the OETR profile; and (2) that some of the regional structures in the GeoPro model were modeled incorrectly. For example, the Tomo2D model shows that the large increase in velocity on the shelf is not caused by a shallow continental crust basement, as proposed by Luheshi et al. [2012] based on the GeoPro model, but is rather due to carbonate layers, which were drilled in the area crossed by the profile [wells: Hesper P-52 and Sachem D-76]. These carbonate layers are found from 50-90 km distance along the profile at ~5 km depth. Moreover, there is a velocity inversion below the carbonates caused by lower velocity clastic sediments. Further seaward, in the OCT region between 190-270 km, the new model cannot resolve the layer immediately above the Moho, which was interpreted as magmatic underplating by Luheshi et al. [2012]. Finally, at the very seaward end of the profile and again unlike the results and interpretation of the GeoPro velocity model, the oceanic crust is characterized by a velocity gradient, suggesting that the transition from rifting to drifting likely took significant time during which anomalous oceanic crust was produced.

Completion of this smooth traveltime tomography work opens the door for what perhaps will be the most exciting stage of the proposed work, the joint prestack depth migration of OBS and MCS data.

Acknowledgments

We thank National Counsel of Technological and Scientific Development - CNPq (Process nº. 201.026/2015-5), the staff and colleagues from Department of Geology of Institute of Geosciences at Federal University of Rio de Janeiro – UFRJ and from Department of Earth Sciences at Dalhousie University.

References

Bevington, Philip R., and D. Keith Robinson. *"Data reduction and error analysis."* McGraw-Hill (2003).

Funck, Thomas, et al. *"Crustal structure of the northern Nova Scotia rifted continental margin (eastern Canada)."* Journal of Geophysical Research: Solid Earth 109.B9 (2004).

Gerlings, Joanna, Keith E. Louden, and H. Ruth Jackson. *"Crustal structure of the Flemish Cap Continental Margin (eastern Canada): an analysis of a seismic refraction profile."* Geophysical Journal International 185.1 (2011): 30-48.

Hansen, Dorthe Møller, et al. *"Development of a major polygonal fault system in Upper Cretaceous chalk and Cenozoic mudrocks of the Sable Subbasin, Canadian Atlantic margin."* Marine and Petroleum Geology 21.9 (2004): 1205-1219.

Keen, C. E., and D. P. Potter. *"The transition from a volcanic to a nonvolcanic rifted margin off eastern Canada."* Tectonics 14.2 (1995): 359-371.

Korenaga, J., and W. W. Sager. *"Seismic tomography of Shatsky Rise by adaptive importance sampling."* Journal of Geophysical Research: Solid Earth (1978–2012) 117.B8 (2012).

Korenaga, J., et al. *"Crustal structure of the southeast Greenland margin from joint refraction and reflection seismic tomography."* Journal of Geophysical Research: Solid Earth 105.B9 (2000): 21591-21614.

Lau, KW Helen, et al. *"Structure of thinned continental crust across the Orphan Basin from a dense wide-angle seismic profile and gravity data."* Geophysical Journal International 202.3 (2015): 1969-1992.

Louden, K, Lau, H, Wu, Y & Nedimovíc, M, 2011. *Refraction Crustal Models and Plate Reconstruction of the Nova Scotia and Morocco Margins. Annex 14, Play Fairway Analysis Atlas – Offshore Nova Scotia.* http://energy.novascotia.ca/oil-and-gas/offshore/play-fairway-analysis/analysis.

Louden, K. E., and D. Chian. *"The deep structure of non-volcanic rifted continental margins."* PHILOSOPHICAL TRANSACTIONS-ROYAL SOCIETY OF LONDON SERIES A MATHEMATICAL PHYSICAL AND ENGINEERING SCIENCES (1999): 767-799.

Louden, Keith, and Helen Lau. *"Insights from scientific drilling on rifted continental margins."* Geoscience Canada 28.4 (2001).

Louden, Keith. *"Tectonic evolution of the east coast of Canada."* CSEG Recorder 27.2 (2002): 37-48.

Luheshi, Matt, et al. *"The impact of conjugate margins analysis on play fairway evaluation–an analysis of the hydrocarbon potential of Nova Scotia."* first break 30.1 (2012): 61-72.

Moser, T. J., G. Nolet, and R. Snieder. *"Ray bending revisited."* Bulletin of the Seismological Society of America 82.1 (1992): 259-288.

Papazachos, C., and G. Nolet. *"P and S deep velocity structure of the Hellenic area obtained by robust nonlinear inversion of travel times."* Journal of Geophysical Research: Solid Earth 102.B4 (1997): 8349-8367.

Watremez, Louise, et al. *"Traveltime tomography of a dense wide-angle profile across Orphan Basin."* Geophysics 80.3 (2015): B69-B82.

Wu, Yue, et al. *"Crustal structure of the central Nova Scotia margin off Eastern Canada."* Geophysical Journal International 166.2 (2006): 878-906.

Zhang, Jie, Uri S. ten Brink, and M. Nafi Toksöz. *"Nonlinear refraction and reflection travel time tomography."* Journal of Geophysical Research: Solid Earth 103.B12 (1998): 29743-29757.

Continent-ocean transition across the northeastern Nova Scotian margin from a dense wide-angle seismic profile

K. W. Helen Lau[1], Mladen R. Nedimović[1] and Keith E. Louden[1]

[1]Dept. of Earth Sciences, Dalhousie University, Halifax, NS, Canada

Accepted date. Received date; in original form date

Abbreviated title: Continent-ocean transition across Scotian margin

Corresponding author: K.W. Helen Lau, Dept. of Oceanography, Dalhousie University, Halifax, NS, B3H 4R2, Canada; email: kwhlau@dal.ca; phone: +19027020188

SUMMARY

…

KEYWORDS

Continental margins: divergent; Continental tectonics: extensional; Crustal structure; North America

1. Introduction

…

2. Geological Background

…

3. Wide-angle Seismic Data

Wide-angle data were acquired in 2009 for the Offshore Energy Research Association (OERA) of Nova Scotia by GeoPro GmbH along a 405-km-long ocean bottom seismometer (OBS) profile across the northeastern Nova Scotia margin (Fig. 1). This profile (OETR-2009) is ~100 km to the east of OBS profile SMART-1 (Funck *et al.* 2004) and is coincident with multichannel seismic (MCS) profile GXT-2000, which can be tied to the SMART profiles by profile GXT-5100 in deep water (~4 km) (Fig. 1). Data useful for analysis, all with a sampling interval of 4 ms, were recorded on only 78 out of the 100 deployed OBSs. Instrument spacing ranges from <3 km across the presumed ocean-continent transition (180–300 km model distance; Fig. 1) to ~10 km at the seaward end of the profile (>360 km distance) and ~5 km for the remaining sections of the profile. Within each OBS, a group of three 4.5 Hz geophones (two horizontal and one vertical component) were mounted at the bottom of a glass sphere which also housed the seismic recording units. An external hydrophone was mounted to the top of the sphere. Only the vertical geophone and hydrophone data were used for the analysis presented in this work. A tuned array of 8 airguns (total volume = 64 L), towed at 10 m depth, was fired every 60 s to provide an average shot spacing of ~124 m.

Raw data were formatted into SEGY files for data analysis, which included noise attenuation, arrival picking and velocity modelling. Standard corrections that account for gun delay (50 ms), a receiver specific constant time delay, and the OBS clock drift were applied to the data records. Gun positions were corrected for the gun delay and the offset between the guns and the GPS antenna. The OBS positions were relocated to their seafloor positions, which were estimated by picking the direct water wave arrivals for each shot and raytracing using a water velocity profile from a CTD cast by another survey nearby (42°33.88'N and 59°05.78'W). These corrected OBS and shot positions were then used to calculate the true source-receiver offset distances.

Common receiver gathers of OBS data were plotted and coherent signals from compressional waves that underwent reflections and refractions (diving waves) through various seismic layers were picked (Figs. 2–8). Unfiltered data were used wherever possible but for deeper layers, bandpass filtering and/or predictive deconvolution were often necessary to improve the signal-to-noise ratio of the arrivals. Note that the filters used for Figs. 2–8 are optimized for the scale shown and not necessarily the ones used when picking.

Figure 2 shows an example of refracted and reflected phases (Table 1) through the shallower sedimentary layers beneath the shelf. On the basis of their apparent velocity, we divide the observed sedimentary arrivals into three major groups belonging to the following sets of layers: shallowest layers (S1–3) with phase (or apparent) velocities significantly lower than 4 km s^{-1} (the reduction velocity); deeper layers (S4–5) with phase velocity that is ~4 km s^{-1}; and the deepest layers (S6–8) with significantly higher phase velocity than 4 km s^{-1}. The reflection from the top of layer S4 layer is very strong throughout the profile, suggesting a large velocity discontinuity across the boundary. When the OBS record from Figure 2 is plotted using a greater offset range and higher reduction velocity of 6 km s^{-1} (Fig. 3), the rapid decrease and disappearance of the amplitude of the refracted phase through layer S7 at ~-22 km and ~32 km offset distances (arrows in Fig. 3) comes into focus showing a phenomenon called step-back. A step-back in the first arrivals indicates a velocity inversion, which occurs wherever a relatively low-velocity layer (LVL) is present underneath a relatively high velocity layer (HVL). When rays penetrate the LVL, they are refracted downward, creating a shadow zone. Figure 3, which displays the data recorded on OBS 12, shows an example of a shadow zone and indicates that layer S8 is an LVL. Neighbouring OBS records from the shelf region also show a similar step back in the first arrivals. Since no returning rays can be observed from this layer, no direct velocity constraints are possible using refracted phases. The wide-angle reflection from the top of Layer S8 and the offset distances at which the amplitude of the S7 refraction dies off constrain the thickness of layer S7. However, the velocity of the LVL is still weakly constrained by the moveout of the basement reflection and by assumption of continuity with adjacent sedimentary velocities on both sides. No step-backs are observed for refractions seaward of the shelf (Fig. 4).

Underneath the slope at OBS 27 (Fig. 4), the refracted phase of S6 is observed over a much wider offset range than landward, suggesting a dramatic thickening of this layer. The data also show evidence of a salt diaper within this layer on the seaward side of OBS 27. Due to the rapid changes in water depth across the record, the observed phase velocities are not a good indication of the layer velocities. For example, arrivals for layer S8 with phase velocity of ~4 km s^{-1} constrain much higher velocity of the deepest sediment above the basement. The phase for the layer above is sequentially numbered as S7 for simplicity although it has no resemblance to the same phase beneath the shelf landward where step-backs are observed (Fig. 3).

Figures 3–8 show OBS data that display velocity structures that uniquely define three crustal zones: continental (OBSs 3, 23 and 24), transitional (OBS 54) and oceanic (OBS 79). Regarding the continental crustal observations, OBS 3 (Fig. 5) shows refracted and reflected arrivals (Table 1) from three layers (C1-3) with phase velocities of 5–6 km s^{-1}. Refractions through layers C1 and C3 both have relatively strong amplitudes, while the refraction through layer C2 is weak, possibly due to scattering by the overlying complex structures. The wide-angle Moho reflection (P_mP) is normally of high amplitude at far offsets (> 90 km) but can also be traced back to near offsets to constrain the depth of Moho beneath the thick crust (~12 s two-way-travel-time, TWTT).

Figure 6 shows OBS records 23 and 24 with the crustal first breaks overall arriving later in time than the same arrivals at OBS 3 (Fig. 5), especially at the right hand side, which indicates basement deepening and crustal thinning in the seaward direction. The asymmetry between the two sides is mainly caused by the difference in seafloor depths (Fig. 6). Unlike for OBS 3, the crustal refractions on the landward side of OBS 23 are poorly defined, possibly due to shadow zones caused by complex crustal structures. Nevertheless, the mid-crustal and P_mP reflections are easily observed and constrain the crustal velocities. On the seaward side, the crustal arrivals recorded by OBS 24 appear distorted by the presence of a salt diaper at ~25–35 km offsets. The strong secondary arrivals of the C3 refraction provide the primary constraint for the velocity of this layer. Wide-angle mid-crustal and Moho reflections also constrain the crustal thicknesses. Furthermore, with a gradual increase in phase velocities from one phase to another (deepest sedimentary phase velocity ~5 km s^{-1}, layer C2 ~ 6 km s^{-1}, layer C3 ~ 7 km s^{-1}, and mantle Pn ~ 8 km s^{-1}), the first arrivals form a moderately wide “U” shape. The tighter the “U” shape, the thinner is the crust.

In contrast, farther seaward within the transitional crust, the first arrivals on the right hand side of OBS 54 (Fig. 7) are refractions which only turn in the sediments (phase velocity ~5 km s^{-1}) and mantle (phase velocity ~8 km s^{-1}) thus forming a “V” shape. This suggests the presence of extremely thin crust. The crustal refractions are only secondary arrivals and seemingly represent just an extended part of the layer S8 refraction. Nevertheless, existence of a very thin crust is confirmed by the GXT-2000 coincident reflection image, which shows a clear basement reflection at the top of layer C1 in this area, and strong P_mP reflections observed in the OBS data.

OBS 79 (Fig. 8) is located seaward of the GXT-2000 profile within the oceanic crustal zone, where structures are probed only by the OETR-2009 profile. Despite the absence of a coincident MCS reflection image in this area, geometry of the structural boundaries is well constrained because we observe numerous high-amplitude wide-angle reflections in the OBS data. The most prominent sedimentary reflection in the OBS data comes from the top of layer S7, suggesting a large velocity discontinuity (a transition from ~3 to ~4 km s^{-1}) across the boundary. The base of layer S7 (the basement reflection) can also be clearly observed, and constrains the depth and topography of the crust. The phase velocity of the refracted phase C1 (~5 km s^{-1}) is mostly a result of changes in basement topography. The refracted phase C2 is also affected by distortions caused by the basement topography, as well as that of the mid-crustal boundary. However, C2 forms first arrivals that are distinguishable from those of the upper crustal layer C1, supporting a two-layered oceanic crustal structure. The amplitude of phase C2 is observed to die off abruptly before the mantle phase (P_{n2}) indicating a large decrease in velocity gradient, as amplitude is proportional to velocity gradient. However, the apparent velocity of phase C2 increases gradually towards the bottom of this layer (larger offset distances) and transitions smoothly to P_{n2}, suggesting a minor velocity discontinuity with the mantle. Weak and intermitted appearances of P_mP can be observed to constrain the depth to Moho. Overall, this record section and those from nearby OBSs show very different velocity structure than the ones found landward (Figs. 2–7).

Strong leftward dipping first arrivals with phase velocity of > 7 km s^{-1} (P_{n1} for layer mantle-1) are observed at 26–44 km offset distances on OBS 54 (Fig. 7). Such a high phase velocity is unusual for the crust (cf. C3 of OBS 24 on Fig. 6 and C2 on OBS 79 in Fig. 8) and, therefore, is likely to come from the mantle indicating very thin (~4 km) transitional crust for the OBS 54 area. The P_{n1} phase is observed to be continuous in travel time with that of the P_{n2} phase at the far offset distances, suggesting no velocity contrast across the two phases. The sharp decrease in amplitude across the two phases (~44 km offset) further signifies a large discontinuity in velocity gradient. The P_{n2} phases with a phase velocity of ~8 km s^{-1} are well observed along the profile (Figs. 3–8), except for the two ends where offsets are restricted. Its low amplitude and frequency are characteristic of normal, unaltered mantle. The timing of P_{n2} also provide an important constraint on Moho depths (Figs. 3-6 and 8).

4. Seismic Modelling

4.1. Methodology

We use RAYINVR, the raytracing algorithm of Zelt & Smith (1992), to model the P-wave velocity by fitting the seismic arrival traveltimes layer-by-layer in a top-down approach. Location of the seafloor is determined using the two-way-travel-times (TWTTs) from the MCS profile GXT-2000 (Fig. 1) converted to depths by a constant water velocity of 1.5 km s^{-1}. For seafloor location at the seaward end of the OETR-2009 profile (south of OBS 71) that is not covered by GXT-2000 profile, we use the GEBCO_08 grid (GEBCO 2008). For consistency, these depths were first converted to TTWTs using an estimated water velocity profile from a nearby CTD cast and then back into equivalent depths for 1.5 km s^{-1} water velocity. Although constraints for velocity modeling of the sub-bottom layers come from OBS data, this modeling process is supported by information on the layer boundary location from the GXT-2000 MCS reflection image.

The fitting of forward-modeled traveltime curves to observed arrival times was initially done visually for the purpose of phase identification (Figs 2–8). Once a complete preliminary model was produced, the zero-crossing times of identified phases were hand picked with each pick being assigned an uncertainty value based on the frequency content and signal-to-noise ratio of individual wavelets (Table 2). These picks were then used for inverse modelling to form an optimally fitted final model. Due to the large numbers of phases identified from the data, we only use OBS stations that have good data quality and provide an even distribution of observations along the profile (red stars; Fig. 9). Pick intervals were subsequently decimated to a minimum of 100 m to avoid overweighting regions of dense trace spacing in the inversion and error analysis.

4.2. *P* wave Velocity Model

Figure 9 shows the final P-wave velocity model as well as the refracted and reflected rays used in the inverse modelling. For a detailed comparison with well data and previous velocity models, 1-D profiles are extracted at key locations and shown in Figures 10 and 11.

The modelled sedimentary velocities are generally consistent within the layers across the profile with the exception of a limited extent in layers S6-8 beneath the shelf (0–100 km model distances; Fig. 9a). Layers S1–3 are the youngest sedimentary layers whose velocities of 1.7–2.9 km s^{-1} are substantially lower than the velocities of the deeper layers as shown in the data in

Figure 2. The largest velocity jump (~1.2 km s^{-1}) across the bottom boundary of layer S3 is modelled beneath the shelf where two wells are located nearby and the carbonate Wyandot formation is drilled at similar depths (P-52 and D-76; BASIN database, Geological Survey of Canada, Dartmouth, Nova Scotia, Canada; Figs. 9a and 10). The OBS data require that layer S4 below is modeled with higher velocity than measured by downhole seismics in the wells (Wyandot formation). A small velocity inversion at the top of layer S5 is also needed to model a minor step back in the OBS data (Fig. 2). This minor velocity reduction is also suggested by the well data (Fig. 10). The top of layer S6, characterized by a small velocity step increase, coincides with the O-Marker within the Missisauga formation at well P-52. Beneath this boundary, velocities increase steeply into the Mic Mac formation to reach ~5.8 km s^{-1} at the top of layer S7 at distances 60–90 km. Velocities in layer S7 are nearly vertically uniform, i.e. show a low gradient. Beneath these high velocities, a low velocity zone (S8) exists within two sub-basins at distances ~25–105 km (Figs. 9a and 10). In this section of the profile, there are no first arrival constraints for layer S8 and velocities of 4.7–5.4 km s^{-1} are assigned by assumption that the velocities in this area of S8 are similar to S8 velocities modeled seaward. The velocities of 5.3–5.8 km s^{-1} at the landward end of layer S8, however, approach those of the crust (Fig. 9a).

Seaward beneath the slope, lateral heterogeneity that mimics salt diapiric structures can be modelled within layer S6 (Fig. 9a). This layer reaches a maximum thickness of ~6 km at 128 km distance, seaward of which both its thickness and velocity decrease until it pinches out at 293 km distance. The velocity of layer S7 is highest (4.8–5.2 km s^{-1}) at the slope where the overburden is thickest but decreases to a minimum of 3.7 km s^{-1} at the seaward end where the overburden is thinner. The otherwise smooth top boundary of S7 is distorted into highs by salt structures at several locations. Layer S8, the deepest sedimentary layer, has velocities of 4.8–5.3

km s^{-1} and pinches out onto the basement at 295 km distance. A structural step upward at the top of S8 is located at 185–195 km distances.

Layers C1–3 are modelled with velocities of 5.0–7.4 km s^{-1}, which are generally higher than velocities for most sediments (Figs. 9a and 11). Furthermore, the top boundary of layer C1 is constrained by the interpreted basement reflection from the coincident MCS profile (see Section 5.1). In addition to the vertical layering, the crustal layers also display two horizontal transitions in velocity indicating three distinctive crustal zones: continental (C), transitional (T) and oceanic (L) (Fig. 9a). Some of these lateral transitions resulted in development of velocity discontinuities in the model as shown in Figure 9, while others did not require an actual velocity boundary.

The full-thickness (~30 km) continental crust modelled at the landward end of the profile is comprised of three sub-crustal layers based on their distinctive velocity structures (Figs. 9a and 11a). The upper crust (C1) has the highest gradient (0.04 s^{-1}), the lowest velocities (5.6–6.3 km s^{-1}) and the largest thickness (16 km); the middle crust (C2) shows intermediate gradient (0.02 s^{-1}), velocity (6.4–6.6 km s^{-1}) and thickness (9 km); and the lower crust (C3) has the lowest gradient of 0.01 s^{-1}, the highest velocities (6.9–7.0 km s^{-1}) and the smallest thickness (5 km). While the crust as a whole does not thin until seaward of 22 km distance, the upper crust first thins gradually starting from the landward most end followed by abrupt thinning to ~1 km seaward at ~52 km distance (Fig. 9a). In contrast, the middle and the lower crustal layers individually thicken slightly seaward to a thickness of 13 km and 11 km, respectively, before rapidly thinning to 4 km in both cases seaward. The velocity gradient also increases farther seaward as the crustal layers become much thinner, with the largest increase modelled within the middle crust, and the velocities become lower (upper crust ~ 5.3–6.1 km s^{-1}; middle crust ~ 5.7–

6.5 km s^{-1}; lower crust ~ 6.5–6.8 km s^{-1}). Local thickening of the upper and middle crusts can be seen seaward of the hinge zone at ~50 km distance, suggesting the presence of tilted fault blocks. The seaward thickening in the lower crust beneath the shelf break is, in contrast, more regional and smooth. Toward the seaward limit of the continental zone (140–172 km), the velocity structures become slightly different from those landward: the crustal velocity gradients decrease to 0.04–0.06 s^{-1} and the velocity increases to > 7 km s^{-1} within the lower crust. As the Moho forms a concave upward geometry seaward of distance 70 km, we are able to observe numerous rays diving through the mantle (Fig. 9b) and a normal mantle velocity of 8.0 km s^{-1} is modelled.

The transitional zone (172–272 km) farther seaward clearly shows a very different set of velocity structure (Figs. 9a and 11b and c). Layer T1, the transitional zonal equivalence of layer C1, has both very low velocity (5.3–5.4 km s^{-1}) and velocity gradient (lowest ~ 0.04 s^{-1}) toward the middle of the zone but a more-or-less constant thicknesses of ~1–2 km (Fig. 9a). The middle crust (C2) pinch-outs within this zone, creating a large velocity discontinuity across the boundary between layers T1 and T2 (the transitional zonal equivalence of layer C3; velocities ~6.3–7.5 km s^{-1}). Layer T2 also thins seaward from a thickness of 4.7 km until pinching out at ~260 km distance while its velocity gradient increases to a maximum of 0.6 s^{-1} at distance 236 km, which is abnormal for crustal layers (Figs. 9a and 11a, b and c). Underneath layer T2, a new layer is modelled as T3 for velocity structures that are very different from those of other layers. Its velocities of 7.1–8.0 km s^{-1} are approximately between those of the layer C3/T2 landward and normal mantle underneath. Therefore, velocity discontinuity across layers T2 and T3 is small (~0.5 km s^{-1}) at the landward and seaward ends (Fig. 11c), and no velocity discontinuity into the normal mantle layer underneath at distance 221 km is modeled (Fig. 11b). Layer T3 also has a relatively high velocity gradient of 0.16–0.42 s^{-1} (Figs. 9a, 11b and c) and a general seaward increase in thickness to a maximum of 4.3 km at distance 240 km (Figs. 9a and 11c) before it rapidly thins and pinches out seaward into the Oceanic zone.

The other major lateral change in velocity structures is modeled seaward, from the transitional to the oceanic zone (Fig. 9a). The basement in the oceanic domain is elevated to ~9–10 km deepth and is characterized by rough topographic highs. Layer L2, which is modeled as an extension of C1/T1 that we interpret as oceanic layer 2, is highly variable in velocity (5.0–5.9 km s^{-1}), velocity gradient (0.1–0.5 s^{-1}) as well as thickness (0.4–1.9 km s^{-1}) across this zone. The mid-crustal boundary at the base of oceanic layer 2 is equally rough and marks a high velocity discontinuity into oceanic layer 3 (L3) with modeled velocities of 6.2–7.4 km s^{-1} (Figs. 9a and 11d). The modelled velocity gradient is consistently high (~0.25 s^{-1}) across the L2 and L3. Despite the large variations in both the top and the bottom boundary depths, the thickness of the layer 3 remains relatively consistent at ~3.7 km, except at the seaward end (> 390 km distance) where it is thinner, though the modeling constraints are poor at the model edges. A normal mantle velocity of 8.0 km s^{-1} is modelled beneath layer 3, constrained by a large number of rays (Fig. 9b).

4.3. Error analysis and Resolution for Velocity Model

We performed statistical error analysis (Table 2) of our final velocity model (Fig. 9a) by calculating the root-mean-square (rms) residual t_{rms} (0.099 s overall) and normalized χ^2 (2.177 overall), with respect to their pick uncertainties (10–150 ms). When χ^2 is ~1, observed data are neither over-fitted nor under-fitted by the model, which is considered optimal. However, complexities in modelled structures such as large tilted fault blocks, salt diapirs and LVL across rifted margins as in our case (e.g. Lau *et al.* 2006; Funck *et al.* 2004) commonly cause a large decrease in the number of constraining picks making χ^2 of ~1 impractical.

According to Table 2, half of the 24 inverted phases have a $\chi^2 \leq 1.5$ and three quarters have a $\chi^2 \sim\leq 2$. For the remaining quarter of phases, two of which are sedimentary (P_{s1}, P_{s6}), three crustal ($P_{c2}P$, P_{c3}, P_mP) and one mantle (P_{n2}), χ^2 is > 2.5. The larger value for P_{s1} (2.861) is a combination of an oversimplification of complex seafloor velocity structures and small pick uncertainties (mean = ±0.018 ms) due to high signal-to-noise ratio of the arrivals. For P_{s6}, its χ^2 value of 2.714 is likely due to the blending of the steeply dipping salt structures in layer S6 and the surrounding sediment into a single layer (Fig. 9a). Wide-angle crustal reflections also tend to have worse fits than those of the sediment due to multi-path diffractions caused by rough layer interface geometry such as those of $P_{c2}P$ and P_mP (Fig. 3) within the continental zone and larger uncertainties in their interpretations not included in the error analysis. Furthermore, the large χ^2 of P_{c3} and P_{n2} stems from the detailed fitting of a deep layer across a large number of OBSs that sampled the same region as misfits are compounded from shallower layers and their large traveltimes also mean that only a small percentage in error will translate into a large χ^2.

The resolution for different parts of the model is represented by the diagonal values of the resolution matrix (Zelt & Smith 1992) for each velocity (Fig. 12a) and depth node (Fig. 12b). The resolution matrix values can range from 0 to 1 and are controlled by the number of picks and their distribution in relation to the structures. Regions with resolution >0.5 are of relatively better resolution and vice versa. Regarding the velocity resolution, starting from the sedimentary layers, most parts of the top most sedimentary layers (S1–3) are very highly resolved (> 0.7; Fig. 12a). The deeper sedimentary layers (S5–8) have relatively good resolution beneath the slope and seaward. The thickest parts of the sedimentary layers S6 and S7 where salt structures are present (125–140 km and 160–190 km, respectively) are among the best resolved. For the continental crust, all three crustal layers are relatively well resolved beneath the shelf away from the landward end of the model and layers C1 (upper crust) and C3 (lower crust) remain well resolved underneath the continental rise. The transitional layer T1 and T3 shows fairly high resolution at distance 240–265 km. The oceanic layer 3 (O2) is also relatively well resolved landward of 350 km distance. With resolution >0.9 over two major regions that are sampled by a large number of rays, the normal mantle layer is the best resolved layer of the model (Figs. 9b and 12a). Resolution at the two ends of the model and at pinch-outs of layers is often poor due to the lack of constraining rays. Other locations of moderately poor resolution (<0.3) include layers S4–7 for distances 50–100 km (but they are also constrained by boreholes; Fig. 10) and layers L2 and T2 where velocity gradients are high within relatively thin layers. Another reason for low resolution is the large gap in instrument spacing between OBSs 41 and 46 and between OBSs 89 and 90. Finally, the shadow zone created by the LVL within layer S8 under the shelf also resulted in poor resolution within the basin (distance 70–105 km).

The resolution of the depth nodes (Fig. 12b) is predominantly very high (>0.7) as most of the boundaries are sampled by reflected phases (black lines in Fig. 12a). Low resolution is only present at a few locations where no reflections from the boundaries can be observed (white lines in Fig. 12a). Note that unreflective model boundaries, such as the base of layer T3, are created only for the purpose of changing the vertical velocity gradients within what would otherwise be a single continuous velocity layer.

4.4. Gravity Modelling

By using the velocity-to-density conversion curve shown in Lau *et al.* (2006) and the methodology of Talwani *et al.* (1959) and Won & Bevis (1987), we construct a 2-D gravity model that corresponds to the velocity structures in our final velocity model. This gravity model is then compared with the observed gravity (Fig. 13a and b; rms misfit = 4.0 mGal; Sandwell *et al.* 2014). The density model extends with uniform thickness to infinity at both the landward and seaward ends, and the bottom of the model is at 40 km depth as shown in Fig. 13b. For clarity, and because detailed structures are unlikely to be resolvable by gravity modeling, we combine the thin sedimentary velocity layers into two density layers. Since velocities decrease seaward, we also divide each of the two combined sedimentary layers laterally into two density blocks using a vertical boundary at the location of the greatest change in velocity. In order to improve the fit with the observed gravity, the landward part of layer S8 (distance -20–25 km), where the velocities are >5.2 km s^{-1}, requires a separate density model block so that a higher density can be assigned (2.56 Mg m^{-3}). The crustal and mantle layers are taken directly from the velocity model except for the seaward end of the oceanic layer 3 (distance 390–420 km) where a thicker layer is required to fit the observed gravity compared with the seaward thinning layer in the velocity model. Such modification is acceptable as the seismic constraints at this part of the model are poor (Figs. 9b and 12). We also separate the transitional upper crust (T1) from that of the continental zone (C1) along the 5.5 km s^{-1} contour to reflect the seaward decrease in both velocity and density (Fig. 13b).

Considering that we use uniform density distribution within each block, we estimate an average velocity for each block before converting it into density. Since the upper and lower continental crust (C1 and 2) have overlapping velocity ranges, we estimate a combined average velocity of 6 km s^{-1} and hence a density of 2.72 Mg m^{-3}. Small adjustments are, however, needed for the two mantle layers from the converted densities in order to fit the observed gravity. First, for the serpentinized mantle layer (T3, discussed below), the seismic (7.75 km s^{-1}) converted density of 3.24 Mg m^{-3} has to be lowered to 3.20 Mg m^{-3} to explain the lack of gravity high observed (Fig. 13a). Similar adjustment was also required in Lau *et al.* (2006) for the serpentinized mantle layer, suggesting that the velocity-density curve used may not be sufficiently accurate for this rock type, at least in the study area. Second, we originally used a uniform normal mantle density of 3.33 Mg m^{-3} which resulted in a good fit above the continental zone but produced a large scale misfit over the transitional and the oceanic zone. Therefore, we separated the normal mantle layer into the denser continental mantle and the less dense oceanic mantle (3.283 Mg m^{-3}; Fig. 13b) as in Funck *et al.* (2004) and Wu *et al.* (2006). Note that the abrupt boundary at ~210 km distance is arbitrary and likely represents a diffuse transition. Note also that the density contrast across this boundary depends on the bottom depth of the model. However, our contrast of 0.027 Mg m^{-3} is larger than those of similar mantle models in Funck *et al.* (2004) and Wu *et al.* (2006) despite having the same continental mantle density and model bottom depth. While the observations of a lower oceanic mantle density is not uncommon (e.g. Maystrenko & Scheck-Wenderoth 2009), the causes are yet to be understood (see Discussion section). We also calculated the pressure based on the density model at the bottom of the model (Fig. 13c). It shows that the margin is isostatically balanced at both ends while imbalance above and around the shelf break is supported by flexure.

5. Discussion

For joint interpretation of the wide-angle OBS velocity model and the coincident GXT-2000 MCS reflection image, we first convert the GXT-2000 pre-stack depth migrated section (ref?) to TWTT using the corresponding migration velocity. The resulted time section is then converted back to depth by vertical stretching using the final wide-angle OBS velocity model produced in this work (Figs. 9a and 14). The velocity model and the reflection image are displayed superimposed in Figure 14 and shows good agreement, which allow for a unified interpretation. The good correspondence between the two results is not surprising considering that the MCS reflection image was an important constraint in the construction of the velocity model boundaries. Hence, a combined analysis using the depth-converted MCS section (Fig. 14), the final velocity model (Figs. 9a and 14) and the downhole seismic and stratigraphic interpretations of wells P-52 and D-76 (Fig. 10) forms the basis of the presented depositional, structural and zonal interpretation (Fig. 9a). This is followed by a comparative analysis with relevant nearby profiles across the Nova Scotia and its conjugate Morocco margins.

5.1. Rifted Continental Zone

5.2. Transitional Zone

5.3. Oceanic Zone

5.3.1. Sediment

Stratigraphic interpretation of post-rift sedimentary layers along the depth profile GXT-2000 is relatively straightforward as horizon depths are calibrated by boreholes on the shelf (Figs. 10 and 14). This imaging confidence combined with a shallow water depth (< 100 m) makes the Scotian Basin underneath the shelf a potentially desirable hydrocarbon target. According to both the reflectivity and the velocity model, both the thinner (~0.5 km) layer S4 and the thicker (<2 km) layer S7 carbonate banks, which are potential reservoirs, are limited to the shelf where shallow water depths were maintained since the continental breakup due to proximity to sediment sources (Fig. 14a). Note that the actual top of the late Jurassic carbonate bank may be at the Mic Mac top boundary within layer S6. The layer S7 carbonate bank reaches such high velocities (5.8 km s^{-1}) that any clastic sediment underneath creates a LVL (see Section 3 and

Funck *et al.,* 2004). With only three OBSs (# 15—17) directly above the carbonate bank, Funck *et al.* (2004) was unable to resolve its thickness, hence extended it down to the basement for simplicity. However, we are able to constrain with high depth resolution (Fig. 12d) the thickness of this layer using constrains from at least 7 OBSs directly above the carbonate bank and the observed reflections from the MCS image (Fig. 14a).

A larger number of OBSs do not, however, solve the problem of the lack of turning rays through the LVL so its velocities remain poorly constrained. Boreholes also do not penetrate deep enough to constrain velocities in this layer (Fig. 10). While Funck *et al.* (2004) presented a model without a LVL (except for the salt), we propose one with interpolated sedimentary velocities beneath the high velocity layer (HVL) as descripted in Section 3. Note that such uncertainty also translates into uncertainties in the depths of basement and deeper boundaries such as Moho. Another major difference between the two models is the absence of salt diapirs beneath the shelf in the OETR-2009 model. Instead, basement highs are interpreted, according to their velocities, as large scaled (~15 km wide and ~5 km high) tilted basement blocks. This also agrees with observed tilted sediments within the basin that mostly dip landward as in syn-rift sediment (Fig 14a). The Scotian Basin, is hence, interpreted as a series of smaller half-grabens rather than a large slope basin as suggested in the SMART-1 model. The basement model of OETR-2009 also fits the observed gravity (Fig.13a) much better than that of SMART-1. Implications to source rock and hydrocarbon formation are, however, beyond the scope of this paper. Salt structures are, however, widespread beneath the slope and the abyssal plain (Fig. 4b).

5.4. Regional Comparison

5.4.1. Nova Scotia Margin

...

5.4.2. Moroccan Margin

6. Conclusions

We

7. Acknowledgement

We.

8. References

Biari, Y. *et al.*, 2015. Deep crustal structure of the North-West African margin from combined wide-angle and reflection seismic data (MIRROR seismic survey), *Tectonophysics*, **656**, 154–174, doi:10.1016/j.tecto.2015.06.019.

Funck, T., Jackson, H.R., Louden, K.E., Dehler, S.A. & Wu, Y., 2004. Crustal structure of the northern Nova Scotia rifted continental margin (eastern Canada), *Journal of Geophysical Research: Solid Earth*, **109**(B9), doi:10.1029/2004JB003008.

GEBCO, 2008. General Bathymetric Chart of the Oceans (GEBCO) One Minute Grid, *British Oceanographic Data Centre*. Available from: https://www.bodc.ac.uk/data/hosted_data_systems/gebco_gridded_bathymetry_data/gebco_one_minute_grid/

Lau, K.W.H., Louden, K.E., Funck, T., Tucholke, B.E., Holbrook, W.S., Hopper, J.R. & Christian Larsen, H., 2006. Crustal structure across the Grand Banks–Newfoundland Basin Continental Margin – I. Results from a seismic refraction profile, *Geophysical Journal International*, **167**(1), 127–156, doi:10.1111/j.1365-246X.2006.02988.x.

Maystrenko, Y. & Scheck-Wenderoth, M., 2009. Density contrasts in the upper mantle and lower crust across the continent-ocean transition: constraints from 3-D gravity modelling at the Norwegian margin, *Geophysical Journal International*, **179**(1), 536–548, doi:10.1111/j.1365-246X.2009.04273.x.

Sandwell, D.T., Müller, R.D., Smith, W.H.F., Garcia, E. & Francis, R., 2014. New global marine gravity model from CryoSat-2 and Jason-1 reveals buried tectonic structure, *Science*, **346**(6205), 65–67, doi:10.1126/science.1258213.

Shimeld, J., 2004. A comparison of salt tectonic subprovinces beneath the Scotian Slope and Laurentian Fan, in *GCSSEPM 24th Annual Bob F. Perkins Research Conference, Salt Sediment Interactions and Hydrocarbon Prospectivity: Concepts, Applications, and Case*

Studies for the 21st Century, Vol. 24, pp. 291–306, eds Post, P., Olson, D., Lyons, K., Palmes, S., Harrison, P. & Rosen, N., Gulf Coast Section, SEPM Foundation, Houston, TX.

Talwani, M., Worzel, J.L. & Landisman, M., 1959. Rapid gravity computations for two-dimensional bodies with application to the Mendocino submarine fracture zone, *Journal of Geophysical Research*, **64**(1), 49–59, doi:10.1029/JZ064i001p00049.

Won, I.J. & Bevis, M., 1987. Computing the gravitational and magnetic anomalies due to a polygon; algorithms and Fortran subroutines, *Geophysics*, **52**(2), 232–238, doi:10.1190/1.1442298.

Wu, Y., Louden, K.E., Funck, T., Jackson, H.R. & Dehler, S.A., 2006. Crustal structure of the central Nova Scotia margin off Eastern Canada, *Geophysical Journal International*, **166**(2), 878–906, doi:10.1111/j.1365-246X.2006.02991.x.

Zelt, C.A. & Smith, R.B., 1992. Seismic traveltime inversion for 2–D crustal velocity structure, *Geophysical Journal International*, **108**, 16–34.

9. Figure Captions

Figure 1. Bathymetry map (colour scale) showing locations of the OETR-2009 OBS profile (this paper; red line), coincident MCS profile GXT-2000 (black line), wide-angle seismic profiles SMART (Funck *et al.* 2004; Wu *et al.* 2006), connecting MCS profile GXT-5100 and selected boreholes (brown). The OETR-2009 profile was collected along a great circle and GXT-2000 profile was not, resulting in minor location differences. The study area (red rectangle) is shown relative to eastern Canada and US in the inset. The bathymetry is contoured (thin dashed lines) every 1000 m. Yellow patches are salt (Shimeld 2004). The OETR-2009 model distance is tick-marked and labelled in black. Red filled circles are locations of OBSs. Area around profile OETR-2009 is enlarged in the lower panel with OBSs numbered in red (white on dark background) and bathymetry contoured every 500 m. SI – Sable Island.

Figure 2. Velocity modelling of shallow sediments for OBS 12. Top: hydrophone data overlaid by theoretical traveltimes (colour curves) versus model distances from ray tracing through the

final velocity model. Dashed colour segments are only from forward modelling. Traveltime is reduced by 4 km s^{-1} relative to shot-receiver offsets. The data have been processed with minimum-phase predictive deconvolution and bandpass filtering. Inset shows the linear moveout of different phase velocities in km/s. Middle: the corresponding ray-path diagram. Black lines are model boundaries and grey areas are crustal layers. See Legend (Bottom) for colour coding and Table 1 for nomenclature of the observed wave phases.

Figure 3. Velocity modelling of deeper sediments for OBS 12. Top: hydrophone data overlaid by theoretical traveltimes versus model distances from ray tracing through the final velocity model. Traveltime is reduced by 6 km s^{-1} relative to shot-receiver offsets. Black arrows show the beginning of a step back in arrival traveltimes. Bottom: the corresponding ray-path diagram. Ray colour legend is shown in Figure 2. Other information same as in Figure 2 caption.

Figure 4. Velocity modelling for OBS 27. Top: vertical geophone data overlaid by theoretical traveltimes versus model distances from ray tracing through the final velocity model. Traveltime is reduced by 6 km s^{-1} relative to shot-receiver offsets. Bottom: the corresponding ray-path diagram. Ray colour legend is shown in Figure 2. Other information same as in Figure 2 caption.

Figure 5. Velocity modelling for OBS 3. Top: hydrophone data overlaid by theoretical traveltimes versus model distances from ray tracing through the final velocity model. Traveltime is reduced by 6 km s^{-1} relative to shot-receiver offsets. Bottom: the corresponding ray-path diagram. Ray colour legend is shown in Figure 2. Other information same as in Figure 2 caption.

Figure 6. Velocity modelling for OBS 23 (left) and 24 (right). Top: vertical geophone (OBS 23) and hydrophone (OBS 24) data overlaid by theoretical traveltimes versus model distances from ray tracing through the final velocity model. Traveltime is reduced by 6 km s^{-1} relative to shot-receiver offsets. Bottom: the corresponding ray-path diagram. Ray colour legend is shown in Figure 2. Other information same as in Figure 2 caption.

Figure 7. Velocity modelling for OBS 54. Top: vertical geophone data overlaid by theoretical traveltimes versus model distances from ray tracing through the final velocity model. Traveltime is reduced by 6 km s^{-1} relative to shot-receiver offsets. Bottom: the corresponding ray-path diagram. Ray colour legend is shown in Figure 2. Other information same as in Figure 2 caption.

Figure 8. Velocity modelling for OBS 79. Top: hydrophone data overlaid by theoretical traveltimes versus model distances from ray tracing through the final velocity model. Traveltime is reduced by 6 km s^{-1} relative to shot-receiver offsets. Bottom: the corresponding ray-path diagram. Ray colour legend is shown in Figure 2. Other information same as in Figure 2 caption.

Figure 9. Final P-wave velocity model of profile OETR-2009 (a) and constraining ray diagram (b). (a) Stars are OBS locations with filled colours representing differing constraints input to the model: red, fully picked; grey, not picked; unfilled, no data. The velocity model has layer boundaries in black lines and velocities defined by colour scale. Dashed-line segment of Moho boundary at the right hand model end is different from that of the density model in Fig. 13. Layers are labelled according to Fig. 2 legend and Table 1 except C1—3 are replaced with T1—2 and L2—3 for the transitional and the oceanic zone, respectively. White rectangles at the bottom show crustal zonal interpretations (see text). Velocities are contoured every 0.1 km s^{-1} (white lines). OBS numbers are above black arrows; vertical blue lines are well positions projected along profile. Vertical pink lines locate the 1-D velocity–depth profiles plotted in Fig. 11. Area outside of ray coverage is masked. (b) Illumination diagram showing ray density in colour (truncated at 1000 rays). Only rays used for inversion are shown. Grey lines are model boundaries.

Figure 10. 1-D velocity versus depth profiles through the sedimentary layers of the final model at 60 and 75 km model distance (solid lines), projected locations of wells P-52 and D-76, respectively, and their corresponding downhole seismic models (dashed line). Layers are labeled

for model 60 km according to Fig. 9a. Ages and depths of stratigraphic formations and location of the O-marker (red line) are taken from previous interpretations of well P-52 (ref?).

Figure 11. 1-D velocity versus depth profiles extracted at selected locations over the three interpreted crustal zones for models OETR-2000 (red), SMART-1 (black) and SMART-2 (blue). See Figs. 9a and 15 for profile locations on their corresponding 2D models. Depths are shown relative to top of crystalline basement. Layers are only labelled for the OETR profiles.

Figure 12. Model resolution plots. (a) Colour scale shows gridded diagonal values of the resolution matrix for all velocity nodes. Red means better resolved and blue means less well resolved. Note that values for areas between layer boundaries are linearly interpolated from values along the boundaries. Black lines represent locations of layer boundaries illuminated by picked reflections and white lines are locations without observations. See caption of Fig. 9a regarding model layer names, crustal zonal interpretations and OBS symbols. (b) Depth resolution of velocity model boundaries. Black lines are velocity model layer boundaries. Colour-scaled circles are diagonal values of the resolution matrix of the depth nodes.

Figure 13. (b) Density model (Mg m^{-3}) derived from the final velocity model. The Moho depths at the seaward end of the model (for distances 390–420 km) were modified for the density model to show greater continuity in oceanic crustal thickness. Dashed line shows the depth as determined by velocity modeling of the seismic arrivals. The densities of the serpentinized mantle and oceanic mantle blocks, shown in bold numbers, do not follow the velocity-density conversion used for other layers in the model. (a) Observed (Sandwell & Smith 2009) and calculated gravity anomalies from the 2-D density model (Fig. 13b). (c) Lithostatic pressure at 40 km depth, which is the bottom of the model in b.

Figure 14. MCS profile GXT-2000 (foreground reflectivity) after conversion to depths using the OETR-2009 final velocity model (colour background). Dashed lines are model boundaries;

stars are OBS positions. See Fig. 9 for explanation to labelling of layers and OBS fill colours. The original continuous profile is divided into three detailed subplots for different regions of interest: (a) moderately thinned continental crust beneath the shelf; (b) highly thinning continental beneath the slope and rise; (c) continent-ocean-transition.

Figure 15. Along-strike comparison of the continent-ocean transition (COT) across the northeastern Nova Scotia margin based on RAYINVR p-wave velocity models of profiles (a) OETR-2009 (Fig. 9a), (b) SMART-1 (Funck *et al.* 2004), and (c) SMART-2 (Wu *et al.* 2006). See Fig. 1 for locations of profiles. Vertical red, black and blue lines show locations of 1-D profiles plotted in Fig. 11 as labelled at the top. Velocities are contoured every 250 m s^{-1}.

Figure 16. Conjugate comparison of RAYINVR p-wave velocity model between profile OETR-2009 (Fig. 9a) on the Nova Scotia margin and profile MIRROR-1 on the Moroccan margin (Biari *et al.* 2015). Crustal zones are adapted from the same paper. Question mark represent interpretation subjects to discussion (see text). Velocities are contoured every 250 m s^{-1}.

10. Appendix

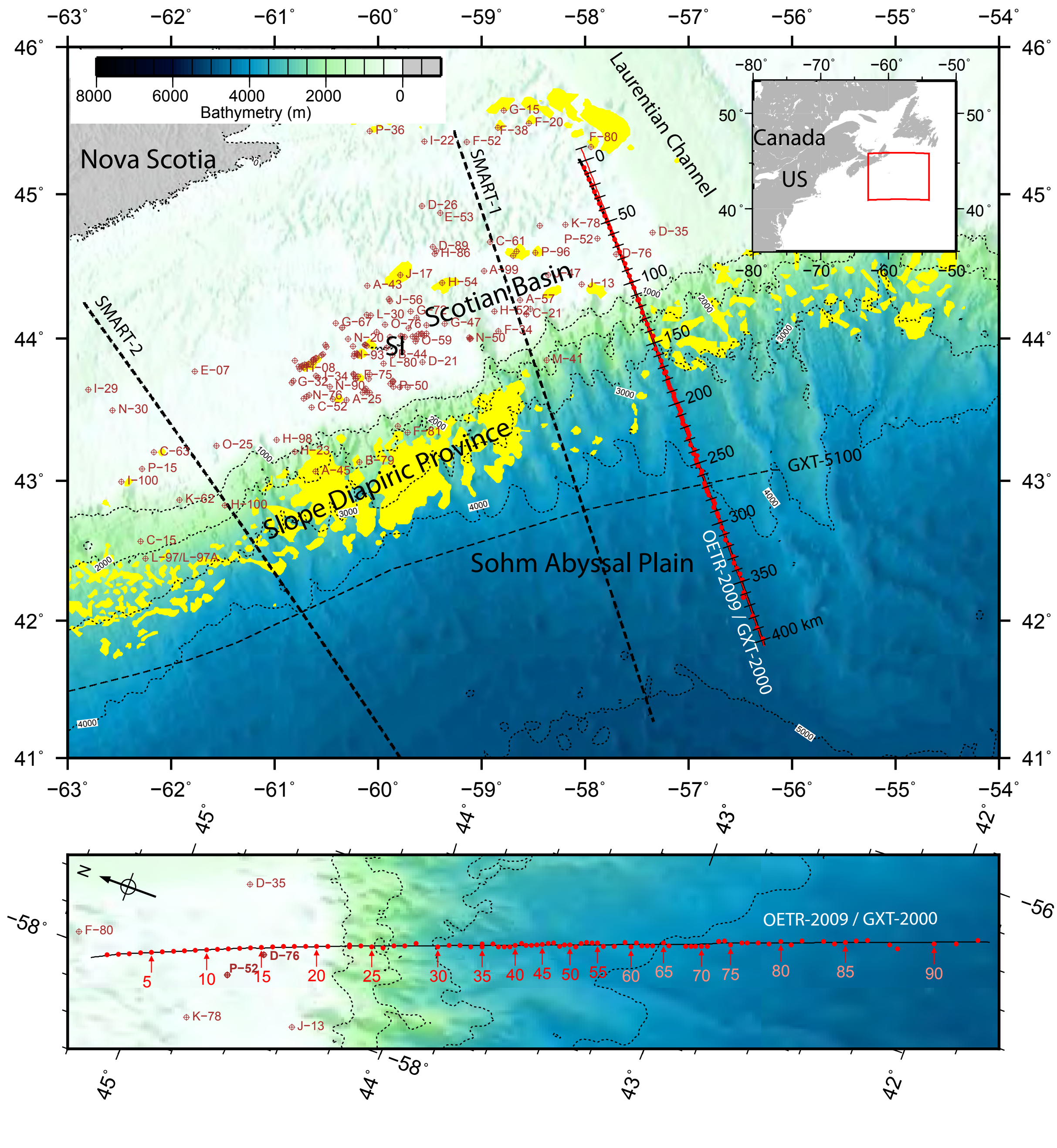

Bathymetry (m)
Nova Scotia
Laurentian Channel
Canada
US
SMART-1
SMART-2
Scotian Basin
Slope Diapiric Province
Sohm Abyssal Plain
GXT-5100
OETR-2009 / GXT-2000
400 km

Figure 1

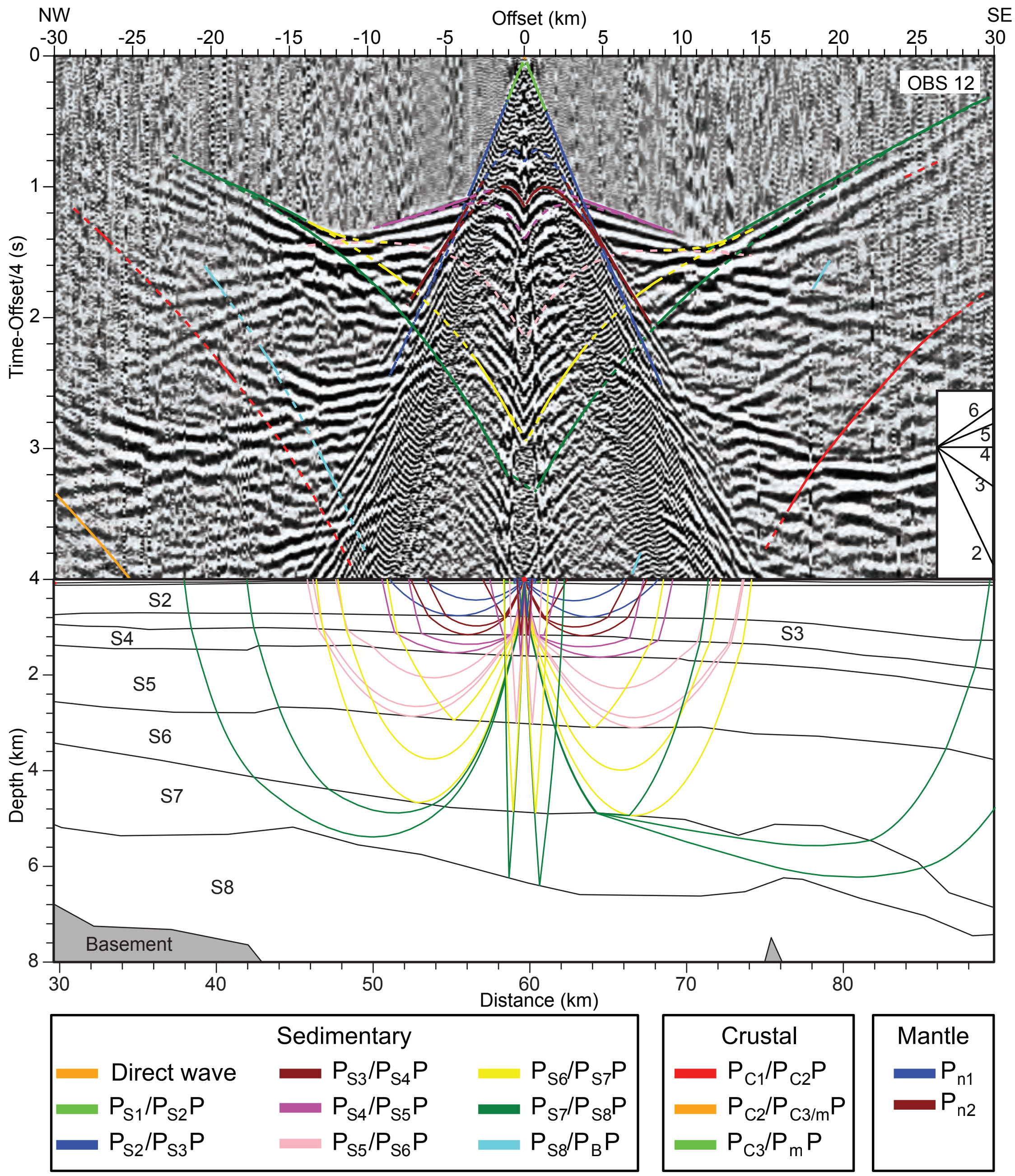

NW
Offset (km)
SE
-30
-25
-20
-15
-10
-5
0
5
10
15
20
25
30
OBS 12
Time-Offset/4 (s)
0
1
2
3
4
6
5
4
3
2
S2
S3
S4
S5
S6
S7
S8
Basement
Depth (km)
2
4
6
8
30
40
50
60
70
80
Distance (km)
Sedimentary
Direct wave
$P_{S1}/P_{S2}P$
$P_{S2}/P_{S3}P$
$P_{S3}/P_{S4}P$
$P_{S4}/P_{S5}P$
$P_{S5}/P_{S6}P$
$P_{S6}/P_{S7}P$
$P_{S7}/P_{S8}P$
$P_{S8}/P_{B}P$
Crustal
$P_{C1}/P_{C2}P$
$P_{C2}/P_{C3/m}P$
$P_{C3}/P_{m}P$
Mantle
P_{n1}
P_{n2}

Figure 2

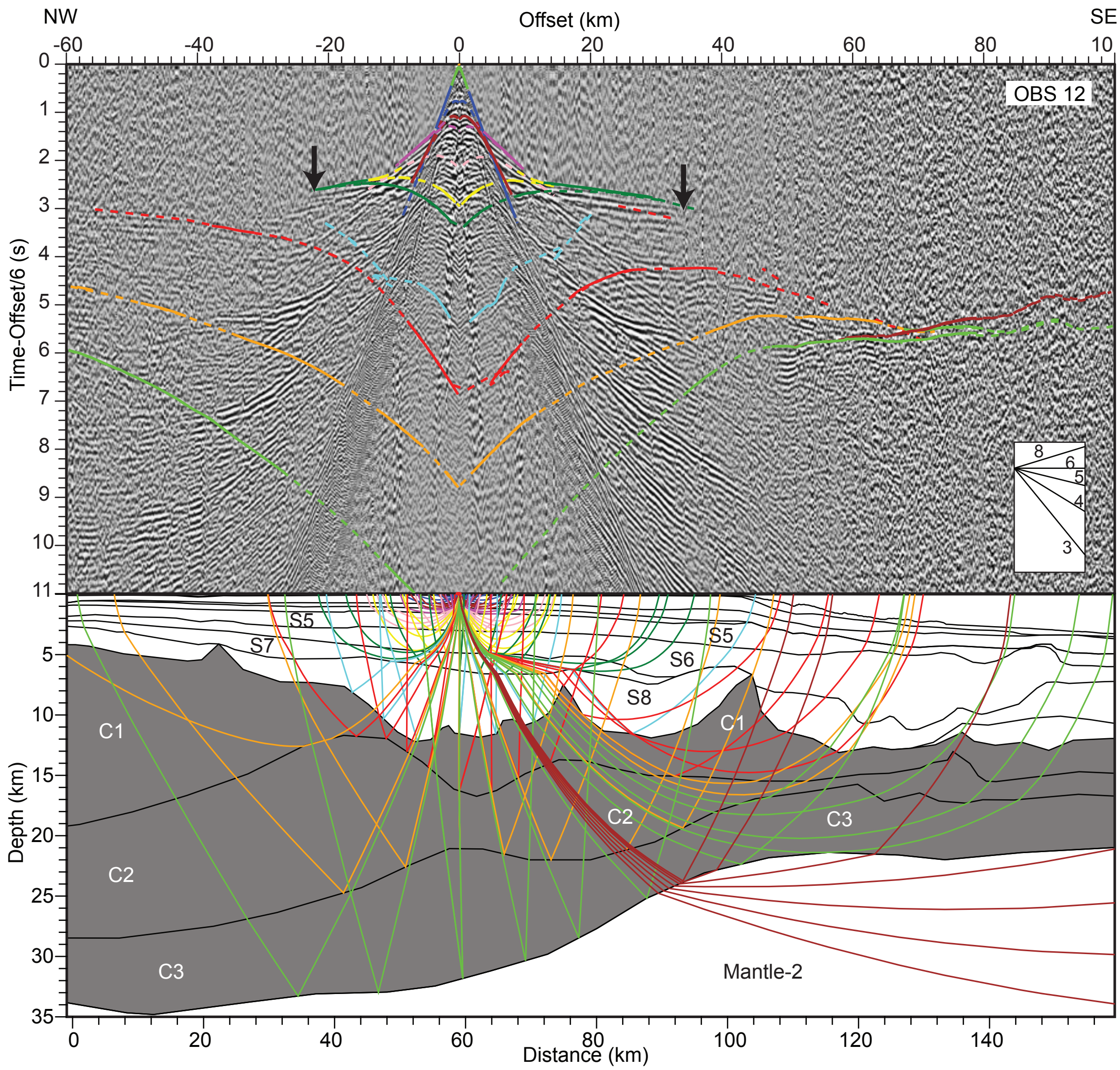

Figure 3. Decon1

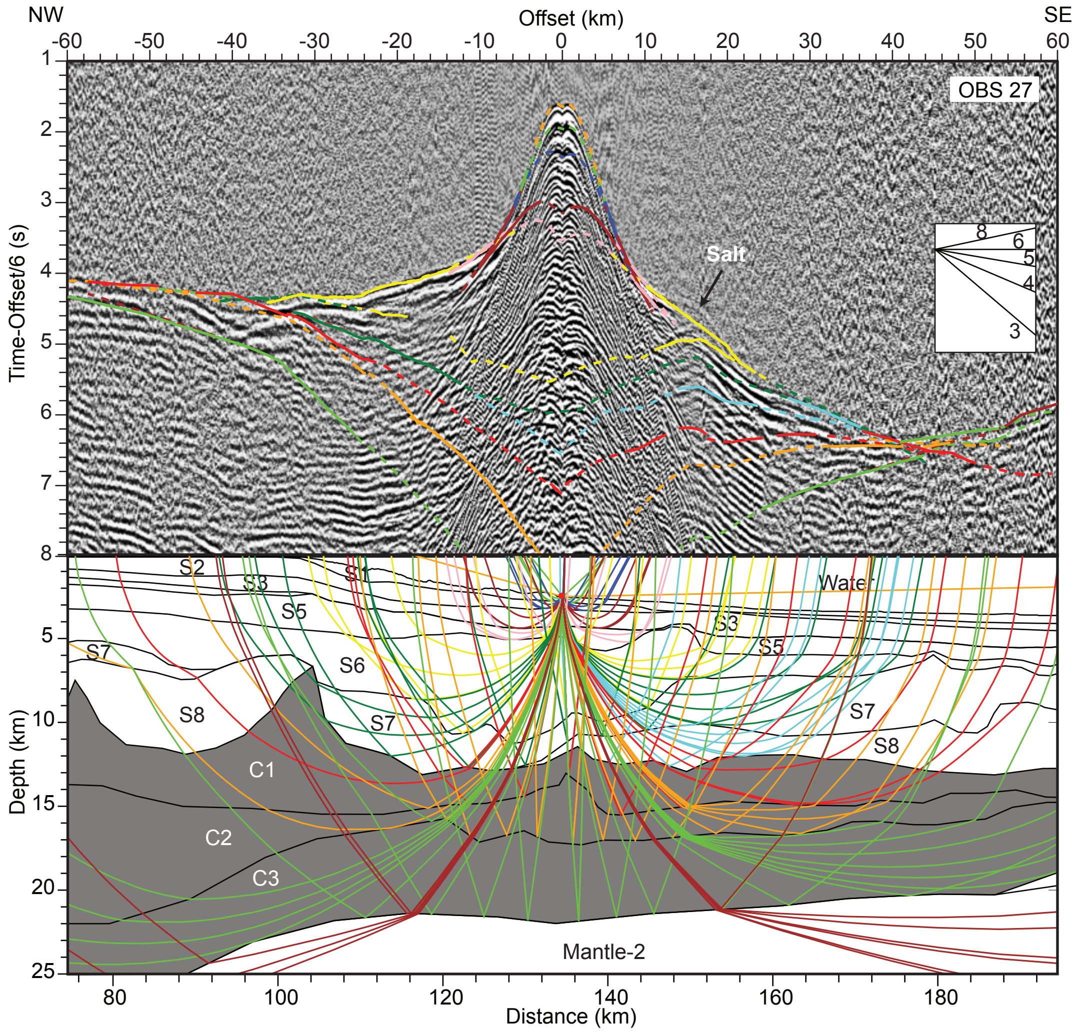

Figure 4. Decon 2.

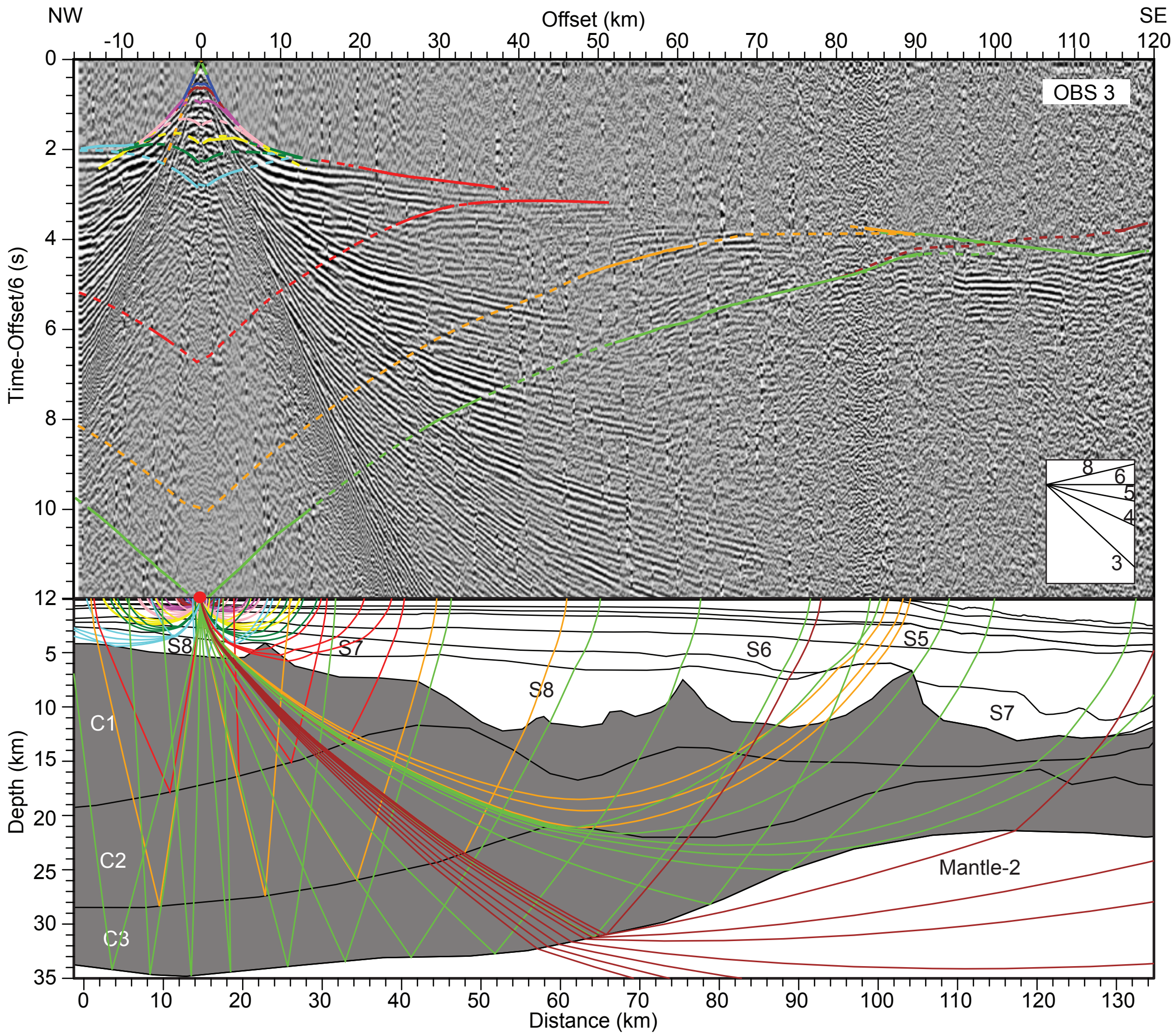

Figure 5. Decon 2.

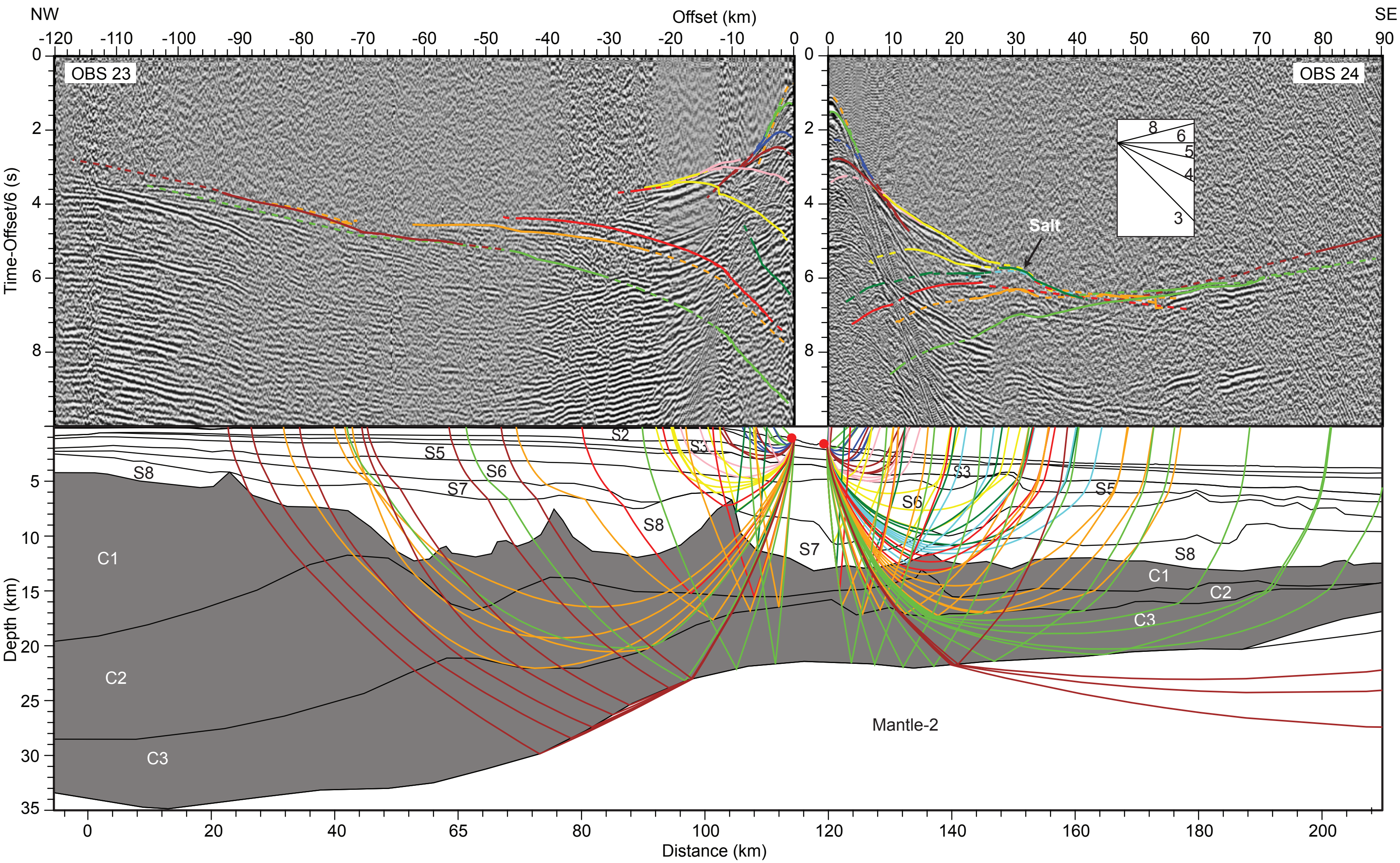

Figure 6. Decon 3.

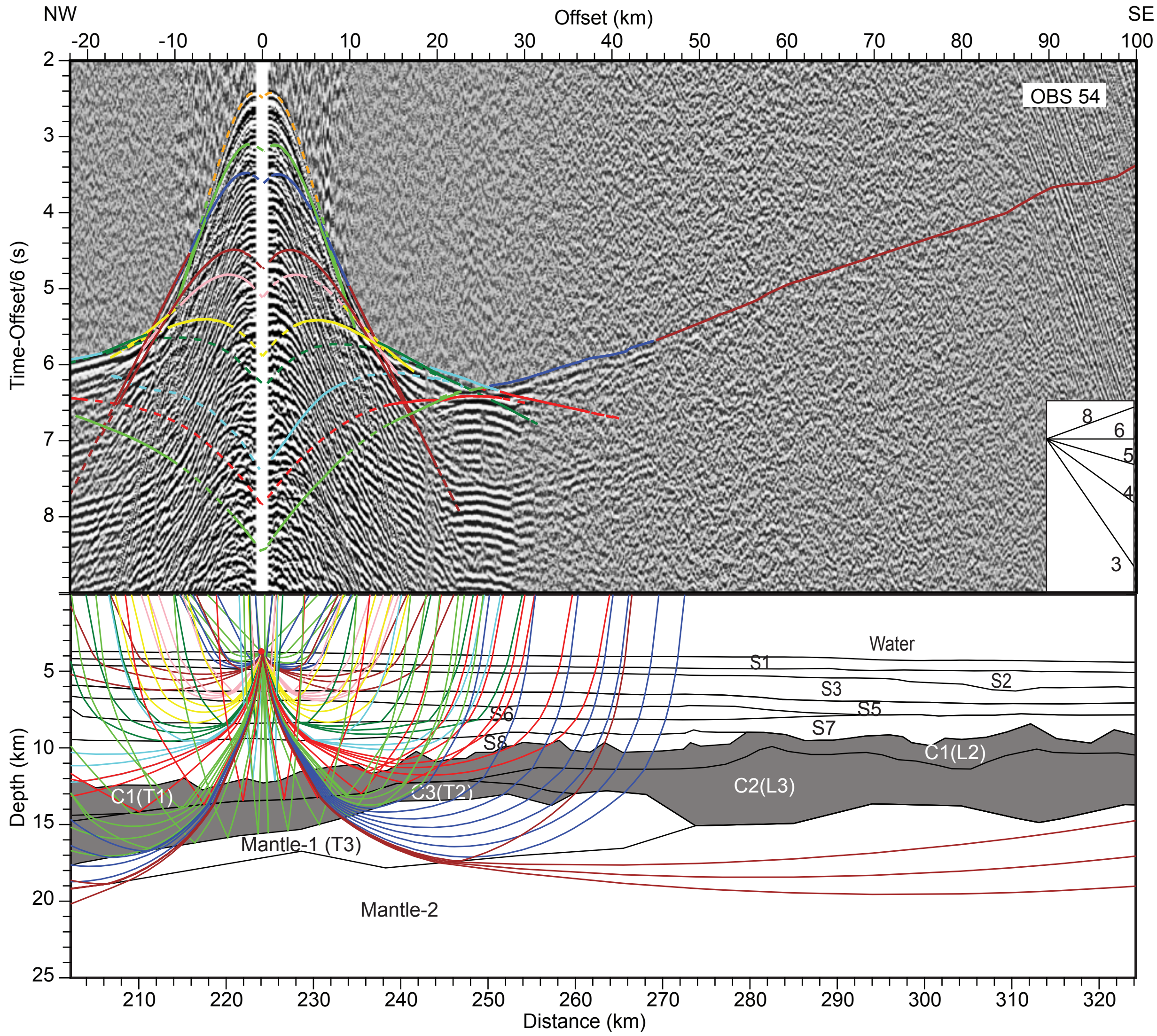

Figure 7. Decon. 3

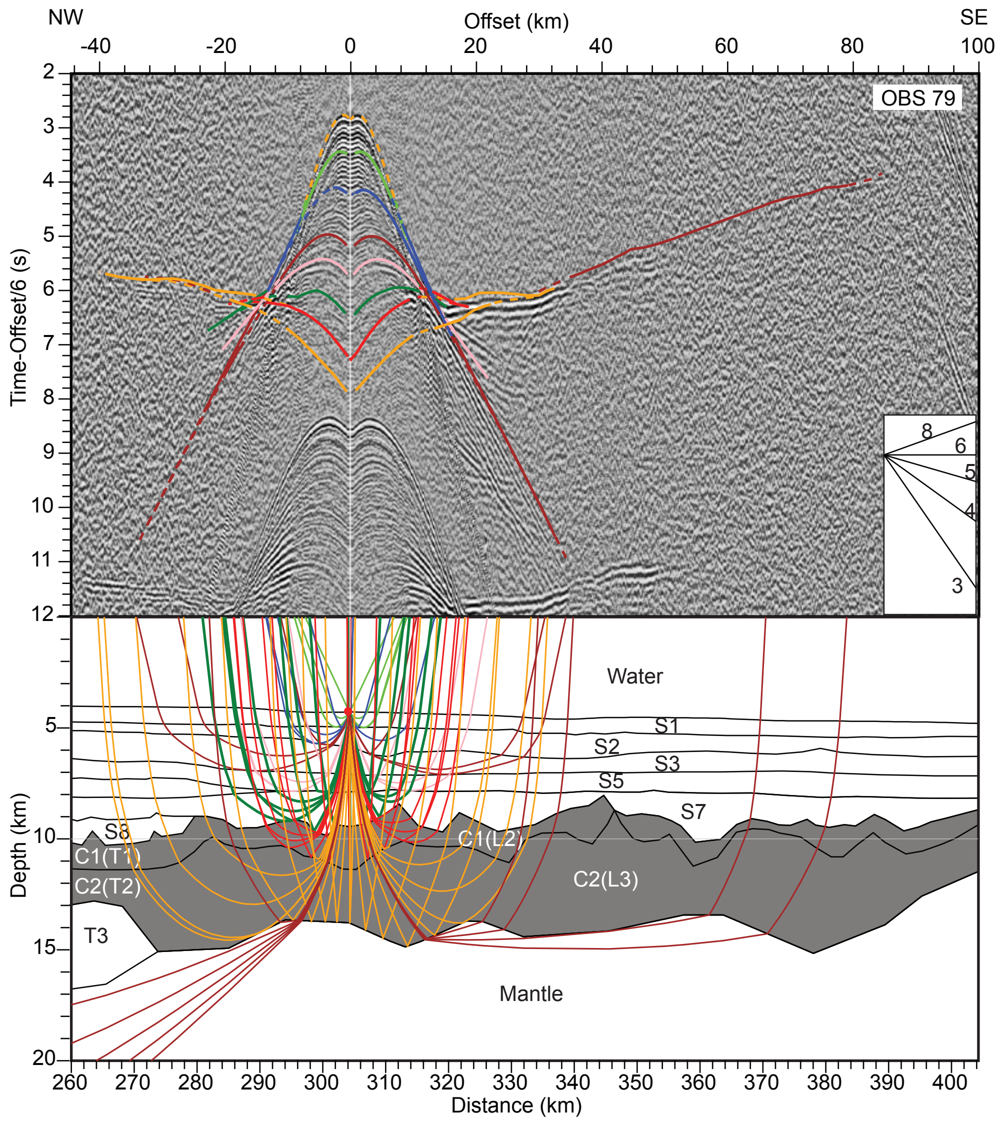

Figure 8. Decon. 3

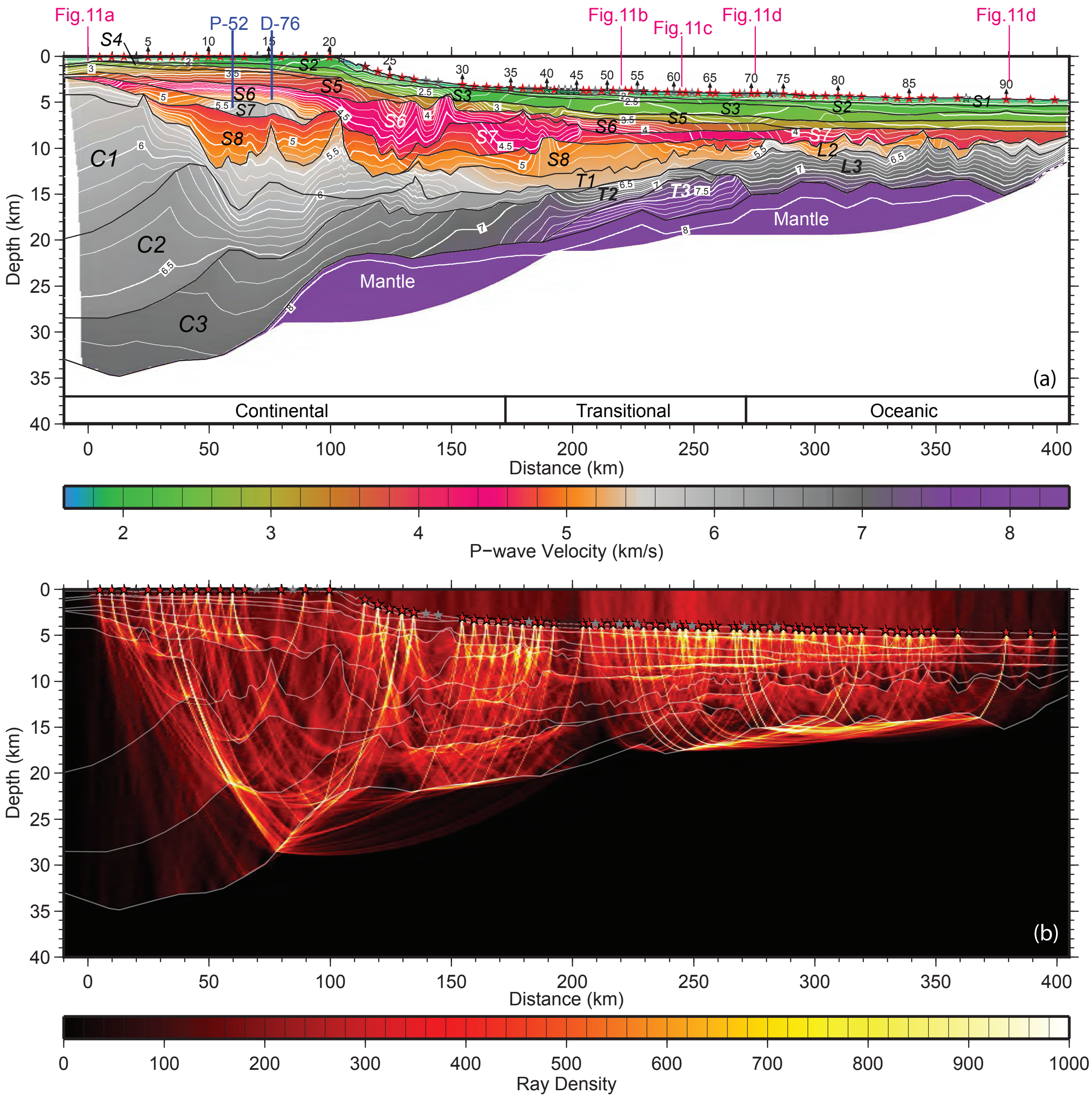

Fig.11a
P-52
D-76
Fig.11b
Fig.11c
Fig.11d
Fig.11d
S4
S2
S5
S6
S7
S8
S3
S1
L2
L3
T1
T2
T3
C1
C2
C3
Mantle
Mantle
(a)
Continental
Transitional
Oceanic
Depth (km)
Distance (km)
P−wave Velocity (km/s)
(b)
Depth (km)
Distance (km)
Ray Density

Figure 9

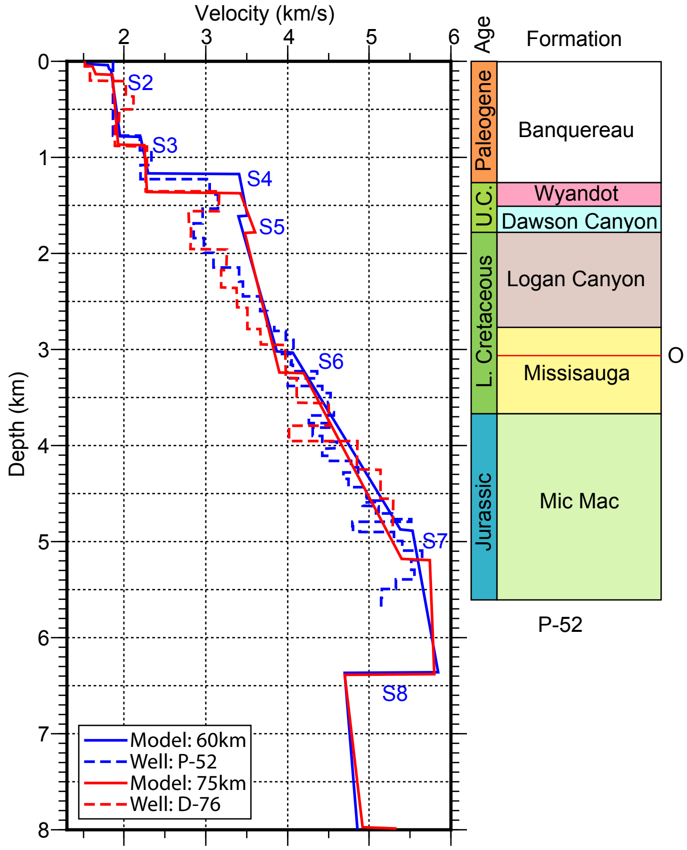

Velocity (km/s)
2
3
4
5
6
0
1
2
3
4
5
6
7
8
Depth (km)
S2
S3
S4
S5
S6
S7
S8
Model: 60km
Well: P-52
Model: 75km
Well: D-76
Age
Formation
Paleogene
U.C.
L. Cretaceous
Jurassic
Banquereau
Wyandot
Dawson Canyon
Logan Canyon
Missisauga
Mic Mac
O
P-52

Figure 10

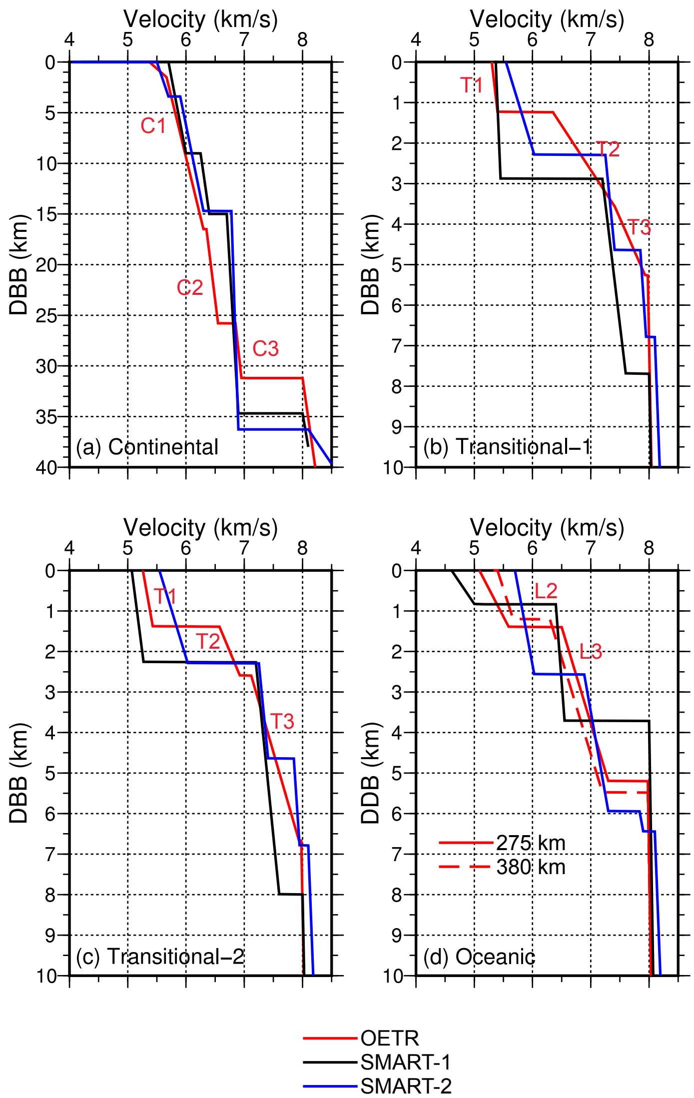

Velocity (km/s)
DBB (km)
C1
C2
C3
(a) Continental
(b) Transitional−1
T1
T2
T3
(c) Transitional−2
DDB (km)
L2
L3
275 km
380 km
(d) Oceanic
OETR
SMART-1
SMART-2

Figure 11

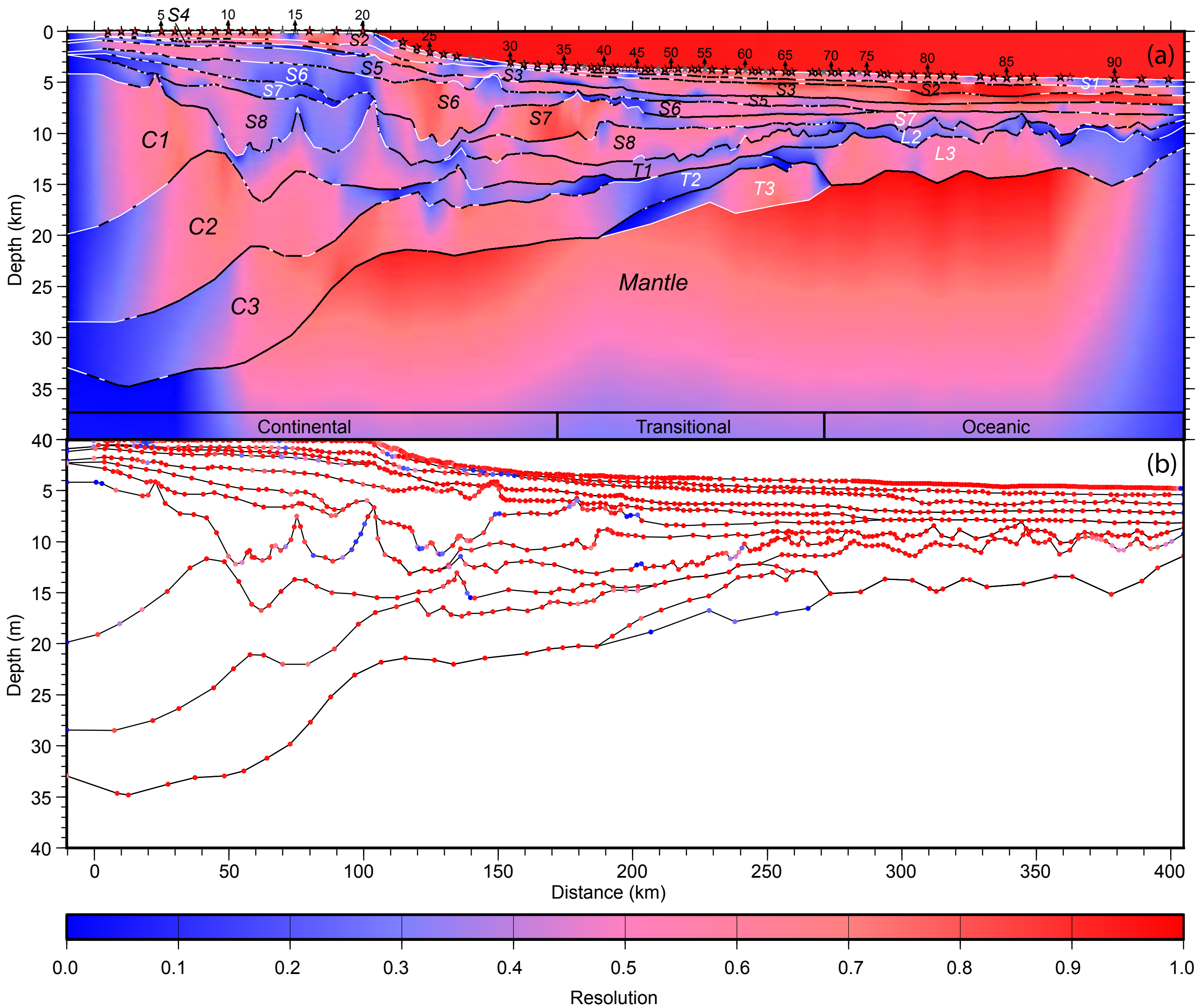
(a)
(b)
S4
S2
S5
S6
S7
S8
S3
S1
C1
C2
C3
T1
T2
T3
L2
L3
Mantle
Continental
Transitional
Oceanic
Depth (km)
Depth (m)
Distance (km)
Resolution
0.0
0.1
0.2
0.3
0.4
0.5
0.6
0.7
0.8
0.9
1.0

Figure 12

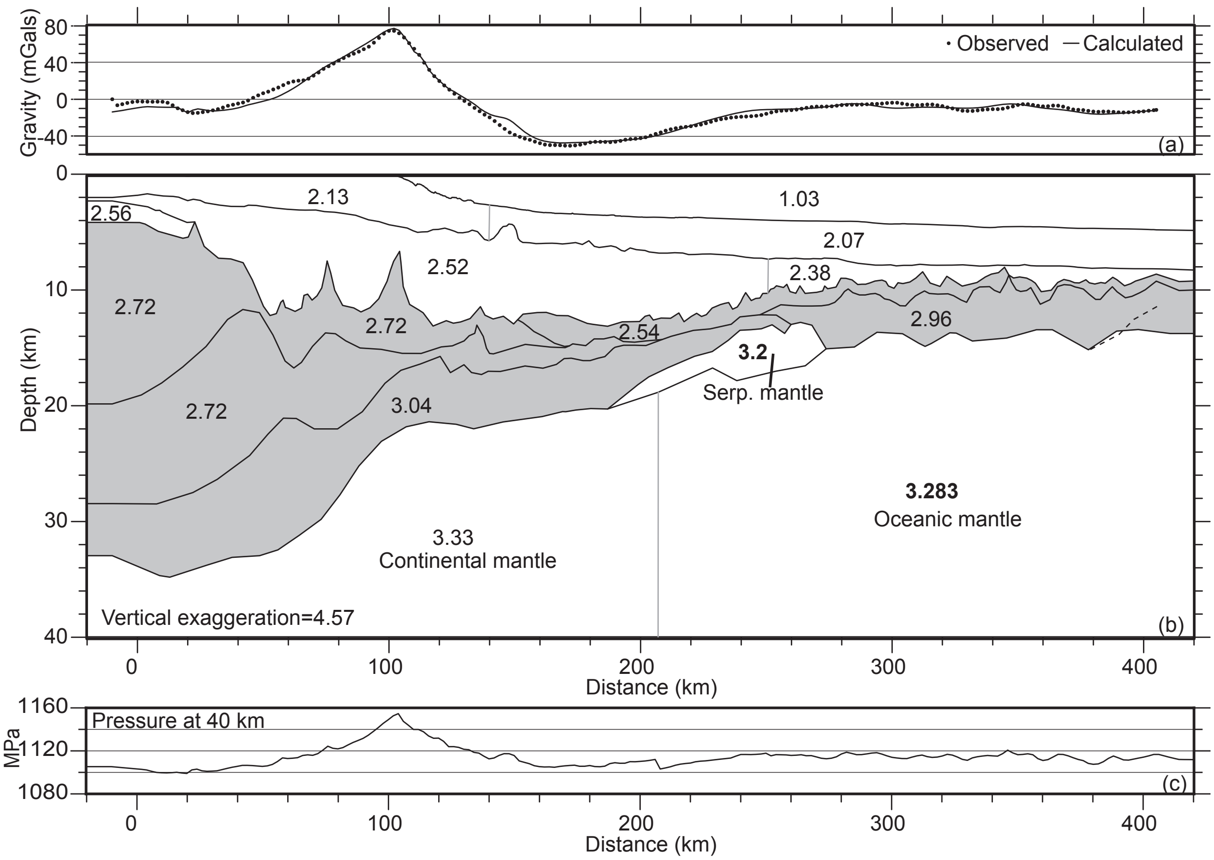
Gravity (mGals)
80
40
0
-40
• Observed — Calculated
(a)
Depth (km)
0
10
20
30
40
2.13
1.03
2.56
2.07
2.52
2.38
2.72
2.72
2.54
2.96
3.2
Serp. mantle
2.72
3.04
3.283
Oceanic mantle
3.33
Continental mantle
Vertical exaggeration=4.57
(b)
0
100
200
300
400
Distance (km)
MPa
1160
1120
1080
Pressure at 40 km
(c)
0
100
200
300
400
Distance (km)

Figure 13

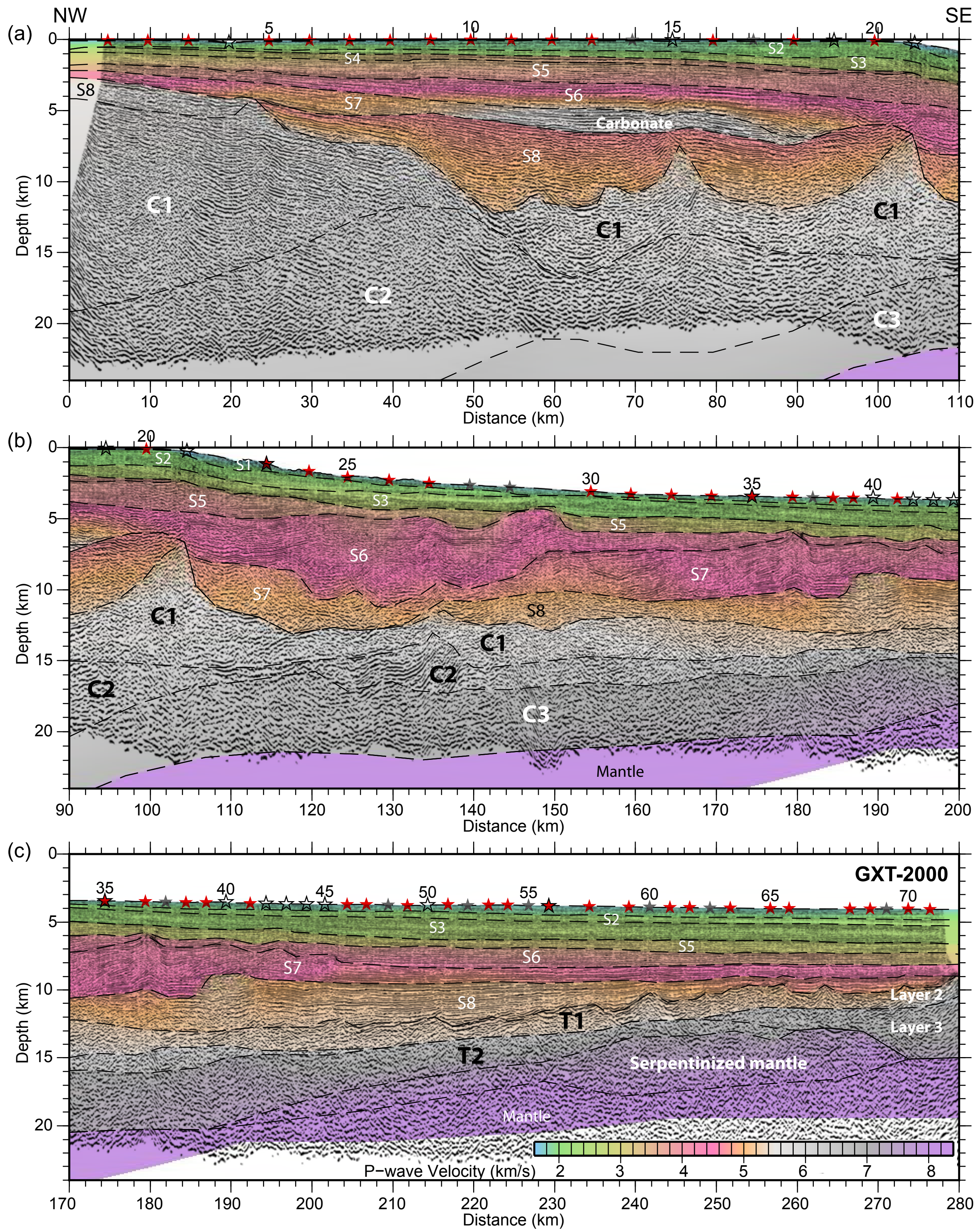

NW
SE
(a)
(b)
(c)
Depth (km)
Distance (km)
Carbonate
C1
C2
C3
S1
S2
S3
S4
S5
S6
S7
S8
Mantle
GXT-2000
Layer 2
Layer 3
T1
T2
Serpentinized mantle
P–wave Velocity (km/s)

Figure 14

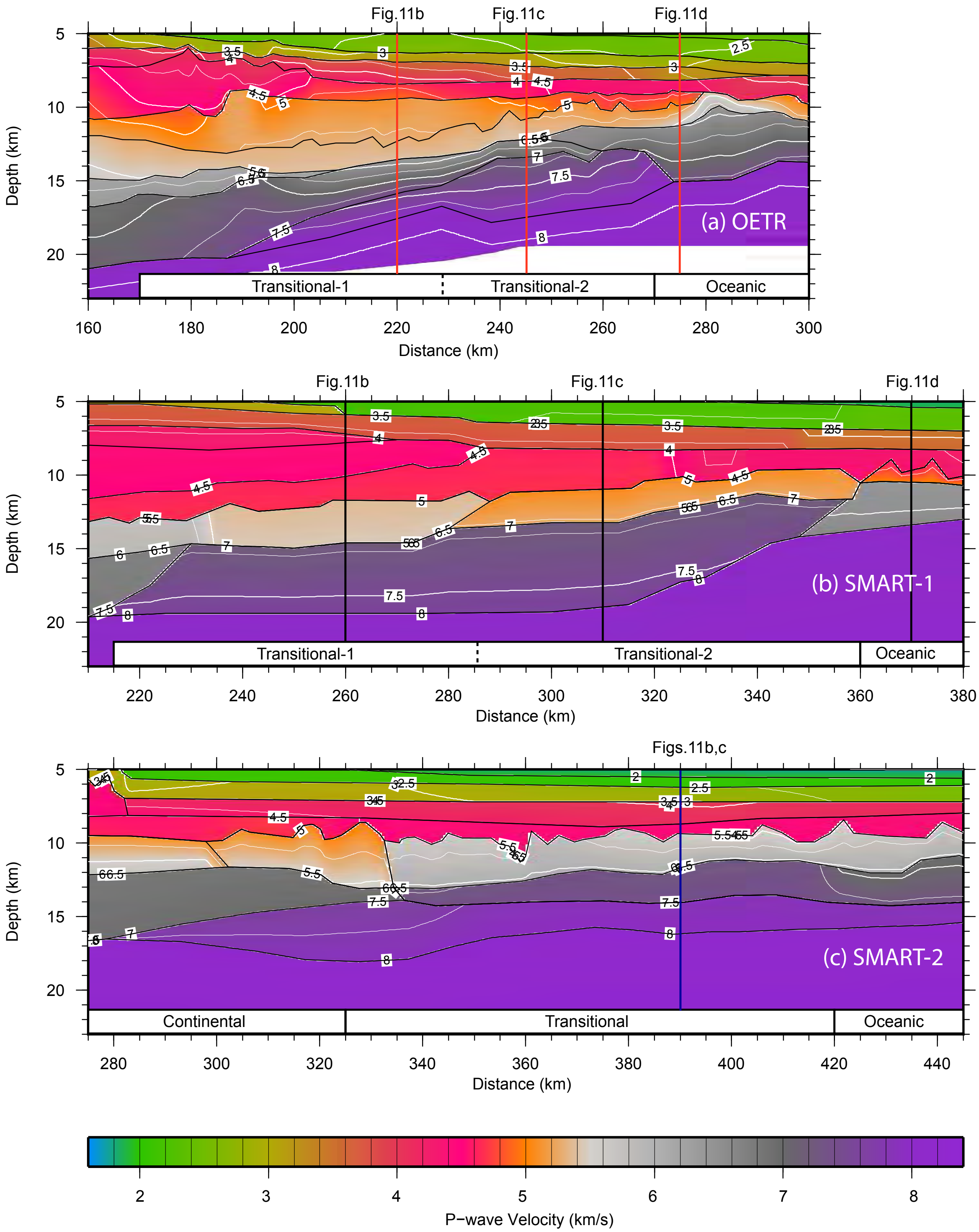

Fig.11b
Fig.11c
Fig.11d
Depth (km)
(a) OETR
Transitional-1
Transitional-2
Oceanic
Distance (km)
(b) SMART-1
Transitional-1
Transitional-2
Oceanic
Distance (km)
Figs.11b,c
(c) SMART-2
Continental
Transitional
Oceanic
Distance (km)
P−wave Velocity (km/s)

Figure 15

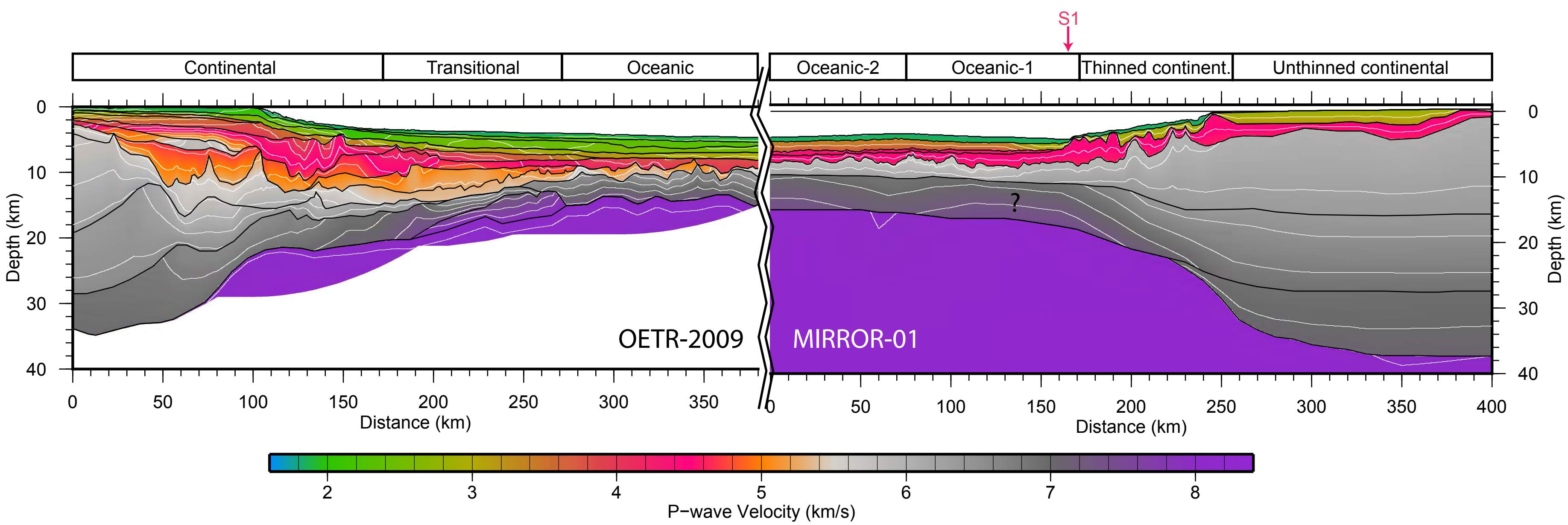

S1
Continental
Transitional
Oceanic
Oceanic-2
Oceanic-1
Thinned continent.
Unthinned continental
Depth (km)
Distance (km)
OETR-2009
MIRROR-01
?
P−wave Velocity (km/s)

Figure 16.

Table 1. Glossary of seismic phases

Phase	Description
Direct	Direct wave through the water
P_{sn}	P-wave refracted phase through the n^{th} sedimentary layer from the top
$P_{sn}P$	P-wave reflected phase from the bottom of the n^{th} sedimentary layer from the top
$P_{s6}P$	P-wave reflected phase coincident with base ? unconformity
P_{s7}	P-wave refracted phase through interpreted carbonate layer beneath the shelf
P_BP	P-wave reflected phase from the basement top
$P_{C1}/P_{C2}/P_{C3}$	P-wave refracted phase through the upper/middle/lower crystalline crust
$P_{C2}P/P_{C3}P$	P-wave reflected phase from the top of the middle/lower crystalline crust
P_mP	P-wave Moho reflection or reflection at the crust-mantle boundary
P_{n1}	P-wave refracted phase through interpreted, serpentinized mantle (T3)
P_{n2}	P-wave refracted phase through normal mantle

Table 2. Error analysis statistic for picked OBSs: number of raytraced picks (n), mean uncertainty of all input picks ($t_{uncertainty}$), RMS residual between modeled and observed traveltimes (t_{rms}) and normalized (χ^2)

	Phase	n	mean $t_{uncertainty}$ (s)	t_{rms} (s)	χ^2
Sediment	P_{S1}	658	±0.018	0.029	2.861
	$P_{S2}P$	3092	±0.021	0.018	0.791
	P_{S2}	2980	±0.017	0.025	2.304
	$P_{S3}P$	4407	±0.024	0.027	1.192
	P_{S3}	5553	±0.029	0.043	1.706
	$P_{S4}P$	9394	±0.032	0.034	1.157
	P_{S4}	822	±0.023	0.020	0.737
	$P_{S5}P$	338	±0.025	0.023	0.789
	P_{S5}	3185	±0.033	0.041	1.708
	$P_{S6}P$	6952	±0.033	0.030	0.799
	P_{S6}	4410	±0.037	0.060	2.714
	$P_{S7}P$	4514	±0.043	0.061	1.879
	P_{S7}	7271	±0.042	0.045	1.131
	$P_{S8}P$/ P_BP	7223	±0.046	0.062	1.566
	P_{S8}	2739	±0.048	0.051	1.166
	$P_{B'}P$	4567	±0.049	0.059	1.404
Crust	P_{C1}	3598	±0.049	0.052	1.080
	$P_{C2}P$	11387	±0.060	0.113	2.967
	P_{C2}	7135	±0.053	0.068	1.700
	$P_{C3}P$/ $P_{m'}P$	9278	±0.061	0.090	2.055
	P_{C3}	5186	±0.069	0.148	4.191
	P_mP	13805	±0.083	0.163	3.805
Mantle	P_{n1}	1726	±0.050	0.051	1.260
	P_{n2}	14937	±0.087	0.174	3.394
All		135157	±0.053	0.099	2.177

Note: The basement reflection is comprised of P_BP (reflection from the bottom of S7 where S8 is absent) and $P_{B'}P$ (reflection from the bottom of S8). P_mP (reflection from the bottom of C3) is the continental Moho whereas $P_{m'}P$ (reflection from bottom of O2) is the oceanic Moho.